Dipl.-Ing. Matthias Leitner, BSc.

Density of Liquid High-Melting Metals and the Estimation of Critical Point Data

DOCTORAL THESIS

to achieve the university degree of

Doktor der technischen Wissenschaften

submitted to

Graz University of Technology

Supervisor

Ao.Univ.-Prof. Dipl.-Ing. Dr.techn. Gernot Pottlacher

Institute of Experimental Physics
Thermophysics and Metalphysics Group

Graz, November 2019

This document is set in Palatino, compiled with pdfLaTeX2e and `Biber`.

The LaTeX template from Karl Voit is based on KOMA script and can be found online: https://github.com/novoid/LaTeX-KOMA-template

Affidavit

I declare that I have authored this thesis independently, that I have not used other than the declared sources/resources, and that I have explicitly indicated all material which has been quoted either literally or by content from the sources used. The text document uploaded to TUGRAZonline is identical to the present doctoral thesis.

Date	Signature

Acknowledgment

Writing a doctoral thesis would not be possible without the help of many supportive people. This is the time to say “Thank you”!

I would like to express my gratitude to my doctorate supervisor *Ao.Univ.-Prof. Dipl.-Ing. Dr.techn. Gernot Pottlacher*. Apart from his professional expertise and guidance, I deeply appreciated his amicable support, his MacGyver-like approach to troubleshooting and experimenting, his entertaining stories and of course the fabulous smoked trout.

Many PhD and master students, recently or previously in the group of Thermophysics and Metalphysics, shall be thanked for their input and for making the work environment very enjoyable and constructive. Some members of the group deserve to be mentioned separately in that context: *Dipl.-Ing. Dr. Alexander Schmon*, who introduced me to the art of pulse-heating and my fellow PhD colleagues *Dipl.-Ing. Thomas Leitner* and *Dipl.-Ing. Peter Pichler*.
Besides many discussions with strong home-brewed coffee of sometimes most challenging flavors, I would like to thank *Thomas* for his good-humored and helpful nature.
Peter, being a friend for almost two and a half decades, made the sometimes strenuous existence as an experimental physicist most entertaining. Frequent physical/philosophical discussions will make the time memorable in so many ways. Rock on!

Nothing works without family and good friends. Especially, I would like to thank my parents *Anita* and *Othmar* for their love and one-of-a-kind support over the years but also my sisters *Martina* and *Magdalena*. Spending time with these brilliant people brings the sometimes necessary change of scene.

Above all, I owe my most heartfelt gratitude to my wife *Astrid*, who helped and motivated me in so many ways over the years. Spending time together in the mountains and in remote places of foreign countries helped me to clear my mind and focus on the important things.

Finally, I would like to thank our child that, with an estimated mass of (1.18 ± 0.05) kg, as I write these lines, gave me the best writing motivation of all times ...

... dedicated to my grandfather Nikolaus Egger

Abstract

The liquid-phase density of selected high-melting transition metals up to the highest accessible temperatures is determined in this work. The metal samples were resistively heated from room-temperature up to the boiling point by means of ohmic pulse-heating, while monitoring their temperature and thermal expansion. Small modifications to the measurement setup were made to enhance the data quality and collect data at higher temperatures while reducing arising uncertainties. Normal spectral emissivity data were used to correctly assess the sample temperature via pyrometry. An uncertainty estimation according to the *guide to the expression of uncertainty in measurement* (GUM) was conducted.

Additionally, the critical point of these metals (i.e., critical temperature and critical density) as well as their phase diagram in the temperature-density-plane were estimated by extrapolating the obtained density data according to a simplified theoretical model, recently proposed by Schröer and Pottlacher.
This extrapolative approach is limited by the specimen's boiling point, which poses a natural upper temperature limit for the input data. Therefore, efforts were taken to increase the boiling point by performing high-pressure pulse-heating experiments. As a consequence, density data over a broader temperature range, i.e., closer to the critical point can be obtained. In the course of high-pressure pulse-heating experiments, a higher thermal expansion compared to that obtained in low-pressure experiments was observed for selected metals. The reason for this discrepancy is systematically searched for in this thesis.

Liquid-phase density and critical point data of the metals niobium, tantalum, tungsten, iridium and rhenium are presented and compared to data reported in the literature. In addition, various thermophysical properties were derived for the low-melting metal aluminum.

Zusammenfassung

Die vorliegende Arbeit beschäftigt sich mit der Bestimmung der flüssigen Dichte von ausgewählten hochschmelzenden Übergangsmetallen. Die Metallproben wurden mithilfe einer ohm'schen Pulsheizmethode von Raumtemperatur bis zu deren Siedepunkt erhitzt, während die Probentemperatur und thermische Ausdehnung mitgemessen wurden. Kleinere Modifikationen am Messaufbau wurden vorgenommen um die Datenqualität zu verbessern, Unsicherheiten zu reduzieren und als Folge Daten bei höheren Temperaturen zu bestimmen. Außerdem wurde der normale spektrale Emissionsgrad berücksichtigt um eine korrekte Temperaturzuweisung zu ermöglichen. Die Unsicherheiten der erhaltenen Daten wurden gemäß des GUM-Leitfadens abgeschätzt.

Zusätzlich wurden die kritische Temperatur und die kritische Dichte sowie das Phasendiagramm der jeweiligen Metalle aus den experimentellen Dichtedaten abgeschätzt. Die Abschätzung basiert dabei auf einer unlängst von Schröer und Pottlacher vorgeschlagenen Extrapolation dieser Daten zu höheren Temperaturen. Der extrapolative Ansatz wird durch den Siedepunkt des untersuchten Metalls beschränkt, da das Einsetzen des Siedens eine natürliche Temperaturobergrenze der Daten bedingt. Um zu höheren Temperaturen zu gelangen wurden Hochdruck-Pulsheizexperimente durchgeführt; hierbei wird der Siedepunkt durch den höheren statischen Druck erhöht, wodurch Daten über einen größeren Temperaturbereich erhalten werden können. Für ausgewählte Metalle wurde während dieser Experimente eine höhere Expansion als in Niederdruckexperimenten beobachtet. Die Ursachen hierfür werden in dieser Arbeit systematisch gesucht.

Die Dichte der flüssigen Phase sowie der kritische Punkt der Metalle Niob, Tantal, Wolfram, Iridium und Rhenium werden präsentiert und mit Literaturdaten verglichen. Zusätzlich wurden mehrere thermophysikalische Daten von Aluminium bestimmt.

Contents

List of Figures

List of Tables

1. Introduction and Motivation

Thermophysical properties of liquid metals at high temperatures and pressures, such as the density, are of interest in many areas of engineering and science. For instance, a metal's liquid density is used to calculate mass balance in refining operations or serves as input quantity in simulations that model thermal natural convection phenomena in furnaces and ladles as well as casting and solidification processes [1–3]. In fact, various physical models show a relatively strong sensitivity on density input data compared to other thermophysical properties [4].
But apart from the application of density data for simulations to improve production processes or better understand physical models, thermal expansion data are also needed in calculating other thermophysical properties, such as electrical resistivity, thermal conductivity and diffusivity as well as viscosity and surface tension.

While the density of pure metals is mostly well known in the solid phase, the situation is different for the liquid phase. Especially for some high-melting metals, an inconsistency can be observed between data previously reported by our work group and data given in the literature, which are inconsistent in themselves (compare Fig. 1.1). In addition, these data often do not reach far into the liquid phase or exhibit rather large uncertainties, if reported at all. This observation is also a consequence of the high temperatures involved and the resulting technical and physical difficulties, e.g., sample containment due to its high reactivity. These considerations and observations motivate a complementary revisit on the liquid density of selected high-melting metals.
Two main methods capable of such measurements emerge in this context: *Levitation methods*, where a liquid metal droplet is either electromagnetically or electrostatically levitated, and highly dynamic *pulse-heating methods*, where typically wire-shaped specimens are heated up to their boiling point

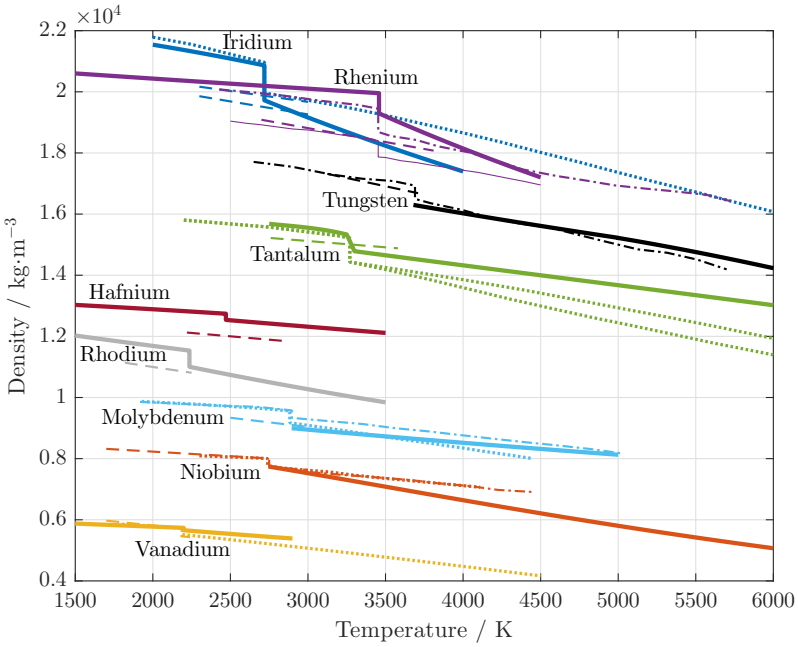

Figure 1.1.: Density as a function of temperature of relevant high-melting pure metals at the end of the solid and in the liquid phase. *Solid thick line*: Data by this work group [5] and references therein, *dashed line*: Liquid and undercooled density by Paradis and Ishikawa et al. (JAXA group) [2, 6–12], *dotted line*: Gathers and Shaner et al. (IEX group) [13–16], *dash-dotted line*: Hixson and Winkler [17–19], *solid thin line*: Thévenin et al. [20].

within microseconds. The first method delivers liquid-phase data in the vicinity of the melting point and in the undercooled liquid state. But when the aim is to obtain data far beyond the melting point, the pulse-heating method is the method of choice.

While a variety of thermophysical properties were previously acquired simultaneously in typical pulse-heating experiments at Graz University of Technology, A. Schmon suggested in his doctoral thesis to conduct exclusive density measurements to improve data quality [21].
The selection of metals to be revisited, using the Schmon approach, is based on three requirements: First, normal spectral emissivity data should be available for the chosen metals to ensure a correct temperature evaluation. Such

data were previously reported by our work group [22] for metals that can be investigated with a pyrometer at the standard wavelength of pyrometry, i.e., $\lambda = 650\,\mathrm{nm}$. The application of normal spectral emissivity data as a function of temperature is crucial for a correct temperature evaluation [23]. Second, the metals have to be ductile enough to be acquirable in the form of thin homogeneous sample wires that are typically used in pulse-heating experiments and third, the metals must not be radioactive.
Potential candidates fulfilling the above mentioned requirements are depicted in Fig. 1.1, where the density at the end of the solid and in the liquid phase reported by different authors are plotted. Based on this figure, the elements niobium, tantalum, tungsten, rhenium and iridium were chosen for a careful reinvestigation within the scope of this thesis.

Apart from the relevance of density data by itself, measuring a liquid metal's density as a function of temperature eventually also maps part of its phase diagram in the temperature-density plane. According to simplified models [24], the extrapolation of the density behavior to higher temperatures allows to estimate the metal's phase diagram and its critical point. This particular point in the phase diagram is not only of pure scientific interest, it is also very important in high temperature technologies, such as in aerospace and power engineering. In the latter, the data are needed for potential fission-reactor accident calculations and future fusion reactor designs [25]. Besides, the material's phase diagram and its critical point are of immediate interest in astrophysics and planetary physics, where modelers rely on data describing the response of metals under extreme conditions [26].

While an introductory chapter on various density measurement methods was already given in the doctoral thesis of A. Schmon [21], the next chapter will introduce the topic of the critical point and phase diagrams in more detail.

2. The Critical Point

Accessing the critical point of high-melting metals experimentally is very difficult due to the high pressure and temperature involved. Experimental data thus only exist for low-melting metals, while a variety of models is applied to estimate the critical point for experimentally inaccessible high-melting metals. In this chapter, fundamentals on the critical point, as well as previous and recent approaches of experimental, semi-empirical and theoretical nature are discussed.

2.1. Fundamentals

For understanding the term critical point, it is useful to explain the term equation of state (EOS) first. The equation of state links the state variables of a substance that depend on each other, such as pressure p, volume[1] V and temperature T to each other. In a general form, the equation of state f may be expressed as

$$f(p, V, T) = 0\,. \tag{2.1}$$

Thus, the EOS describes a surface in three-dimensional space spanned by the coordinates p, V and T. Such a surface, or three-dimensional phase diagram, is schematically depicted in Fig. 2.1. Each point on this surface corresponds to an equilibrium state of the system. For easier visualization, projections of this surface into one of the three planes spanned by the state variables are often considered, two of which are plotted in Fig. 2.1. In both the pV- and the pT-projection, the critical point is labeled, being the termination in the vapor pressure curve (pT-projection) and the meeting point between

[1] or density ρ.

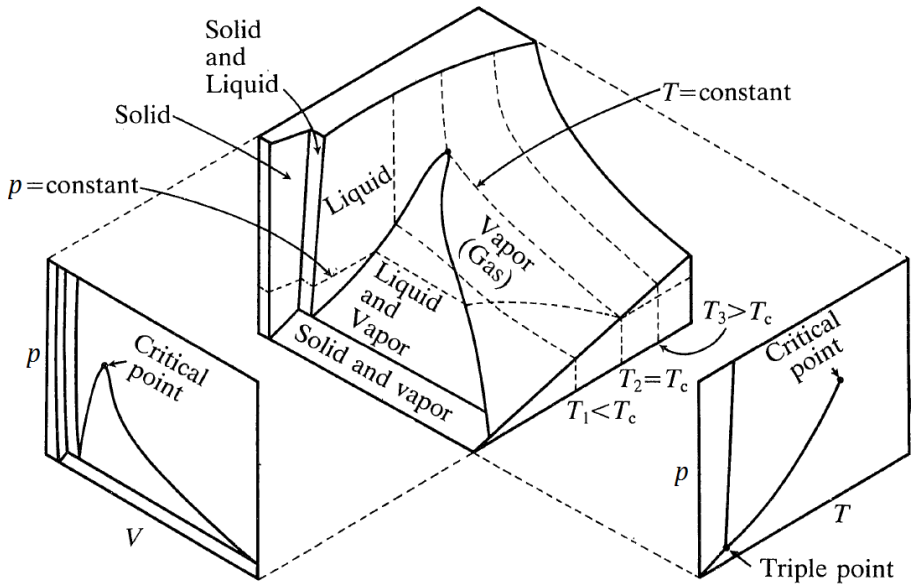

Figure 2.1.: Schematic three-dimensional phase diagram of a substance as a function of pressure p, volume V and temperature T, and projections into the pV- and pT-plane. The substance can be present in solid, liquid and vapor phase. Isobars (p = const.) and isotherms (T = const.) are indicated by dashed lines on the phase diagram surface. The critical point, being the termination of the vapor pressure curve is labeled in the projections. Graph taken from [1].

saturated liquid and saturated vapor line (pV-projection). In this point, all properties of the coexisting phases, i.e., liquid and vapor phase, are equal to each other. Note that at pressures below p_c, the volume V will increase discontinuously upon a phase change from the liquid to the vapor phase (jump in volume with increasing temperature, first order phase transition). However, at or above p_c, the jump in volume vanishes and the attributes liquid and gaseous become obsolete. Above the critical point the substance is said to be present as a supercritical fluid.

2.2. Direct experimental determination

Possibilities for direct experimental determination of the critical point (p_c, V_c, T_c) of low-melting metals[2] were previously reported by Pottlacher and Boboridis, e.g., [27, 28], using a pulse-heating technique. In these approaches, the static pressure acting on the sample was increased in successive experiments while searching for indications of reaching the critical point. The pressure dependence of the following quantities are such indications:

1. Persistent stability of the sample geometry,
2. Vanishing shock waves,
3. Changes of sample resistivity.

From the measured data, also the critical temperature T_c and the critical volume V_c may be estimated, as the sample temperature and its volume are also monitored throughout the experiment. A prerequisite for this direct approach is that the critical pressure of the investigated metal resides below the pressure achievable with the experimental apparatus, in this case $p \approx 5000\,\text{bar}$. Hence, this approach cannot be used to determine the critical point of high-melting metals, whose critical pressures are well above this achievable pressure.

Persistent stability of the sample geometry

Upon the phase change from the liquid to the vapor phase at the sample's boiling point, the sample's volume will increase discontinuously, compare Fig. 2.1. This jump in volume destroys the sample (phase explosion) and is clearly visible on images that are captured throughout the experiment. Increasing the static pressure p to a value above the sample's critical pressure p_c will thus lead to a vanishing of this phase explosion as there is no first order phase transition any more.

[2] Lead, zinc, indium and gold.

Vanishing shock waves

As a consequence of the vanishing phase explosion above p_c, no boiling shock wave will emerge from the sample surface if the static pressure is higher than the sample's critical pressure. This is a further indication that the chosen static pressure is equal to or greater than the critical pressure of the sample.

Changes in sample resistivity

With a static pressure above the sample's critical pressure, the slope of electrical resistivity as a function of enthalpy will increase only slightly, whereas for $p < p_c$, there will be a sharp increase due to the phase change from liquid to vapor.

Another direct experimental approach is the application of shock wave methods, as described by Fortov and Lomonosov [29].

2.3. Estimation of the critical point

Apart from few direct possibilities to obtain the critical point of metals, various semi-empirical and theoretical approaches exist. This section lays out possibilities reported in the literature to estimate the critical temperature, critical density and critical pressure. Finally, possibilities for obtaining the equation of state or a projection of it (phase diagram) are discussed.

2.3.1. Methods for estimating the critical temperature

Several empirical relations exist that relate the critical temperature to a more easily obtainable physical property, such as its boiling temperature or the heat of vaporization at normal pressure.

Relation to boiling point

GULDBERG RULE Stated by Guldberg in 1890, the critical temperature T_c may be related to the boiling temperature T_b at atmospheric pressure by an empirically determined factor A via

$$T_c = A \cdot T_b \,. \tag{2.2}$$

The proportionality factor A stated in the literature differs depending on the experimental data used to calibrate the relationship. Ohse and Tippelskirch cite a Guldberg factor of $A = 1.764$ [30]. Lang points out, that the factor appears to be group dependent [31]. For group I elements, he states a factor of $A = (2.49 \pm 0.22)$, but also indicates the strong variance in the data used to derive this factor. Based on theoretically predicted T_c values, Lang proposes $A = (3.69 \pm 0.20)$ for high-melting metals of the groups IV, VI and VIII. According to Hess and Schneidenbach, the factor originally stated by Guldberg was $A = 1.5$, while he states $A = (2.07 \pm 0.04)$, calibrating the relationship to the well known critical temperatures of potassium, rubidium and caesium [32].

GATES-THODOS RULE In 1960, Gates and Thodos [33] proposed a power-law relationship between the critical temperature T_c and the boiling temperature T_b at atmospheric pressure via the two coefficients A and B,

$$T_c = A \cdot T_b^B \,, \tag{2.3}$$

where $A = 1.4732\,\mathrm{K}^{1-B}$ and $B = 1.0313$. The empirical law was calibrated using experimentally determined critical temperature and boiling point data of 17 elements in a T_b-range between approximately 4 K to 800 K.

A similar law with different constants was proposed by Blairs taking into account experimental data of various metallic and non-metallic liquids [34]. Blairs states $A = 1.2574\,\mathrm{K}^{1-B}$ and $B = 1.0788$.

Relation to entropy of vaporization

GROSSE METHOD In 1961, Grosse made considerations to relate the entropy of vaporization[3] ΔS_v to the critical temperature T_c, as ΔS_v approaches zero at the critical point, much like the enthalpy of vaporization or the surface tension do [35]. Grosse applied the principle of corresponding states, implying that the molar entropy of vaporization ΔS_v should be equal for different liquids at the same reduced temperature T/T_c. Knowing the enthalpy of vaporization thus allows to deduce a critical temperature. Critical temperatures of high-melting metals reported in [35] are based on the behavior of mercury only.

Relation to heat of vaporization

KOPP-LANG RULE This rule, originally proposed in 1967, relates the critical temperature T_c to the heat of vaporization ΔH_v at the normal boiling point via a proportionality constant A,

$$T_c = A \cdot \Delta H_v \,. \tag{2.4}$$

The factor originally stated by Kopp[4] was $A = 26.8\,\mathrm{K \cdot mol \cdot kJ^{-1}}$ and modified by Lang[5] to $A = 28.73\,\mathrm{K \cdot mol \cdot kJ^{-1}}$ [30, 31]. Several years later, Hess and Schneidenbach proposed $A = (28.0 \pm 0.5)\,\mathrm{K \cdot mol \cdot kJ^{-1}}$, obtained by calibration with experimental data on the alkali metals [32].

Relation to surface tension

Several models exist, that relate the critical temperature to the surface tension. Authors reporting such models are for instance Grosse in 1962 [36] and Bohdansky in 1968 [37].

[3] $\Delta S_v = \Delta H_v / T$, with enthalpy of vaporization ΔH_v, and temperature T.
[4] Original value: $A = 0.112\,\mathrm{K \cdot mol \cdot cal^{-1}}$, conv. with 1 cal = 4.1868 J.
[5] Original value: $A = 0.1203\,\mathrm{K \cdot mol \cdot cal^{-1}}$, conv. with 1 cal = 4.1868 J.

In 2006, Blairs and Abbasi related the hard sphere diameter a as well as the surface tension σ and the molar volume V, all at the liquidus temperature, to the critical temperature T_c via

$$a^{5/2} = A \cdot \left[V \left(\frac{\sigma}{T_c} \right)^{1/4} \right] - B \,, \tag{2.5}$$

with the coefficients $A = 8.9833 \times 10^{-19}\,\mathrm{m}^{-1/2} \cdot \mathrm{mol} \cdot (\mathrm{K} \cdot \mathrm{m} \cdot \mathrm{N}^{-1})^{1/4}$ and $B = 1.0459 \times 10^{-25}\,\mathrm{m}^{5/2}$. The empirical relation was calibrated using a variety of literature data to calculate the term $V(\sigma/T_c)^{1/4}$ and relate it to $a^{5/2}$, where a was derived from the empirical relation

$$a^3 = (1.484 \pm 0.025) \times 10^{-24} \cdot V \,. \tag{2.6}$$

Further relationships

GOLDSTEIN SCALING PROPOSAL Proposed by Goldstein et al. in 1989 [38] and used by Hess and Schneidenbach [39], there is a scaling relation between the critical temperature and the plasmon energy at the critical point. As a consequence, the critical temperature T_c may be related to the electron density at the critical point $n_{e,c}$ via the proportionality constant A:

$$T_c = A \cdot \sqrt{n_{e,c}} \,, \tag{2.7}$$

with $A = (4.42 \pm 0.25) \times 10^{-8}\,\mathrm{cm}^{3/2} \cdot \mathrm{K}$.

ISOCHORIC THERMAL PRESSURE COEFFICIENT METHOD In 1993, Blairs and Abbasi used this method for the estimation of critical temperatures. The approach links the critical temperature to the speed of sound, the density and the isobaric heat capacity [40].

2.3.2. Methods for estimating the critical density

RULE OF RECTILINEAR DIAMETER To estimate the critical density of a material, the rule of rectilinear diameter often is applied. This rule, stated in 1887 by Cailletet and Mathias [41], assumes that the average density[6] of a liquid ρ_l, and its saturated vapor ρ_v, decreases linearly as a function of temperature T,

$$\frac{1}{2} \cdot (\rho_l + \rho_v) = A - B \cdot T \,, \tag{2.8}$$

where A and B are constants. The critical density may thus be estimated by linear extrapolation of experimental low-temperature liquid-density data up to an otherwise obtained critical temperature.
However, there is evidence that the phase diagram diameter does not decrease linearly with temperature, especially in the vicinity of the critical point [24, 39].

2.3.3. Methods for estimating the critical pressure

COMPRESSIBILITY FACTOR Following the VAN DER WAALS equation of state, a critical compressibility factor Z_c may be defined as

$$Z_c = \frac{p_c}{R_s \cdot \rho_c \cdot T_c} \,, \tag{2.9}$$

where R_s is the specific gas constant and p_c, ρ_c and T_c are the critical values for pressure, density and temperature. Knowing the critical values for compressibility, temperature and density thus allows to calculate the critical pressure. The critical compressibility factor ranges between approximately 0.2 to 0.3 for alkali metals, but can be significantly higher for other elements, e.g., $Z_c = 0.45$ for indium [28].

[6] This average value is often referred to as the "phase diagram diameter".

VAPOR PRESSURE A three-term vapor pressure equation may be fitted to experimental data, described by

$$\ln(p_\mathrm{v}) = A + \frac{B}{T} + C \cdot \ln(T)\,, \tag{2.10}$$

where p_v is the vapor pressure, T is the temperature, A, B and C are coefficients. At least for heavier alkali metals such a three-term equation is reported to describe the vapor pressure up to the critical point [42]. Extrapolating this equation to an otherwise determined critical temperature then allows to estimate a critical pressure. However, Hess and Schneidenbach state that experimental data well above the atmospheric pressure are needed in order to obtain meaningful coefficients [39, 42].

Hess proposed another approach to estimate both p_c and T_c by making use of the Likalter relation [43],

$$p = A \cdot (T \cdot E_\mathrm{i})^2\,, \tag{2.11}$$

where p is the pressure, T the temperature and E_i the ionisation energy of the undisturbed atom. Based on the alkalis, Hess et al. proposed $A = (1.66 \pm 0.12) \times 10^{-6}\,\mathrm{bar} \cdot \mathrm{K}^{-2} \cdot \mathrm{eV}^{-2}$ [42]. Somewhere along the curve described by equation (2.11), the critical point must be found. Consequently, the $(T_\mathrm{c}, p_\mathrm{c})$-pair may be obtained by intersecting the Likalter relation (equation (2.11)) with an extrapolated vapor pressure curve (equation (2.10)) [28, 42].

2.3.4. Methods for predicting the equation of state

Some of the following approaches do not give a whole equation of state, but rather yield a projection into a plane spanned by two state variables, e.g., density and temperature. In that case, an estimation of a two-dimensional phase diagram is obtained.

Classical van der Waals EOS

The equation of state proposed by VAN DER WAALS in 1873 takes the form

$$p = \frac{RT}{v-b} - \frac{a}{v^2}\,, \tag{2.12}$$

with pressure p, temperature T and molar volume v. The parameter a is a measure for the attractive forces between the particles, and b takes into account the non-zero volume that one mole of particles occupies. R is the universal gas constant.

The critical parameters (critical volume, pressure and temperature) may be calculated from the parameters a and b via

$$v_c = 3b, \qquad p_c = \frac{a}{27b^2}, \qquad T_c = \frac{8a}{27bR}\,, \tag{2.13}$$

but yield unsatisfactory results for metals with a high-boiling point [27].

Hard sphere and soft sphere van der Waals EOS

Young and Alder proposed an improvement to the classical van der Waals EOS in 1971 using hard-sphere-theory [44]. Pottlacher pointed out that the model (HSVDW) yields unfeasible data for liquids under pressure [27].

In 1977, Young made modifications which led to the soft sphere model for liquid metals (SSVDW) [45]. This model is based on Monte Carlo simulations and has various adjustable parameters. These parameters were chosen in accordance with experimental data of enthalpy (thus heat capacity) and volume as a function of temperature. Due to a systematic error in temperature measurement of the chosen experimental data, the resulting estimates for the critical temperature given in [45] might be too low, while critical volumes might be rather high [46].

A very good review on these two theories may be found in [46].

Other recent EOS approaches

Approaches exist to construct semi-empirical multi-phase wide-range EOS, where the construction is based on data obtained at high temperatures and high pressures [29, 47]. Amongst others, the data used originate from measurements of the isothermal compressibility (diamond anvil cells), isentropic-compression, sound velocity, isobaric expansion and shock compressibility.

Other recent approaches include first-principle quantum-molecular-dynamics (QMD) calculations of thermodynamic properties of liquid metals, e.g., [48, 49], and the use of scaling relations to derive binodals and the critical point based on properties of metals under normal conditions [50].

Schröer-Pottlacher approach

In 2014, Schröer and Pottlacher proposed an approach to estimate the critical temperature and critical density as well as the phase diagram in the ρT-plane on the basis of experimental liquid-phase density data [24].

It is this approach that was used during this thesis to test it on experimentally obtained density of transition metals. The different steps outlined on the following pages are graphically shown in Fig. 2.2.

ESTIMATION OF THE CRITICAL TEMPERATURE

A model function shall be fitted to the experimentally determined liquid-phase density regression $\rho_+(T)$ to obtain an estimate for the critical temperature T_c. The model function takes the form

$$\rho_+(T) - \rho_{\text{diam}}(T) = b \cdot (T_c - T)^{\beta}\,, \tag{2.14}$$

where T is the temperature, b is a constant and β is an exponent. The so-called phase diagram diameter $\rho_{\text{diam}}(T)$ in equation (2.14) is the average between the liquid density and the saturated vapor density[7], i.e.,

[7] In the following, subscript "$+$" indicates the liquid density while subscript "$-$" indicates the saturated vapor density.

$\rho_{\text{diam}}(T) = (\rho_+(T) + \rho_-(T))/2$. The vapor density $\rho_-(T)$ can be assumed to be zero in the experimentally accessible region. Therefore, $\rho_{\text{diam}}(T)$ may be approximated by $\rho_{\text{diam}}(T) = \rho_+(T)/2$ in the following considerations. The left hand side of equation (2.14) thus reduces to $\rho_+(T)/2$ yielding the model function

$$\rho_+(T) = 2 \cdot b \cdot (T_c - T)^\beta \,. \tag{2.15}$$

This function is fitted twice to the liquid phase density $\rho_+(T)$, assuming either an Ising or a mean-field exponent β,

$$\beta = \begin{cases} 1/3 & \text{Ising behavior} \\ 1/2 & \text{mean-field behavior} \,. \end{cases}$$

For each of the chosen exponents β, two fitting coefficients are obtained according to equation (2.15), namely the phase diagram width b_β and the critical temperature $T_{c,\beta}$, presuming the respective model. In lack of any further knowledge, the average of the two obtained critical temperatures is considered as a reasonable estimate for the critical temperature, i.e.,

$$T_c = \frac{(T_{c,1/3} + T_{c,1/2})}{2} \,. \tag{2.16}$$

Although this heuristic approach appears somewhat arbitrary, the authors could show that this approach yields good consistence with experimentally obtained critical temperatures of the alkali metals and thus seems to be justifiable.

CONSTRUCTING SIMPLIFIED ISING AND MEAN-FIELD PHASE DIAGRAMS

In a next step, the rule of rectilinear diameter is applied, where again $\rho_{\text{diam}}(T) = \rho_+(T)/2$ is assumed,

$$\rho_{\text{diam}}(T) = a_{\text{lin}} \cdot (T_{\text{max}} - T) \,, \tag{2.17}$$

yielding the fitting coefficients a_{lin} and T_{max}. Assuming the validity of this rule, a simplified Ising ($\beta = 1/3$) and mean-field ($\beta = 1/2$) phase diagram may thus already be given by combining equations (2.17) and (2.14),

$$\rho_{\pm,\beta}(T) = a_{\text{lin}} \cdot (T_{\text{max}} - T) \pm b_\beta \cdot (T_{\text{c},\beta} - T)^\beta \,, \tag{2.18}$$

where "+" again indicates the saturated liquid line and "−" indicates the saturated vapor line of the phase diagram.

ESTIMATION OF THE CRITICAL DENSITY

With the critical temperature being fixed (equation (2.16)), the critical density is now estimated in two ways, traditionally assuming a linear diameter (rule of rectilinear diameter), or as recently proposed a non-linear temperature variation (theory of complete scaling).

A model equation is fitted to the diameter data and extrapolated up to T_c according to

$$\rho_{\text{diam}}(T) = \rho_{\text{c},\gamma} + a_\gamma \cdot (T_\text{c} - T)^\gamma \,, \tag{2.19}$$

where

$$\gamma = \begin{cases} 1 & \text{rule of rectilinear diameter} \\ 2/3 & \text{theory of complete scaling: non-linear diameter} \,. \end{cases}$$

Depending on the exponent used, two estimates for the critical density $\rho_{\text{c},\gamma}$ are obtained among the fitting coefficients. Again, the average between these two obtained critical densities is taken as a reasonable estimate for ρ_c,

$$\rho_c = \frac{(\rho_{\text{c},1} + \rho_{\text{c},2/3})}{2} \,. \tag{2.20}$$

CONSTRUCTING A PHASE DIAGRAM BASED ON THE ESTIMATES FOR CRITICAL DENSITY AND CRITICAL TEMPERATURE

With the obtained estimates for T_c and ρ_c, the diameter data ρ_{diam} are fitted up to T_c according to a simplified phase diagram diameter model,

$$\rho_{\text{diam}}(T) = \rho_\text{c} \left(1 + a \cdot (T_\text{c} - T) + c \cdot (T_\text{c} - T)^{2/3}\right) \,, \tag{2.21}$$

yielding the phase diagram diameter coefficients a and c. In this simplified approach, the final phase diagram may then be expressed with

$$\rho_{\pm}(T) = \rho_{\text{diam}}(T) \pm b \cdot (T_c - T)^{1/3} \left(1 + b_2 \cdot (T_c - T)^{2/3}\right) , \tag{2.22}$$

where "+" and "−" again indicate the liquid and vapor saturation line, respectively. The phase diagram coefficients b and b_2 are obtained by fitting the liquid saturation line equation ("+" in (2.22)) to the experimental density regression, making use of the just derived mathematical expression for $\rho_{\text{diam}}(T)$.

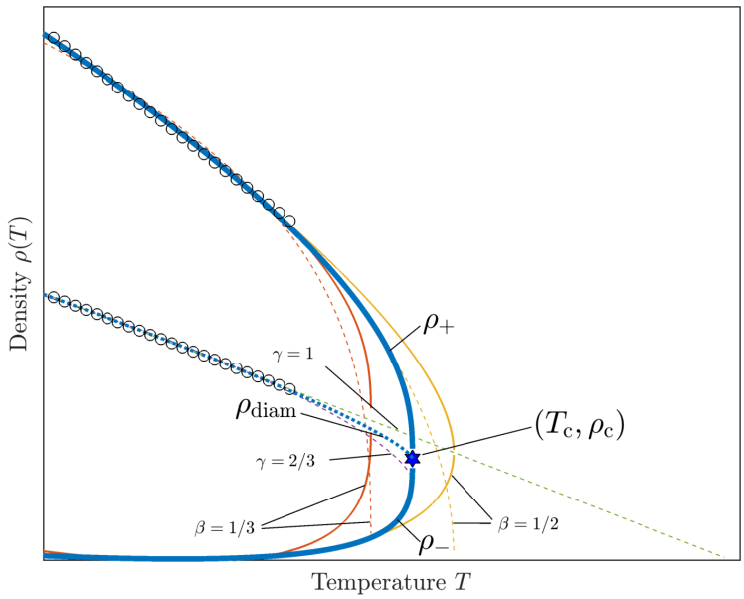

Figure 2.2.: Density data from experiments (○) and extrapolations (dashed lines) according to the Schröer-Pottlacher approach to obtain critical temperature T_c and critical density ρ_c and an estimate for the phase diagram $\rho_{\pm}$ (solid lines). For detailed information on the various lines the reader is referred to the text.

3. Experimental Method and Data Evaluation

This chapter gives detailed information about the method of ohmic pulse-heating, a method that resistively heats metallic sample wires from room-temperature up to the gas phase in order to derive thermophysical properties over a wide temperature range. Furthermore, a concise description of the formulas used in the derivation of these properties from the measured base quantities is given in this chapter.

3.1. Ohmic pulse-heating

With the dynamic method of ohmic pulse-heating, a thin metallic wire specimen with typically 0.5 mm in diameter and a length between 40 mm to 60 mm is resistively heated from room-temperature over the liquid phase up to the boiling point by passing a strong current pulse through it. The energy that is needed for this process is provided by a capacitor bank with a capacitance of 540 µF. This capacitor bank can be charged to voltages between 3 kV to 10 kV by a high voltage power supply (PTAG *2040* L). Once the stored energy is discharged through the wire specimen, currents of up to 10 kA will run through it. In order to start and stop the pulse-heating experiment by switching these high currents, a combination of Krytrons and Ignitrons (BK*508*, EEV) is used. Depending on the sample material, specifically its resistance and heat capacity as well as the chosen experimental parameters, it takes between 35 µs to 80 µs to heat a wire from room-temperature up to the boiling point, where it explodes due to the discontinuous increase in volume. It is desirable to stop the current flow over the wire at the time of explosion to suppress plasma discharges. The remaining capacitor energy is

then dissipated in crowbar resistors.
To influence the rise time of the current in a pulse-heating experiment, a series resistor in the circuit can be chosen between either $1/2\,\Omega$ or $1/4\,\Omega$. Changing to a lower resistance helps in heating samples with high electrical conductivity such as, e.g., aluminum.
For the circuit diagram of the pulse-heating setup used at Graz University of Technology, the reader is referred to the Appendix, Fig. A.1.

Typical heating rates that are achieved with the ohmic pulse-heating setup in Graz are on the order of $10^8\,\mathrm{K}\cdot\mathrm{s}^{-1}$. This fast heating implies several advantages that are inherent to fast pulse-heating techniques:

1. First, the experiment is long over before the vertically standing liquid metal wire can collapse due to gravity. Thus, measurements can be performed on a liquid metal sample.
2. Second, there is no time for chemical reactions of the sample material with its surrounding atmosphere[1] - the experiment is *quasi-containerless*.
3. And third, high heating rates suppress any axial expansion of the sample wire [21, 51, 52]. Therefore, it is sufficient to monitor the radial expansion of the wire during heating in order to deduce volume expansion data.

Even though the heating rates are very high, the sample remains in thermodynamic equilibrium. Hence, the experiment can be considered as *quasi-static* [53].

3.1.1. Measured quantities

During the whole experiment, several raw signals are measured as a function of time. These raw signals correspond to the voltage drop $\boxed{U(t)}$ along the wire[2], the current $\boxed{I(t)}$ through the wire, the normal surface radiance $\boxed{J(t)}$ of the wire and its thermal radial expansion $\boxed{d(t)}$. They are used in a

[1] N_2 or Ar in low-pressure experiments, distilled H_2O in high-pressure experiments.
[2] The voltage drop can only be measured with the low-pressure setup, while the high-pressure sample chamber was not designed for it, compare Sec. 3.1.2.

subsequent data evaluation to derive various thermophysical properties, see Fig. 3.6 and Sec. 3.2.
The first three quantities mentioned above are sampled at 10 MHz and are stored on a 14 bit transient recorder card (M2*i.4032*, *Spectrum*), which resides in a Faraday room. These signals are transferred to the Faraday room via BNC cables, that are fed through copper tubes. By this means, all measurement lines are shielded from the highly inductive currents that result from the discharge[3]. A *LabVIEW* script is used to record the raw signals (master thesis T. Macher [54]).
To monitor the thermal radial expansion of the wire, a highly intense background illumination is provided during the experiment by a commercial photoflash, compare Sec. 3.3.1. Shadow images of the expanding wire are acquired every 2.5 µs, corresponding to a sampling rate of 0.4 MHz. The image information is stored on a separate PC with the software *WinSIS* (*Theta System*).

Fig. 3.1 shows a typical set of measured signals during a pulse heating experiment. Dotted lines indicate data points before the pulse heating start and the regions of insensitivity and saturation in the case of the pyrometer signal $J(t)$. Note the pronounced horizontal plateau in the $J(t)$ trace that occurs during the melting process.

Voltage drop $\boxed{U(t)}$

The voltage drop $U(t)$ along the wire is measured using two molybdenum knife edges with a thickness of 0.1 mm that are attached to the wire in a distance of approximately 40 mm to each other, see Fig. 3.3 (b). For better wire contact, a small triangular-shaped piece is cut out of each knife's contact end. During the experiment, the voltage drop, divided via high impedance voltage dividers, is recorded from each of these knife edges towards common ground. The difference signal is later used for further evaluation to cancel out the contact resistance between voltage knife and wire.

[3] $\frac{\mathrm{d}I}{\mathrm{d}t}|_{t=0} \approx 700\,\mathrm{A}\cdot\mu\mathrm{s}^{-1}$.

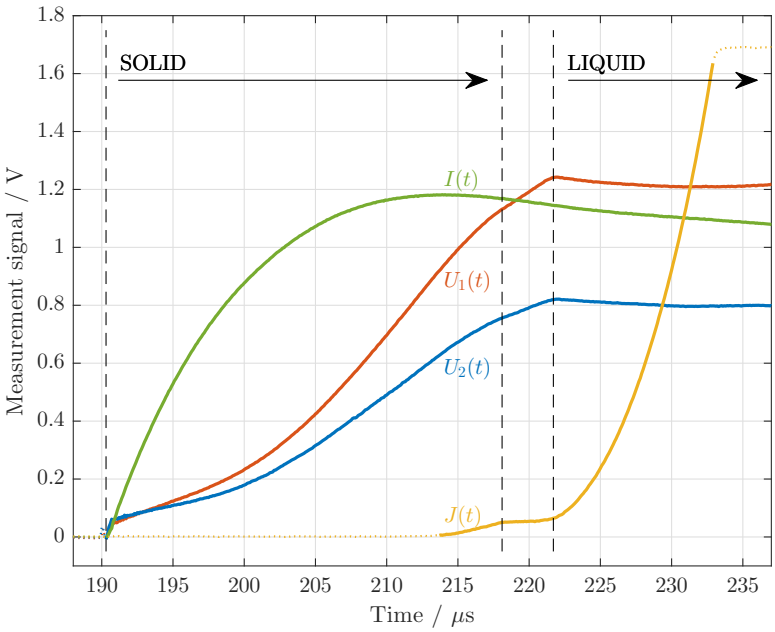

Figure 3.1.: A set of typical measurement signals obtained during pulse-heating as a function of time: Current $I(t)$, the two voltage signals $U_1(t)$, $U_2(t)$ and the surface radiance signal $J(t)$. The dotted lines of $J(t)$ show regions of pyrometer insensitivity and saturation.

Current $\boxed{I(t)}$

The current $I(t)$ is measured with an inductive current probe with real-time integration element (*Model no.: 3025, Pearson electronics*) which is in serial connection to the wire.

Surface radiance $\boxed{J(t)}$

The surface radiance $J(t)$ is monitored with a pyrometer throughout the experiment and is used to evaluate the sample's temperature afterwards. Depending on the material's melting point, four pyrometers with central

Table 3.1.: Specifications of pyrometers used during this thesis.
λ_c ... Central wavelength of interference filter
FWHM ... Full-width-at-half-maximum of interference filter

#	Diode	λ_c / nm	FWHM / nm	Temperature range
1	Si	649.7	37.2	$T \gtrsim 2000\,\mathrm{K}$
2	InGaAs	2350	458	$600\,\mathrm{K} \lesssim T \lesssim 1700\,\mathrm{K}$

wavelengths between 0.65 µm and 2.3 µm are available. For detailed information on the pyrometers used during this theses, consult Tab. 3.1.

Fig. 3.2 shows a schematic drawing of a pyrometer that was built at Graz University of Technology. It consists of a 1:1 imaging system that allows a precise adjustment of the wire specimen with the aid of a tiltable mirror (2) and a justage microscope with built-in scale (3). The position of the pyrometer is adjusted such that the wire center rests at 1.0 mm on the scale. In the measurement mode, the mirror is tilted upwards and frees the light path.

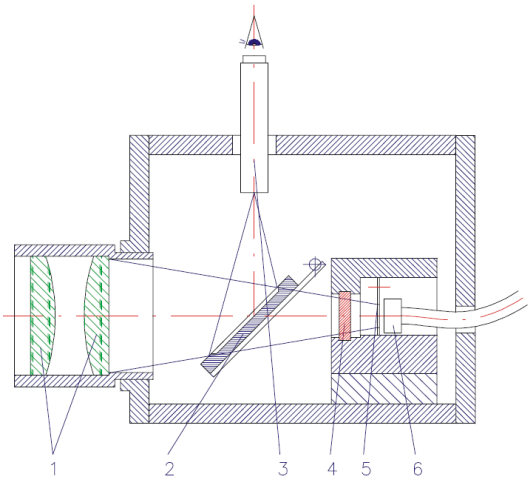

Figure 3.2.: Schematic drawing of a pyrometer. *1* achromatic lenses, *2* tiltable mirror, *3* justage microscope with scale, *4* interference filter, *5* rectangular-shaped field stop, *6* optical fiber towards photo diode. Image taken from [55].

In this mode, the light emitted from the wire passes an interference filter (*4*) which transmits light exclusively in a narrow wavelength interval and thus defines the measurement wavelength of the pyrometer. Subsequently, the light passes a field stop (*5*) and is led to a shielded photo diode and electronics via fiber optics (*6*).

Thermal radial expansion $\boxed{d(t)}$

In order to obtain a sufficiently fast image acquisition rate, a specialized CCD camera system is used (PCO *imaging*, controller unit by *Theta System* and *Graz Univ. of Technology*) in combination with a high-power photoflash for shadow imaging (*Multiblitz X10AC/DC*, 1000 W · s).
The high frame rate is achieved in two steps. First, the incoming photons are converted into electrons with the help of a photocathode. The generated electrons are then multiplied with a micro-channel-plate (MCP) and subsequently reconverted into electrons with a phosphorscreen (P46). This process amplifies the incoming light by a factor of about 10^4 and allows to use camera exposure times of less than 0.5 µs on the CCD sensor of the camera (sensor size: 384 pixel × 572 pixel).
The second measure to obtain a high image acquisition rate is to use only a few pixel lines of the sensor for shadow image acquisition, while using the mechanically masked remainder of the chip as fast buffer storage for previously acquired images. This allows to greatly enhance the image acquisition rate as the time-consuming read-out of the sensor can be postponed to a time after the experiment. For a more in-depth description of the setup to measure thermal expansion, please refer to the doctoral thesis of A. Schmon [21].
During the bigger part of this work, the sensor was masked such that only 8 lines are open for exposure. Typically, an exposure time of 300 ns was used, leading to the above mentioned frame rate of 4×10^5 fps, i.e., one image every 2.5 µs.

While all the above described quantities were previously measured simultaneously during pulse-heating experiments, A. Schmon proposed in his doctoral thesis to conduct exclusive expansion measurements, i.e., measurements without voltage knives [21]. By this means, sideways forces acting on

the wire are eliminated which results in non-moving wires and thus greatly enhances the measurement quality. In addition, the wire length between the brass electrodes is reduced to about 40 mm for expansion measurements compared to roughly 60 mm in measurements with voltage knives. This measure further stabilizes the wire and makes an exact vertical alignment easier.

Geometric properties

When measuring electrical data, the distance between the two voltage knives l_0 is determined with a cathetometer before the experiment (Vernier scale, division 0.02 mm). This length is primarily used in the evaluation to calculate the mass of the investigated wire piece.

The room-temperature wire diameter is measured with a laser micrometer (LS-*7010*, *Keyence Corporation*, combined uncertainty: 2 µm) at three different axial positions, where the sample is rotated in steps of 120° at each axial position. The arithmetic mean of these nine diameter values is used as the actual room-temperature diameter in the evaluation.

3.1.2. Setups for different isobaric conditions

In the group of *Thermophysics and Metalphysics*, the pulse-heating setup can be changed to conduct either low-pressure or high-pressure experiments, compare Tab. 3.2. Each of these experiments are isobaric experiments, where the focus resides on different physical aspects. The low-pressure setup has the advantage of a relatively comfortable voltage drop measurement, which allows to deduce properties such as specific enthalpy and resistivity. This is not possible with the high-pressure setup. On the other hand, the high-pressure setup allows to greatly increase the sample's boiling point by increasing the ambient pressure and thus enlarge the accessible temperature range to a high extent. When studying phase diagrams or investigating critical parameters of metals [28] this setup is the better choice.

Table 3.2.: Characteristics of the two pulse-heating setups for different isobaric conditions. Measurable quantities are indicated with a checkmark.

	Low-pressure setup	**High-pressure setup**
Pressure	$\approx 2.3\,\text{bar}$	1 bar to 5000 bar
Ambient medium	N_2 or Ar	distilled H_2O
Enlarge liquid range	×	✓
Temperature $T(t)$	✓	✓
Expansion $d(t)$	✓	✓
Voltage $U(t)$	✓	×
Current $I(t)$	✓	✓

Low-pressure experiments are typically conducted in nitrogen (ALPHAGAZ 1 N_2, 99.999 % (5.0)) at a pressure of approximately 2.3 bar. In these low-pressure experiments, the pressure is no experimental variable. The reason for the slight overpressure is to effectively inhibit flash arcs during the experiment[4].
In high-pressure experiments, distilled water is used as ambient medium. Among many other advantages, water is safer than gas due to its much smaller compressibility. The pressure can be chosen between 1 bar to 5000 bar. However, the pressure should exceed the critical pressure of water, $p_{c,H_2O} = 220.64\,\text{bar}$ [56], to avoid the formation of a water steam tube around the heated wire. To withstand such high pressures, a sample chamber was designed by G. Pottlacher in his doctoral thesis [27].

Apart from the sample chamber, the discharge circuit and experimental principle remain the same for both setups. These two setups will be discussed in the following sections.

[4] N_2 is usually preferred over Ar, as the dielectric strength of N_2 is higher than that of Ar. Flash arcs, which would lead to an erroneous enthalpy measurement, are thus inhibited more effectively.

Low-pressure setup

Fig. 3.3 (a) shows the low-pressure pulse-heating setup. The capacitor bank (*1*) and Krytrons to start and stop the pulse-heating experiment (*2*) can be seen at the top of the image. In the image center, the discharge chamber with inserted sample holder is visible (*3*). This chamber is equipped with three float glass windows[5] for optical diagnostics, i.e., shadow image acquisition for expansion measurements and surface radiance monitoring for subsequent temperature deduction. A gas in- and outlet (*4*) is connected to the chamber to pressurize it during the experiment and purge it afterwards. The measurement devices visible in Fig. 3.3 are the inductive current probe (*5*), which is connected in series with the wire sample, the shielded voltage measurement lines (*6*), the pyrometer (*13*) with gray filter (*14*) in front of it, and the CCD camera (*12*).
To acquire shadow images of the expanding wire, the light of the photoflash (*7*) is collimated with a simple convex lens[6] (*8*) before passing a notch-filter (*9*). This filter[7] minimizes the intensity of the flashlight at the measurement wavelength of the pyrometer. The light then passes an adjustable iris (*10*) that cuts out possibly remaining non-parallel light rays[8]. At the opposite side of the sample chamber, an imaging lens[9] (*11*) creates a shadow image on the photocathode of the CCD camera. For fine adjustment, the imaging lens and the pyrometer can be moved in three axes with micrometer screws. Note that the pyrometer view is orthogonal to the flash direction to minimize any stray light potentially being reflected into the pyrometer.

The sample holder is shown in Fig. 3.3 (b). The brass electrodes (*17*) are firmly squeezed with the clamps to electrically contact the sample wire (*15*). Also shown in this figure are the thin contacts for voltage drop measurement (voltage knives (*16*)).

[5]Dimensions: $(48 \times 48 \times 5)$ mm.
[6]Focal length collimator lens: $f = 60$ mm.
[7]For pyrometer at 650 nm: *Chroma* ZET647NF, FWHM ≈ 34 nm.
[8]Diameter: $\varnothing = 18$ mm.
[9]Focal length imaging lens: $f = 80$ mm.

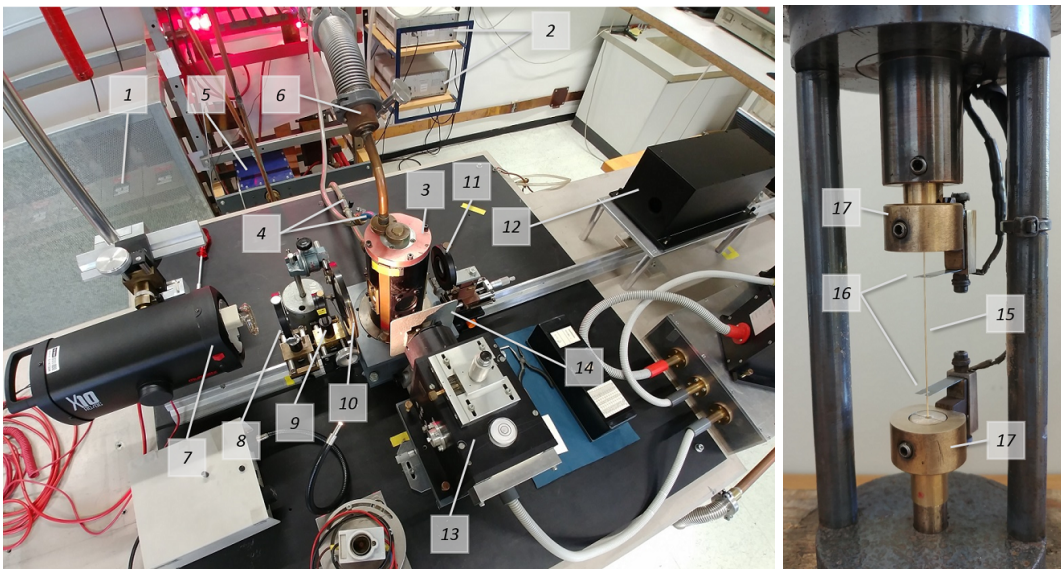

(a) (b)

Figure 3.3.: **(a) Low-pressure pulse-heating setup:** *1* capacitor bank, *2* Krytrons, *3* sample chamber, *4* gas in- and outlet, *5* Pearson probe, *6* voltage measurement lines, *7* photoflash, *8* collimator lens, *9* notch filter, *10* iris, *11* imaging lens, *12* CCD camera, *13* pyrometer, *14* gray filter holder.
(b) Sample holder: *15* wire specimen, *16* voltage knives, *17* brass electrodes and brass clamps.

High-pressure setup

The high-pressure setup is shown in Fig. 3.4 (a). The photoflash (*1*) is used in the exact same manner as with the low-pressure setup - it provides background illumination for the expansion measurement. The light is collimated with a convex lens[10] (*2*) and led through a notch filter (not visible in this image). It then enters the sample chamber that is made of solid stainless steel VEW N 701 (*3*) and can hold 0.25 l of water with the sample holder inserted. The inner diameter of this solid steel chamber is 60 mm, its walls have a thickness of 90 mm. Via two cylindrical sapphire windows[11], the flashlight enters and exits the sample chamber. These sapphire windows

[10] Focal length collimator lens: $f = 60\,\text{mm}$.
[11] Radius $r = 15\,\text{mm}$, thickness $d = 20\,\text{mm}$.

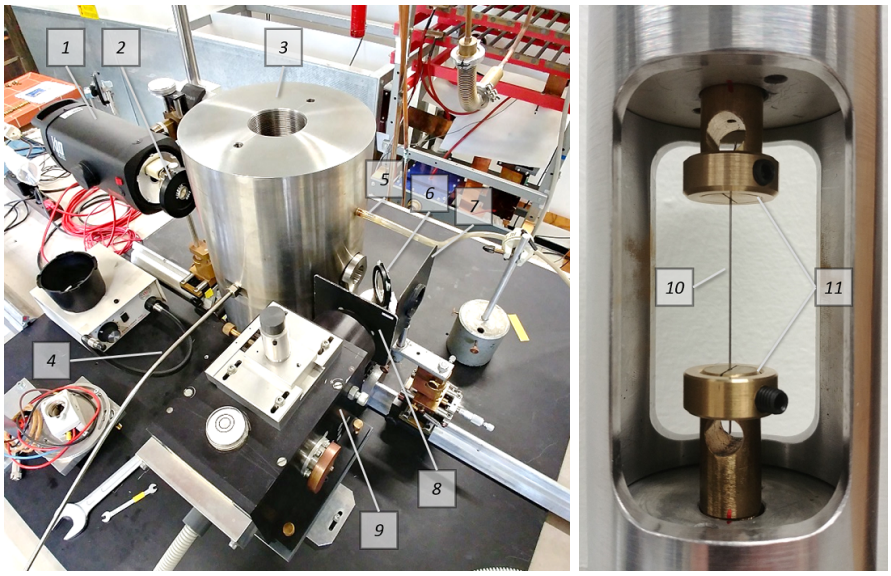

(a) (b)

Figure 3.4.: **(a) High-pressure pulse-heating setup:** *1* photoflash, *2* collimator lens + notch filter, *3* sample chamber, *4* water in- and outlet, *5* bore for pressure compensation, *6* beam splitter, *7* imaging lens, *8* pyrometer lens + gray filter holder, *9* pyrometer.
(b) Sample holder: *10* sample (wire), *11* brass electrodes and brass clamps.

have a clearance of 10 mm and are used because of their high mechanical strength and transmittance in the visible range.

To build up and release pressure, distilled water is pumped into or released from the sample chamber via a thin steel tube (*4*) with 6 mm outer and 1 mm inner diameter. A beamsplitter (*6*), that provides approximately 50 % of original intensity in each direction, splits the outcoming light into pyrometer and camera direction. This is necessary as the high-pressure vessel is equipped with only two windows.
The light traveling towards the CCD camera (not visible in this image) is imaged with a movable lens[12] (*7*). Another lens (*8*) is used in the high-pressure setup, to widen the incoming light and thus magnify the wire[13] before

[12]Focal length imaging lens: $f = 160\,\text{mm}$.
[13]Focal length concave lens: $f = -200\,\text{mm}$.

entering the pyrometer (*9*). By this means, a similar (high) magnification compared to the low-pressure setup is achieved, which ensures that the pyrometer's spotsize relative to the wire diameter is not larger than in experiments with the low-pressure setup.

Fig. 3.4 (b) depicts the sample holder used in high-pressure experiments. A sample wire (*10*) and brass electrodes (*11*), firmly squeezed by brass clamps to connect the wire to the electrical circuit, are visible. A typical distance between the electrodes is 40 mm, but it can be changed by using shorter or longer electrodes.

Not shown in Fig. 3.4 is the plug with an external thread that is connected to the sample holder and drilled into the sample chamber from above to seal it (special steel VEW V 155). Care has to be taken to avoid any metallic or granular residuals on the thread and to use enough petrolatum[14] on the external thread to avoid a rough-running process.
Also not visible is the equipment for the generation of pressure. Distilled water is pumped into the closed chamber with the aid of two pumps, a manually operated pump (*Enerpac 11-400* A1398C) and an electric screw press (*Dunze 625-700-3*) that is used in combination with a step motor (*Berger Lahr* RDM *51117/50*). The piping is equipped with one-way valves (*Nova Swiss 520.3433-1, 1.4571* NW*1.6*) and a needle-valve (*Dunze 61 89417*) to release the pressure after the experiment. A manometer (*Dunze 504-100-2, 61 89417*) monitors the pressure. The electronics for motor control, pressure setting and display were built by J. Friedrich[15].

3.1.3. Time sequence

The experiment's time sequence is controlled via a 5 V TTL pulse generator. The generated pulses trigger the data acquisition, the photoflash, the pulse heating and finally stop the pulse-heating at predefined times that can be changed in increments of 0.1 µs. A typical time sequence is shown in Fig. 3.5.

[14] Better known as Vaseline®.
[15] Institute of Experimental Physics, Electronics Workshop.

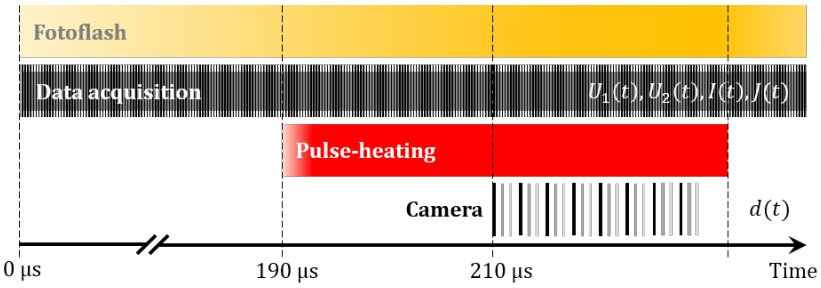

Figure 3.5.: Time sequence in a typical pulse-heating experiment. First, photoflash and data acquisition are activated. Pulse-heating is started shortly before the flash reaches its intensity maximum. When its intensity maximum is reached and the pyrometer becomes sensitive to the sample's surface radiation, the camera sequence is started.

First, the photoflash and the electrical data acquisition are started. The pulse-heating start is delayed by about 190 µs relative to the flash start to account for the intensity rise time of the flash. After another delay of approximately 20 µs, the camera sequence is started. Shadow images of the radially expanding wire are thus acquired during the time of maximum flash intensity and within the temperature range of pyrometer sensitivity. The vertical bars in Fig. 3.5 at a given color indicate the instants in time at which images are taken. The width of these bars symbolizes the exposure time of a single image. To obtain expansion values in between the sampled temperature values, the camera start in a successive experiment is shifted relative to the pulse-heating start, as symbolized by the changing color of the vertical bars (compare also Sec. 3.3.2).

3.2. Data evaluation

This section gives the mathematical and physical background for the data evaluation. Fig. 3.6 shows a flowchart of obtained base quantities (squares) in a typical pulse-heating experiment and thereof derived physical quantities (circles). These derived physical quantities, commonly referred to as *thermophysical properties*, can be grouped into directly obtained quantities (1^{st} and 2^{nd} step) and into quantities that indirectly follow via physical models

(3^{rd} step).
Part of the first group are the specific enthalpy $H(T)$, the heat capacity of the liquid metal c_p, the electrical resistivity $r_{\mathrm{VE}}(T)$, the volume expansion $V(T)/V_0$, and the density $\rho(T)$.
Applying physical models, these thermophysical quantities can be used to calculate the thermal conductivity $\lambda(T)$ and thermal diffusivity $a(T)$ and give estimates for the critical density ρ_{c} and the critical temperature T_{c}.

For the evaluation of temperature, specific enthalpy and uncorrected electrical resistivity, the MATLAB script *Hotwire*, written by F. Sachsenhofer [57] and updated by T. Macher [54] is used. This script also allows to correct the measured voltage drop for any inductive parts. In the following, $U(t)$ represents this corrected voltage drop along the wire.

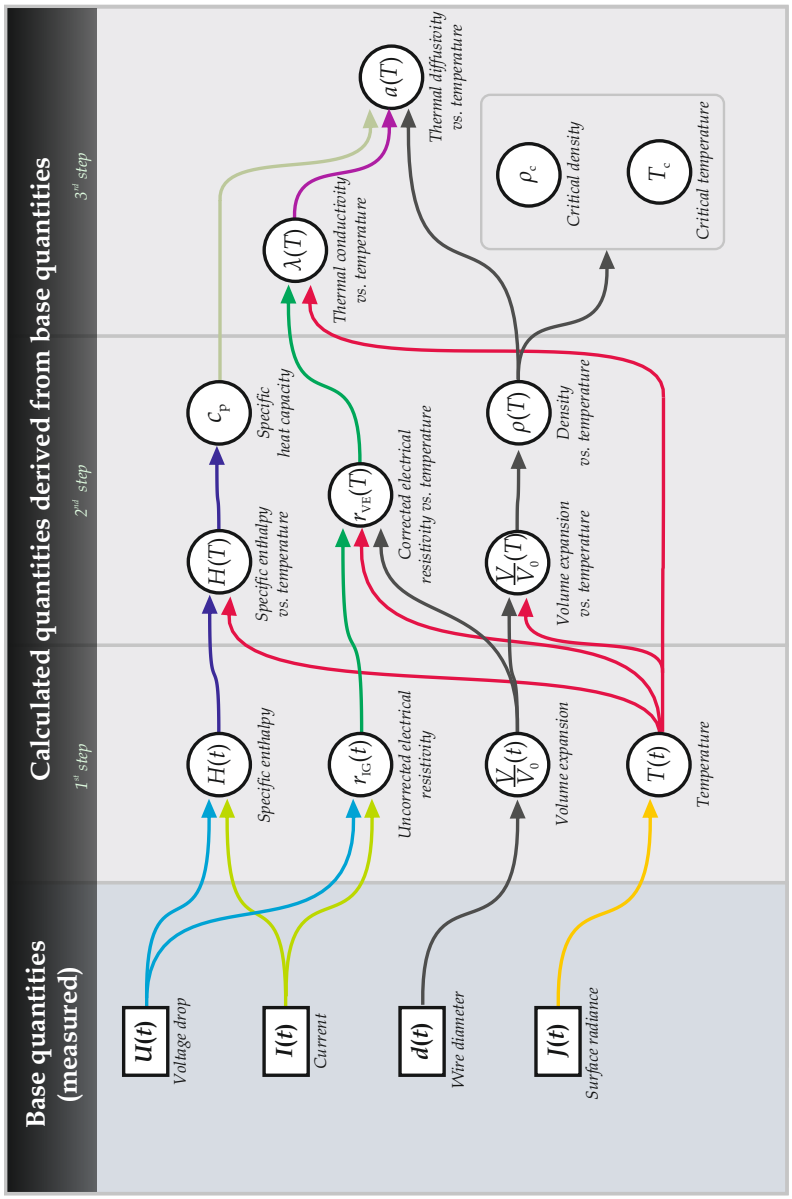

Figure 3.6.: Flowchart of measured and derived quantities in pulse-heating experiments.

3.2.1. Temperature

The temperature measurement via pyrometry is based on PLANCK's law of radiation, that describes the spectral radiance $L_{\lambda,\mathrm{B}}(\lambda, T)$ of a black body[16] at a given wavelength λ and temperature T via

$$L_{\lambda,\mathrm{B}}(\lambda, T) = \frac{c_1}{\pi \cdot \lambda^5} \cdot \left[\exp\left(\frac{c_2}{\lambda \cdot T}\right) - 1\right]^{-1} , \tag{3.1}$$

with the two constants[17] c_1 and c_2.

However, real radiators such as the specimen under investigation, emit radiation less efficiently than a black body, which is described by the emissivity $\varepsilon(\lambda, T)$. This quantity is the ratio of the spectral radiance of a real body $L_\lambda(\lambda, T)$ to the spectral radiance of a black body $L_{\lambda,\mathrm{B}}(\lambda, T)$ at the same temperature and wavelength,

$$\varepsilon(\lambda, T) = \frac{L_\lambda(\lambda, T)}{L_{\lambda,\mathrm{B}}(\lambda, T)} \leq 1 . \tag{3.2}$$

Gathering pyrometer related properties, such as geometrical factors, transmission of the optics, properties of the interference filter used and remaining constants in (3.1) to a calibration constant K, the pyrometer signal $J(T)$ can be expressed via

$$J(T) = K \cdot \varepsilon(\lambda, T) \cdot \left[\exp\left(\frac{c_2}{\lambda \cdot T}\right) - 1\right]^{-1} . \tag{3.3}$$

The pyrometers used during this work were not calibrated directly at a black body or a tungsten strip lamp, but calibrated indirectly. In this indirect calibration procedure, the phenomenon of latent heat is utilized - when the specimen undergoes the phase transition from solid to liquid, the energy that is put into the sample will not further elevate its temperature, but rather lead to a breaking of crystal bonds and thus a transition to the liquid phase.

[16] Subscript "B" for black body.

[17] $c_1 = 2 \cdot \pi \cdot c^2 \cdot h$, with c, the speed of light in the medium and h, the PLANCK constant. $c_2 = c \cdot h / k_\mathrm{B}$, with k_B, the BOLTZMANN constant.

Therefore, a plateau is visible in the radiance-over-time diagram during the several µs-long melting process, compare Fig. 3.1. Assigning the known melting temperature to this plateau value allows to deduce the temperature as a function of time (*indirect calibration*).

Depending on whether information on the normal spectral emissivity $\varepsilon(\lambda, T)$ at the measuring wavelength λ is available or not, two approaches are used.

No information on normal spectral emissivity available

If no information on the normal spectral emissivity ε at the pyrometer's measuring wavelength λ is available, assumptions have to be taken. Relating the pyrometer signal $J(T)$ at any temperature T, as given in equation (3.3), to its expression at the melting temperature $J(T_\mathrm{m})$, results in equation (3.4),

$$T(t) = \frac{c_2}{\lambda \cdot \ln\left\{ \frac{J(T_\mathrm{m})}{J(T)} \cdot \cancelto{\approx 1}{\frac{\varepsilon(\lambda,T)}{\varepsilon(\lambda,T_\mathrm{m})}} \cdot \left[\exp\left(\frac{c_2}{\lambda \cdot T_\mathrm{m}}\right) - 1\right] + 1 \right\}}, \qquad (3.4)$$

where c_2 is the second radiation constant. Note that the subscript "m" indicates values at the melting point. To be able to proceed, it is assumed that the emissivity remains constant with respect to its value at the beginning of the liquid phase $\varepsilon(\lambda, T_\mathrm{m})$, i.e., $\varepsilon(\lambda, T)/\varepsilon(\lambda, T_\mathrm{m}) \approx 1$. Pottlacher and Seifter showed that this assumption is feasible, as long as the measurements do not reach too far away from the melting point [23, 58].

When the goal is to obtain thermophysical properties up to the highest temperatures accessible, as it is in this work, this approach can not be used as it can lead to systematic temperature errors of up to 500 K at the highest temperatures.

Information on normal spectral emissivity available

If data on the normal spectral emissivity of the investigated material are available, the pyrometer signal can easily be converted to true temperatures.

In a first step, the calibration constant K is evaluated according to equation (3.5), by assigning the known radiance temperature at melting[18] $T_{\mathrm{r,m}}$ to the pyrometer signal at melting, $J(T_{\mathrm{r,m}})$, via

$$K = J(T_{\mathrm{r,m}}) \cdot \left[\exp\left(\frac{c_2}{\lambda \cdot T_{\mathrm{r,m}}} \right) - 1 \right] , \tag{3.5}$$

where c_2 is again the second radiation constant and λ is the mean effective wavelength of the pyrometer. Note that the radiance temperature at melting $T_{\mathrm{r,m}}$ is in this work directly derived via the literature value for the true melting temperature T_{m} and the normal spectral emissivity $\varepsilon(\lambda, T_{\mathrm{m}})$, reported previously by our group [22], via equation (3.6),

$$T_{\mathrm{r,m}} = \frac{c_2}{\lambda \cdot \ln\left\{ \frac{1}{\varepsilon(\lambda, T_{\mathrm{m}})} \cdot \left[\exp\left(\frac{c_2}{\lambda \cdot T_{\mathrm{m}}} \right) - 1 \right] + 1 \right\}} . \tag{3.6}$$

The radiance temperature as a function of time $T_{\mathrm{r}}(t)$ is then calculated from the pyrometer signal $J(T_{\mathrm{r}}(t))$ and the calibration constant K, with

$$T_{\mathrm{r}}(t) = \frac{c_2}{\lambda \cdot \ln\left(\frac{K}{J(T_{\mathrm{r}}(t))} + 1 \right)} . \tag{3.7}$$

Finally, the calculated radiance temperature as a function of time is converted to a true temperature $T(t)$ making use of the normal spectral emissivity $\varepsilon(\lambda, T_{\mathrm{r}})$,

$$T(t) = \frac{c_2}{\lambda \cdot \ln\left\{ \varepsilon(\lambda, T_{\mathrm{r}}) \cdot \left[\exp\left(\frac{c_2}{\lambda \cdot T_{\mathrm{r}}(t)} \right) - 1 \right] + 1 \right\}} . \tag{3.8}$$

[18] Note that the index "r" indicates *radiance* temperatures. They have to be used because the normal spectral emissivity is given as a function of radiance temperature.

3.2.2. Volume expansion and density

Fig. 3.7 (a) and (b) depict two images that consist of a sequence of shadow images where each image slice has a resolution of 8 pixel $\times$ 384 pixel (horizontal streaks) being 2.5 µs apart in time. While Fig. (a) is a "cold" sequence captured prior to the pulse heating start, Fig. (b) shows the actual radial expansion ("hot" sequence), and finally the phase explosion during pulse heating (bright region). To deduce a diameter of the wire at a specific instant in time, the gray scale values I_g of each image slice i are summed up in vertical direction, i.e.,

$$I_i(x) = \sum_{y=1}^{8} I_g(x,y), \quad x \in [1,384] \,, \tag{3.9}$$

yielding an intensity profile $I(x)$, as exemplified in Fig. 3.7 (c), for each image slice i. The full-width-at-half-maximum (FWHM), indicated in the figure, is then used as the wire diameter $d(t)$ at a specific instant in time t. This evaluation is done for each of the processable image slices in the hot and cold image sequence, by manually choosing an upper and a lower intensity level using the MATLAB script *Wiredia*. The FWHM is then calculated with sub-pixel resolution by using a linear interpolation between the discrete $I(x)$ values.

To derive the relative thermal radial expansion, the diameter of each image slice i captured during pulse-heating, d_i, is related to the corresponding image slice captured prior to pulse-heating, $d_{0,i}$. This is important, as d_0 oscillates with an amplitude of approximately ± 1 pixel and a period of $i = 9$ images due to electronic effects of the camera system[19]. As the expansion measurement is time-synchronized with the recording of the remaining base quantities, a temperature T can be assigned to each of the diameter values. The relative volume expansion as a function of temperature $V(T)/V_0$ can then be calculated with the previously derived diameter values via

[19]Using wires with a diameter of 0.5 mm results in a pixel diameter of approximately 100 pixel - therefore, the oscillation amplitude corresponds to approximately ± 1 % of the imaged diameter.

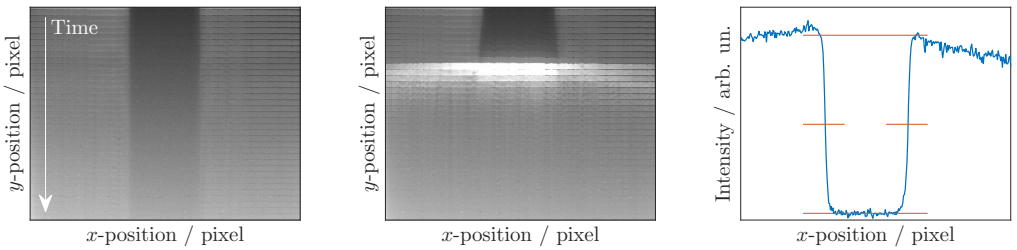

(a) (b) (c)

Figure 3.7.: (a) Image sequence captured prior to the pulse-heating start. (b) Image sequence taken during the pulse-heating experiment. Radial expansion of the wire and the phase explosion (bright horizontal band) can be observed. Time and temperature can be assigned to each of the image slices. (c) Exemplary intensity profile of one streak-image to deduce a precise diameter (FWHM) for density determination. Images taken from publication II of this work [59].

$$\left(\frac{V(T)}{V_0}\right) = \left(\frac{d(T)^2 \cancel{\pi}}{\cancel{4}} \cdot l(T)\right) \cdot \left(\frac{\cancel{4}}{d_0^2 \cancel{\pi}} \cdot \frac{1}{l_0}\right) . \tag{3.10}$$

Under the prerequisite, that no axial expansion occurs during the heating process, i.e., $l(T) = l_0$, equation (3.10) can be further simplified and the volume expansion can be expressed by the square of the radial expansion,

$$\left(\frac{V(T)}{V_0}\right) \overset{l(T)=l_0}{=} \left(\frac{d(T)}{d_0}\right)^2 . \tag{3.11}$$

To fulfill this prerequisite of non-axial expansion, the heating-rates have to be sufficiently high [21, 51, 52]. Heating rates chosen too low would cause a bending of the wire as the distance between the electrodes is fixed, and thus the wire would start to move radially. Thankfully, this problem can be diagnosed easily with shadow imaging.

T. Hüpf supposed in his doctoral thesis, that the inhibited axial expansion is eventually compensated by an increased radial expansion [52] which makes it possible to derive the density $\rho(T)$ from thermal radial expansion data and the room-temperature density ρ_0 via

$$\rho(T) = \rho_0 \cdot \left(\frac{d_0}{d(T)} \right)^2 . \tag{3.12}$$

The room-temperature densities ρ_0 used in this work were carefully selected from the literature.

This approach was used throughout the years at the pulse-heating laboratory in Graz, but also found application in other pulse-heating facilities, such as at the *Lawrence Livermore Laboratory* [14]. Furthermore, comparing density results obtained with equation (3.12) to results obtained with completely different static methods, such as the electrostatic levitation method (Ishikawa, Paradis et al., e.g., [60]), indicates that the pulse-heated wires are indeed showing an increased radial expansion that relates to the sample-specific volume expansion.

3.2.3. Specific enthalpy and heat capacity

The enthalpy H is the sum of a system's internal energy U and the product of pressure p and volume V,

$$H = U + pV , \tag{3.13}$$

and is a measure for the system's energy content. The total differential of H can be written as

$$\mathrm{d}H = \mathrm{d}U + p\,\mathrm{d}V + V\,\mathrm{d}p . \tag{3.14}$$

Considering that pulse-heating is an isobaric process ($p = \text{const.}$), it follows with the differential of the inner energy, $dU = \delta Q - p\,\mathrm{d}V$, that the change in enthalpy equals a change in heat,

$$\mathrm{d}H = \delta Q . \tag{3.15}$$

This specific enthalpy $H(t)$ originating from the transformation of electrical energy into the heat $Q(t)$ via the specimen's resistivity, can be obtained by

integrating the electrical power over time t and relating it to the mass m of the investigated wire piece,

$$H(t) = \frac{1}{m} \int_0^t U(t') I(t') \, \mathrm{d}t' \, . \tag{3.16}$$

The mass m is calculated from the room-temperature density ρ_0 that is usually adopted from the literature and its geometric dimensions, i.e., diameter d_0 and length between the voltage knives l_0:

$$m = \rho_0 \cdot \frac{d_0^2 \cdot \pi}{4} \cdot l_0 \, . \tag{3.17}$$

Note that the derived $H(t)$ describes the sample's enthalpy starting at room-temperature.
The specific heat capacity at constant pressure c_p, which is the amount of heat per unit mass that is needed to raise the sample's temperature by 1 K, can then be calculated via

$$c_\mathrm{p} = \left(\frac{\partial H}{\partial T} \right)_\mathrm{p} \, . \tag{3.18}$$

3.2.4. Electrical resistivity

The electrical resistivity at initial geometry r_IG, that is without considering any thermal expansion, can be derived according to

$$r_\mathrm{IG}(t) = \frac{U(t)}{I(t)} \cdot \frac{d_0^2 \cdot \pi}{4 \cdot l_0} \, , \tag{3.19}$$

where $U(t)$ and $I(t)$ are the voltage drop and the current though the sample at time t, d_0 and l_0 are the wire diameter and length between the voltage knives at room-temperature. Clearly, with this description the electrical resistivity is underestimated, because the wire expansion is neglected.

The physically correct expression, considering the sample's volume expansion (subscript "VE") is given via

$$r_{\mathrm{VE}}(t) = \frac{U(t)}{I(t)} \cdot \frac{d(t)^2 \cdot \pi}{4 \cdot l(t)} \,, \tag{3.20}$$

where now the actual diameter $d(t)$ and the actual length $l(t)$ are considered. Because of the fast heating rates, axial expansion of the sample is inhibited - thus, the distance between the voltage knives remains constant, i.e., $l(t) = l_0$ (compare Sec. 3.2.2). Therefore, the correct electrical resistivity can be obtained by multiplying the electrical resistivity at initial geometry, r_{IG}, with the measured radial expansion squared:

$$r_{\mathrm{VE}}(t) = r_{\mathrm{IG}}(t) \cdot \left(\frac{d(t)}{d_0} \right)^2 \,. \tag{3.21}$$

3.2.5. Thermal conductivity and diffusivity

The thermal conductivity $\lambda(T)$ is a thermophysical quantity describing how well a material conducts heat via thermal conduction in response to a temperature gradient.

Whenever the thermal conduction mechanism is dominated by electronic contribution, such as close to a pure metal's melting point and in its liquid phase, the thermal conductivity λ can be approximated by the empirical WIEDEMANN-FRANZ law. This law relates the thermal conductivity to the electrical conductivity $\sigma = 1/r_{\mathrm{VE}}$ (with r_{VE}, the electrical resistivity) and the temperature T via a proportionality factor L,

$$\lambda(T) = \frac{L \cdot T}{r_{\mathrm{VE}}(T)} \,. \tag{3.22}$$

During this work, the theoretical LORENZ-number $L = L_0 = \pi^2/3 \cdot (k_{\mathrm{B}}/e)^2$ [61, 62] was applied, where k_{B} is the BOLTZMANN constant[20] and e is the

[20] New SI-value: $k_{\mathrm{B}} = 1.380\,649 \times 10^{-23}\,\mathrm{J \cdot K^{-1}}$.

elementary charge[21]. According to the redefinition of SI base units that took effect in May 2019 (*new SI*) [63], a theoretical LORENZ-number of $L_0 = 2.443 \times 10^{-8}\,\mathrm{V^2 \cdot K^{-2}}$ ensues.

The thermal diffusivity $a(T)$ is a property that describes how the spatial distribution of temperature changes with time as a consequence of thermal conduction due to a temperature gradient present. It can be calculated via the thermal conductivity $\lambda(T)$, the density $\rho(T)$ and the specific heat capacity c_p,

$$a(T) = \frac{\lambda(T)}{c_\mathrm{p} \cdot \rho(T)} \,. \tag{3.23}$$

Applying the WIEDEMANN-FRANZ law to equation (3.23) and representing the electrical resistivity with (3.21), and the density $\rho(T)$ with (3.12), allows to estimate $a(T)$ even without measuring thermal expansion:

$$a(T) = \frac{L \cdot T}{c_\mathrm{p} \cdot r_\mathrm{IG} \cdot \rho_0} \,. \tag{3.24}$$

3.3. Improvements on thermal expansion measurement

During the measurements on aluminum it became obvious that the photo-flash used for shadow-imaging had to be replaced. Occurring problems included delayed flash starts but also total flash failures. These problems greatly reduced the number of processable expansion measurements. But also other issues limited the measurement quality in thermal expansion measurements such as the time sequence typically used, where the image acquisition is started before the pulse-heating experiment is started. Finally, the number of pixel lines open for exposure was reduced from 16 to 8 pixel lines, to double the frame rate and thus improve efficiency compared to previous experiments. These issues are discussed in more detail in the following subsections.

[21] New SI-value: $e = 1.602\,176\,634 \times 10^{-19}\,\mathrm{C}$.

3.3.1. High power photoflash

The new flash purchased is a *Multiblitz X10AC/DC* with an energy of 1000 W · s that was the strongest studio flash on the market at at the time of purchase. The necessary electronics to start the flash at a prechosen time were built by J. Friedrich[22]. Fig. 3.8 shows the spectrum emitted by the flash in a wavelength range between 350 nm and 1050 nm. Most of the energy is emitted in the visible range, peaking at about 550 nm.

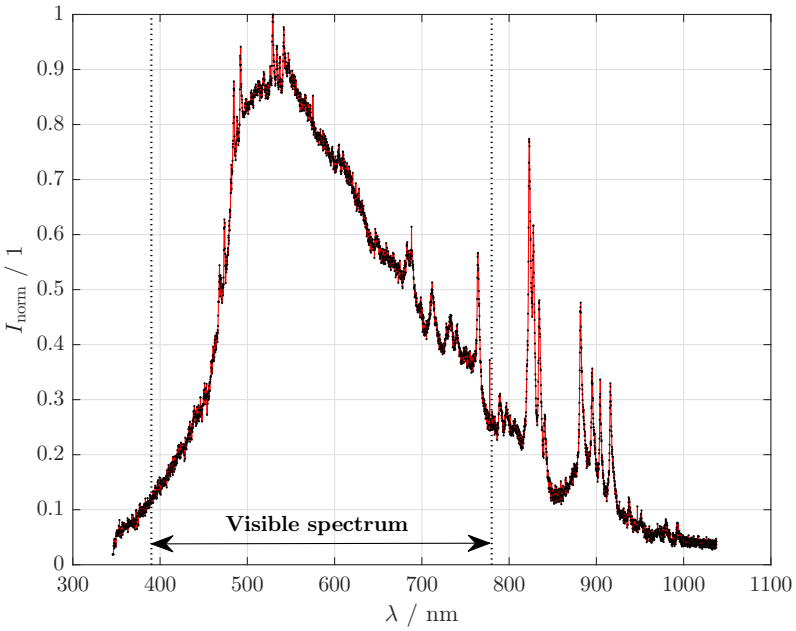

Figure 3.8.: Spectrum of the high-power photoflash *Multiblitz X10AC/DC* at maximum power level (PL 10): Normalized intensity I_{norm} as a function of wavelength λ. Spectrum acquired with an Ocean Optics USB4000 spectrometer.

Fig. 3.9 depicts the normalized intensity development as a function of time for different power levels (PL). Decreasing the power level to PL 9 reduces the maximum intensity to 60 % of the maximum achievable intensity. A further reduction to PL 8 leads to 40 % of maximum flash intensity. For thermal expansion measurements with the ohmic pulse-heating setup, a

[22]Institute of Experimental Physics, Electronics Workshop.

further power level reduction is by no means feasible, therefore, PL 7 to PL 1 are omitted in this graph. Note that reducing the power level also shifts the maximum flash intensity towards earlier times. To obtain high-contrast shadow images of the expanding wire samples, a maximized background illumination is desirable. For this reason, all expansion measurements in this work were conducted at the maximum power level (PL 10).

The inset in Fig. 3.9 shows a zoomed-in flash intensity at PL 10 as a function of time. The flash intensity varies by only $\pm 0.6\,\%$ of the mean intensity value over a 50 µs time interval ($220 \lesssim t/\mu s \lesssim 250$). Even with very strong gray filters applied in front of the pyrometer for widening the measurable temperature range, the time between pyrometer onset and saturation rarely

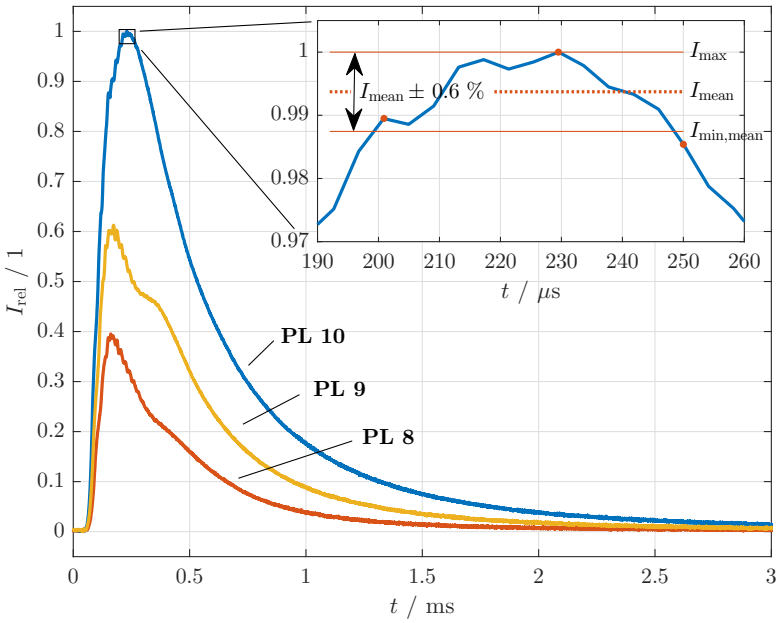

Figure 3.9.: Relative intensity I_{rel} as a function of time t of the high-power photoflash *Multiblitz X10AC/DC* at different power levels (PL). Measurements obtained with a pyrometer at a wavelength of $\lambda = 650\,nm$. The inset shows a zoomed-in region with maximum flash intensity at PL 10. The flash intensity remains constant with a deviation of approximately $\pm 0.6\,\%$ of the mean intensity I_{mean} in the time interval between 200 and 250 µs.

exceeds 25 µs. In fact, as a result of the high heating rates during pulse-heating, the pyrometer is typically only sensitive for as little as 10 µs to 20 µs. For this reason, measurements were timed such that the pyrometer onset approximately coincides with $t \approx 210\,\mu s$. By this means, the mean intensity deviation during a typical pyrometer measurement time decreases to less than $\pm 0.3\,\%$. This is favorable as a non-constant superposition of flashlight onto the pyrometer signal due to stray light would directly affect the derived temperature and thus induce a systematic error.

As outlined in Sec. 3.1.2, additional precautions are taken to minimize flash stray light reaching the pyrometer, such as an orthogonal direction for temperature and expansion measurement and the use of a notch-filter. Therefore, the influence of the flash characteristic on temperature measurement should only play a minor role.

3.3.2. Altered time sequence

The typical time sequence in pulse-heating used in previous works consisted of four steps [21]: Step 1, the flash (F) is started. Step 2, the camera sequence (C) is started. Step 3, the pulse-heating process is engaged (P1) and step 4, the pulse-heating is stopped (P2).

In principle, there is nothing wrong with this time sequence. However, when looking at the cup-shaped intensity profiles obtained in expansion measurements, a noticeable decrease in contrast can be observed during the measurement sequence. This is most likely related to a decay in phosphor screen sensitivity over measurement time. This circumstance is plotted in Fig. 3.10. The maximum intensity I_{max} of such a cup-shaped profile is related to the minimum intensity I_{min} and normalized. As can be seen, the contrast decays with ongoing time, i.e., as a function of image number. Considering that it takes approximately 20 µs until the sample temperature is high enough to be detected by the pyrometer, implies that no temperature can be attributed to the first eight images (2.5 µs per image). At image nine, indicated by a dashed red line, the contrast already decreased to 60 % of first-image-contrast. In other words, in the F-C-P1-P2 sequence, the images with highest contrast are useless because no temperature can be attributed

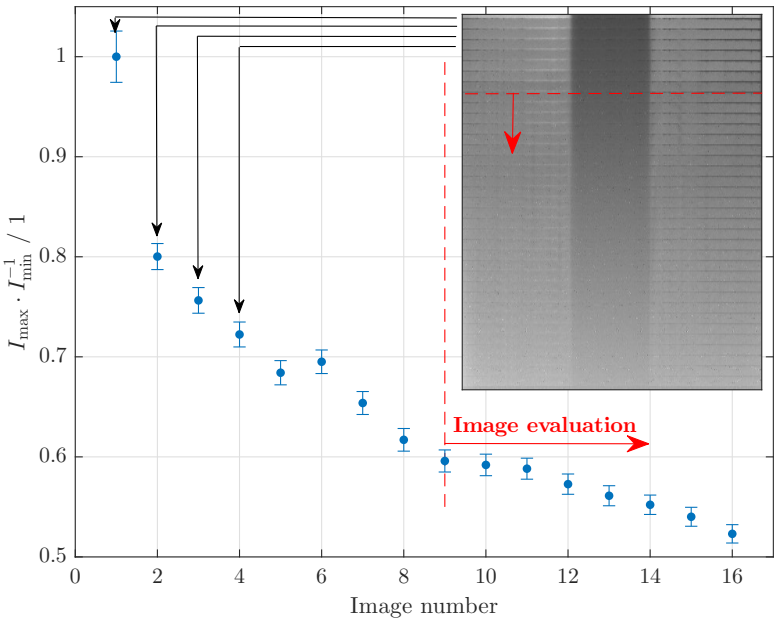

Figure 3.10.: Normalized wire contrast I_{max}/I_{min} in a typical image sequence. The inset shows a (vertically stretched) wire shadowgraph. The red dashed lines indicate the typical image at which a temperature allocation is possible for the first time in measurement, if the camera sequence is started prior to the pulse-heating start (F-C-P1-P2). A strong contrast reduction of the processable images is the result.

to them.
Therefore, camera start and pulse-heating start were swapped (F-P1-C-P2, compare Fig. 3.5). The time delay between pulse-heating start and camera sequence start is chosen such that the first image acquired is already in the pyrometer sensitive region.

Fig. 3.11 shows how changing the time sequence results in a strongly increased signal-to-noise ratio. The two expansion measurements depicted were acquired under the same experimental conditions, such as wire length and diameter, capacitor charging voltage, exposure time etc. The left expansion measurement was started shortly before the pulse-heating was started (previous sequence: F-C-P1-P2), while the right image acquisition started at

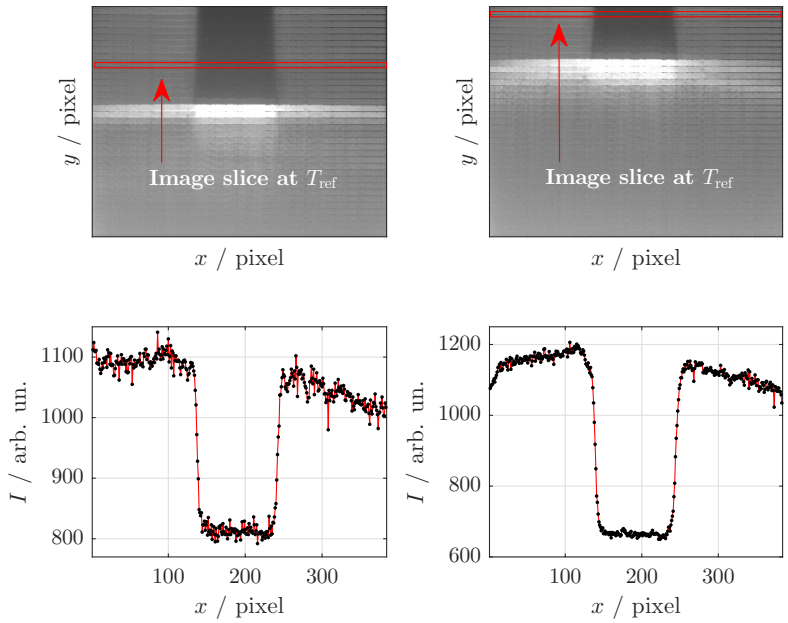

Figure 3.11.: Comparison of expansion sequence and corresponding cup-shaped intensity profile at the same reference temperature T_{ref}, obtained with different time sequences, F-C-P1-P2 (left) and F-P1-C-P2 (right). The F-P1-C-P2 sequence enhances the signal-to-noise ratio at a given temperature.
F ... flash start, P1 ... pulse-heating start, P2 ... pulse-heating stop and C ... camera start.

the pyrometer onset time (new sequence: F-P1-C-P2). The red frames mark the image slice at approximately the same time after the pulse-heating start, thus at the same reference temperature T_{ref}. Deriving the corresponding cup-shaped intensity profiles according to equation (3.9) illustrates how the data quality is increased by this simple measure. This measure is particularly useful if the experimenter wants to obtain thermal expansion values up to the boiling point, because the thermal radiation of the wire increasingly reduces the contrast as the temperature rises.

Ing. R. Dämon[23] designed a galvanic isolation device that was necessary to swap camera and pulse-heating start.

[23] Institute of Experimental Physics, Electronics Workshop.

4. Thermal Expansion Discrepancies in High-Pressure Experiments

The high-pressure vessel was put into operation to extend the accessible temperature range between the melting point and the sample's boiling point by raising the latter. By this means it was anticipated to resolve the non-linear nature of the density as a function of temperature when approaching the critical point. Resolving such a non-linear density behavior would greatly enhance the extrapolation validity.

However, T. Hüpf discovered in his doctoral thesis that the thermal radial expansion of two investigated materials (Nb and $Ni_{80}Cr_{20}$) was *higher* when measured with the high-pressure setup compared to that obtained with the low-pressure setup [52]. If at all, one might expect that the thermal expansion is slightly *lower* compared to that in low-pressure experiments, due to the high static pressure acting on the expanding sample. However, the compressibility of refractory metals is typically very low[1], and should only have a negligible effect on expansion measurement which makes these experiments feasible in the first place.

T. Hüpf performed various tests to investigate this phenomenon but did not find a reason for the observed discrepancy [52]. Hüpf pointed out that the trouble-shooting is inherently difficult due to the two experimental constraints that are closely linked to each other, the static *pressure* and the *atmosphere* used:

[1] compare Tab. 4.2.

1. Low-pressure experiments are performed in an inert *gas atmosphere* at almost *ambient pressure*. The pressure can not be varied on a large scale.
2. High-pressure experiments are performed in *water atmosphere* at *elevated pressures* (at least above the critical pressure of water, $p_{c,H_2O} = 220.64\,\text{bar}$ [56], to preclude boiling of the latter).

Switching between the two setups thus implies a change in pressure *and* a change in atmosphere used. Importantly, the physically intuitive assumption that the discrepancy has no physical reason but must be an artefact instead could be proven by T. Hüpf by monitoring the electrical resistivity of a sample in both setups. As the high-pressure setup is not capable of measuring electrical resistivity in absolute means, he first validated in experiments with the low-pressure setup that water as ambient medium has no impact on the sample's electrical resistivity. In a second step, he checked whether increasing the pressure in successive high-pressure experiments would affect the measurements of a resistivity related quantity[2]. No change in electrical resistivity was reported [52].

Fig. 4.1 (a) shows the relative volume expansion (squared relative radial expansion) of niobium and tantalum, measured during this work[3]. Full symbols represent data acquired with the high-pressure setup in H_2O at pressures between 1 kbar to 3 kbar, open symbols represent data acquired with the low-pressure setup in N_2 at 2.3 bar. The approximate deviation between the two data sets for each metal shows an increasing deviation with temperature, as depicted in Fig. 4.1 (b). This deviation is stronger for niobium than for tantalum, and reaches a value higher than $+25\,\%$ at the highest comparable temperature. While Fig. 4.1 (b) suggests that the data for niobium coincide at the beginning of the liquid phase, this is actually a result of the inadequate linear fit close to the melting temperature. The high-pressure data for tantalum deviate already by $+6\,\%$ at the melting point and further increase to $+16\,\%$ at the highest comparable temperature.

[2] In these experiments, the voltage drop was measured between current infeed and outfeed.

[3] Samples were cut from the very same wire material for low-pressure and high-pressure experiments.

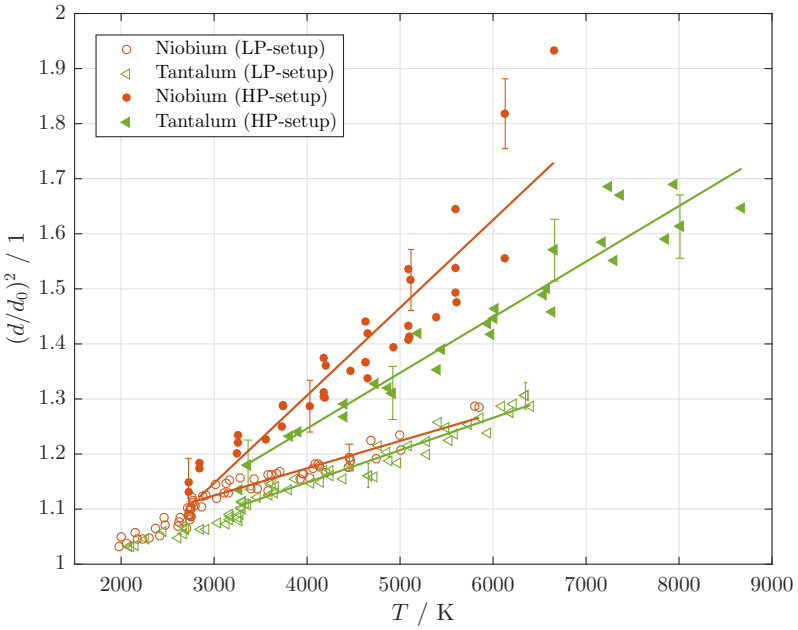

(a)

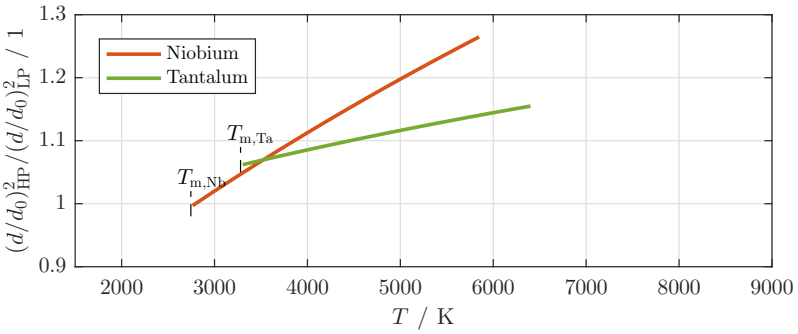

(b)

Figure 4.1.: Thermal expansion discrepancy between high-pressure and low-pressure experiments for Nb and Ta. (a) Measured relative radial expansion squared $(d(T)/d_0)^2$ (relative volume expansion) as a function of temperature T for niobium (circles) and tantalum (triangles) in high-pressure experiments (filled symbols, 1 kbar to 3 kbar, H_2O) and low-pressure experiments (open symbols, 2.3 bar, N_2). (b) Deviation between high-pressure and low-pressure experiments. The deviation increases with temperature.

4.1. Possible effects of changed conditions on measured quantities

As indicated above, changing between the two setups implies a change in atmosphere used *and* in pressure. In the following, possible influences of these two conditions on the monitored quantities, temperature and thermal expansion, are discussed.

4.1.1. Pressure

The high static pressure itself should not pose a problem for thermal expansion measurements as discussed below.

Possible influence of pressure on temperature measurement

CHANGE IN MELTING TEMPERATURE In high-pressure experiments it is usually argued to widen the liquid phase by greatly increasing the material's boiling point. However, the melting point of a material under pressure is also affected by a high static pressure. Tab. 4.1 lists the effects of pressure on the two metals Ta and Nb - the melting point increases with increasing pressure. For experiments up to 3000 bar (0.3 GPa) this implies a change in melting temperature of 7 K to 15 K for Ta, depending on the literature source considered, and a change of less than 11 K for Nb at 3000 bar.

Table 4.1.: Change in melting temperature T_m with pressure p for tantalum (Ta) and niobium (Nb).

Element	$dT_m \cdot dp^{-1}$ / $K \cdot GPa^{-1}$	Reference
Ta	(24 ± 2)	[64]
Ta	49	[65]
Nb	36	[65]

Fig. 4.2 shows the possible systematic error due to an increased, but unconsidered melting temperature for Ta in a worst-case scenario. The pyrometer signal was evaluated twice, assigning two different temperatures to the same plateau value. The solid blue line shows the resulting temperature without considering the change in melting temperature. The dashed blue line shows the temperature evaluated with the melting temperature increased by 15 K. Not considering the rise in melting temperature results in an underestimation of temperature, but the deviation, indicated by the solid red line, ranges between only $-0.3\,\%$ to $-1\,\%$ of the "true" value. Note that a change of 15 K is a rather conservative assumption, and newer values suggest only half of it for Ta (compare Tab. 4.1, [64]). Ignoring the effect of pressure on the melting temperature thus results in an effect that is one to two orders of magnitude too small to explain the measurement results.

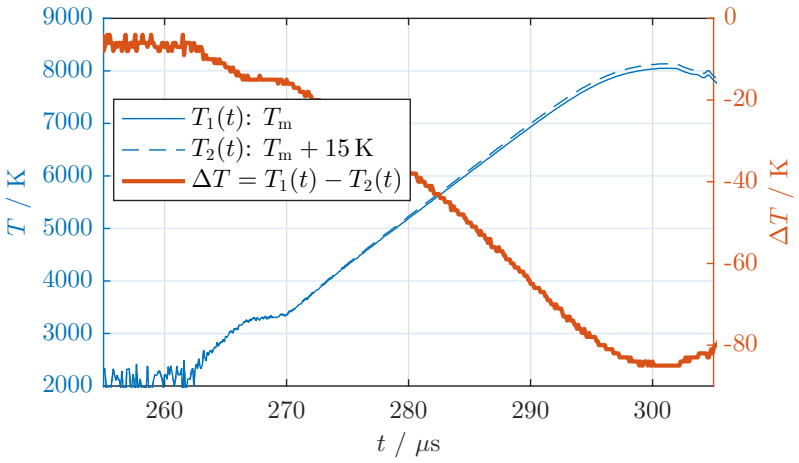

Figure 4.2.: Effect of a pressure-related increased melting point T_m on the temperature evaluation for Ta at 3000 bar. The blue lines show the temperature T as a function of time t assuming an unchanged melting point (solid line), and a melting point increased by 15 K (dashed line). The solid red line shows the temperature error ΔT that results if the rise in melting temperature is not considered.

Possible influence of pressure on thermal expansion measurement

COMPRESSIBILITY OF METALS A static pressure p acting on a metal wire may decrease its volume V, and thus its density. The relative volume change at a temperature T as the pressure is changed can be described via the material's isothermal compressibility κ_T,

$$\kappa_T = -\frac{1}{V} \cdot \left(\frac{\partial V}{\partial p} \right)_T . \tag{4.1}$$

Tab. 4.2 lists the isothermal compressibility of several metals investigated with the high-pressure setup in this work. One could argue that the relative volume change due to the increased static pressure ranges below $V/V_0 = -0.2\,\%$ for a typical static pressure of 1 kbar. The effect of a high static pressure on a metal's density is therefore negligible. Consequently, differences in the experimental data on different isobars are within experimental uncertainty intervals, as was also reported by Gathers et al. [25]. Independently, a high compressibility could only explain a *decreased* thermal expansion under high pressure compared to the expansion at lower pressure, but not an *increased* thermal expansion.

Table 4.2.: Isothermal compressibility κ_T at the melting point and percentual volume change $V \cdot V_0^{-1}$ per kbar for the metals niobium (Nb), tantalum (Ta), rhenium (Re) and iridium (Ir). Data from [66].

Element	κ_T / GPa^{-1}	$V \cdot V_0^{-1}$ / % · kbar^{-1}
Nb	0.0123	-0.123
Ta	0.0168	-0.168
Re	0.0092	-0.092
Ir	0.0082	-0.082

Furthermore, two other reasons exclude the high static pressure as potential explanation for an apparent enlarged thermal expansion:

First, the measured radial expansion sequence is related to a sequence that is acquired at the same static pressure prior to the pulse-heating start. Therefore, compressibility effects or a possible change in the optical path due to the increased static pressure are compensated for.
Second, high-pressure ohmic pulse-heating experiments were carried out in the past by other laboratories, such as at the *Lawrence Livermore Laboratory*, to obtain various thermophysical properties, including volume expansion (Gathers, Shaner, Hodgson, e.g. [25]). Comparing our data obtained at atmospheric pressure (low pressure-setup) with the literature (high-pressure data and data measured in vacuum) does not indicate a significant physical pressure dependence of the quantities measured [59].
However, a significant difference between the high-pressure setup used here in Graz and other high-pressure pulse-heating facilities is the medium used to build up pressure: Other groups use inert gases (Ar or He), not water, to exert pressure on the specimens.

Therefore, the problem seems to be related rather to the atmosphere used, than to the increased pressure itself, or there is some kind of setup-related systematic error that is made in conjunction with the high-pressure experiments.

4.1.2. Atmosphere

As indicated above, distilled water is used at the high-pressure pulse-heating setup in Graz to pressurize the sample chamber. Influences of the water atmosphere on the measured properties are imaginable.

Possible influence of atmosphere on temperature measurement

ABSORPTIVITY OF WATER The surface radiance emitted by the heated wire propagates through the water before reaching the pyrometer. If there is a time-dependent increase in absorptivity due to a temperature gradient evolving in the water, the measured surface radiance may be attenuated and yield apparent decreased temperatures.

The change of radiance intensity $I(x)$ relative to the incident intensity I_0 after traveling a distance x may be described with the LAMBERT-BEER-BOUGUER law,

$$I(x) = I_0 \cdot \exp(-\alpha(\lambda, T) \cdot x)\,, \tag{4.2}$$

where $\alpha(\lambda, T)$ is the absorptivity of the medium, that depends on the light's wavelength λ and the temperature T of the medium. According to [67], the absorptivity of water at the measuring wavelength of the pyrometer ($\lambda = 650\,\mathrm{nm}$) and at $T = 22\,^\circ\mathrm{C}$ is

$$\alpha_{650\,\mathrm{nm}} = (0.340 \pm 0.003)\,\mathrm{m}^{-1}\,.$$

However, the change in absorptivity of water with temperature in a range between 15 °C to 60 °C is reported to be as small as

$$\left(\frac{\mathrm{d}\alpha}{\mathrm{d}T}\right)_{650\,\mathrm{nm}} = (5 \pm 4) \times 10^{-5}\,\mathrm{m}^{-1} \cdot \mathrm{K}^{-1}$$

at 650 nm [68]. Considering a water temperature rise to 100 °C would therefore increase the absorptivity by approximately 1 %, but most likely only in a very thin tube around the wire.

This means, that the effect on temperature measurement of a possibly evolving dynamic temperature rise of the water surrounding the heated wire can be neglected.

Possible influence of atmosphere on thermal expansion measurement

WATER STEAM TUBE Conducting pulse-heating experiments in water, but without raising the static ambient pressure above the critical pressure of water would likely cause the formation of a water steam tube around the wire. On the recorded shadow images, this steam tube would not be identifiable as such, but rather appear like the expanding wire itself. Therefore, such an effect could explain an apparent enlarged thermal expansion.

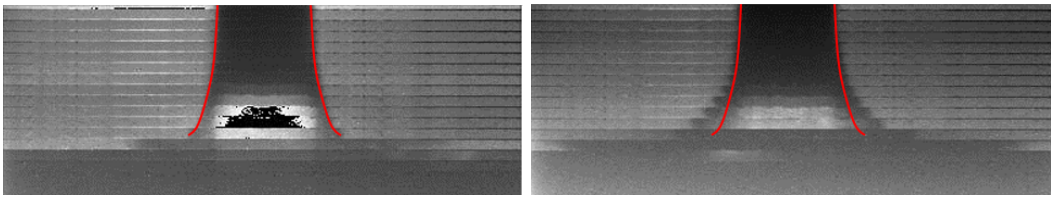

(a) (b)

Figure 4.3.: Expansion sequence of Nb obtained in water (a) at 1000 bar and (b) at 1 bar. The red lines indicate the evolution of the wire diameter that is found in the experiment at 1000 bar. A water steam tube emerges around the wire if the static pressure does not exceed the critical pressure of water and leads to an apparent enlarged expansion (b).

Fig. 4.3 shows the expansion sequence of two Nb wires that are heated in water under the same conditions such as wire length, wire diameter, load voltage, but with different static pressures present. Fig. 4.3 shows the expansion sequence of a wire in water pressurized to 1000 bar (a) and in water at 1 bar (b). The expansion sequence at 1 bar yields a higher thermal expansion than the sequence at 1000 bar. As indicated above, the most likely explanation is that a water steam tube is forming around the wire if the pressure does not exceed the critical pressure of water, as is the case for Fig. 4.3 (b). This experiment, that was repeated several times, indicates that some energy is transferred to the water during pulse-heating.

However, all thermal expansion experiments were conducted at pressures generously exceeding the critical pressure of water and thus resulting in expansion sequences similar to that depicted in Fig. 4.3 (b), which already show an increased expansion compared to experiments conducted in gas atmosphere at low-pressure.

INDEX OF REFRACTION Due to the heating of the wire and its resulting radial expansion, there could be a dynamic temperature and/or pressure increase in the water during the experiment. This may change the index of refraction of the water and might directly affect the expansion sequence due to refraction. Since this effect can happen under heating conditions only, referencing this "hot" image sequence to the "cold" image sequence captured before the experiment would introduce a systematic error.

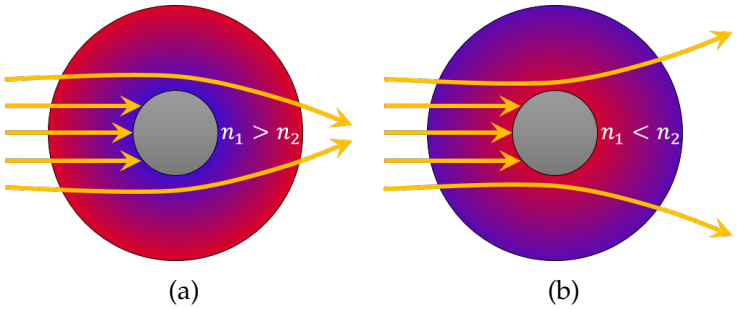

Figure 4.4.: Schematic representation of an index of refraction gradient in water surrounding a pulse-heated wire (grey circle) and the effect on passing light rays. (a) The inner region exhibits a higher index of refraction than the outer region. The light rays are refracted towards the optical axis. (b) The inner region exhibits a lower index of refraction than the outer region. The light rays are refracted away from the optical axis.

Fig. 4.4 schematically depicts the effect of light passing the wire if (a) the index of refraction close to the wire, n_1, is higher than the index of refraction at a greater distance to the wire, n_2, or vice versa (b). The blue color represents a region with a high index of refraction.

To investigate this potential problem, T. Hüpf performed tests, where he guided a laser beam close-by the heated wire and monitored its position on the CCD camera throughout a pulse-heating experiment. No deflection of the laser beam was observed. However, given the intuitive plausibility of this hypothesis and the fact that no experimental details were given, makes complementary investigations inevitable to preclude this effect as potential error source.

4.1.3. Systematic error

Besides the changed conditions, pressure and atmosphere, a systematic setup-related error could be the cause for the observed apparent enlarged expansion.

Possible systematic effect influencing the temperature measurement

FLASH STRAYLIGHT The high-pressure vessel has only two windows, as opposed to three in the low-pressure sample chamber. Therefore, no separate window for temperature measurement is present. As a consequence, the high-pressure experiments either have to be split in separate temperature and thermal expansion measurements, or a beam-splitter has to be used at the exit-window to permit simultaneous measurements. The second approach is preferable, since it doubles the time efficiency compared to separate experiments. Furthermore, the temperature-expansion behavior is measured in the very same experiment and not matched over time. However, several problems arise choosing this approach.

One of these problems is a temperature error that can be introduced, if flash straylight reaches the pyrometer. The measured signal is then a superposition of the wire's surface radiance with the straylight. Therefore, a notch filter was acquired (*Chroma* ZET647NF, FWHM $\approx$ 34 nm), to filter light at the pyrometer wavelength out of the flashlight. Problematically, no notch filters with an FWHM slightly higher than that of the pyrometer's interference filter[4] were available off the rack, resulting in a small yet non-zero remaining straylight intensity reaching the pyrometer's sensor. As a consequence, it was tried to subtract a flash-"baseline" that was recorded prior to the pulse-heating experiment from the pyrometer signal obtained during heating. Two problems occurred testing this approach:

1. The flash intensity shows variations of up to $\pm 5\,\%$ in successive experiments, thus another systematic error is introduced when subtracting a flash baseline from the pyrometer signal obtained during pulse-heating.
2. As the wire expands during pulse-heating, the amount of straylight reaching the pyrometer is smaller than in unheated conditions. Hence, the subtracted baseline signal is too large, the temperature evaluated therefore too high.

[4] Compare Tab. 3.1.

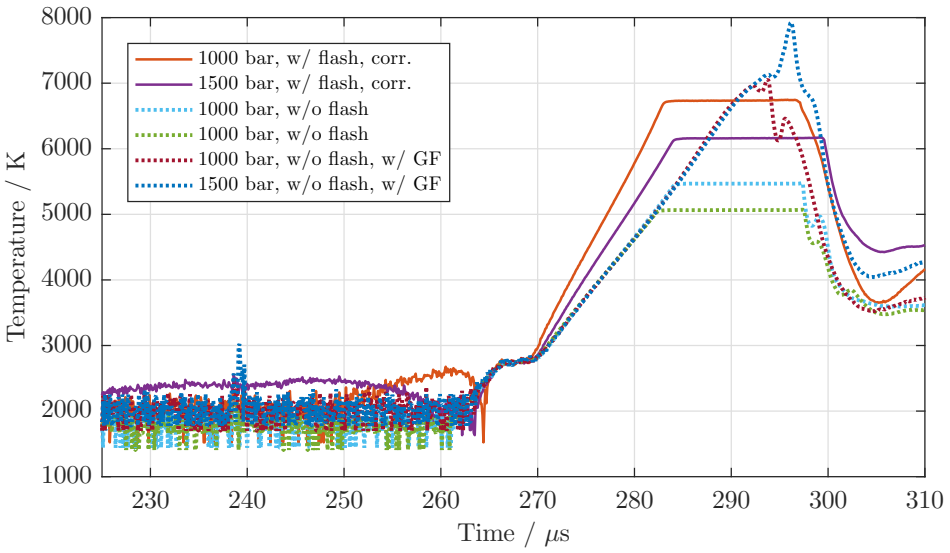

(a)

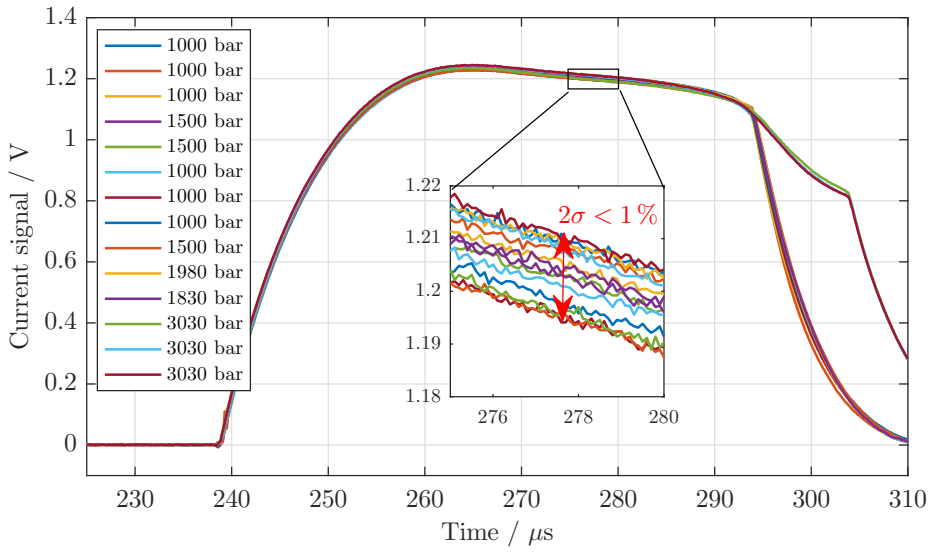

(b)

Figure 4.5.: Temperature and current reproducibility in high-pressure experiments. (a) Using a flash-baseline subtraction delivers erroneous temperature traces (solid lines), while the absence of flashlight yields highly reproducible temperature curves (dotted lines). (b) The current traces show a high reproducibility and can be used as plausibility check when performing a time-matching between separate temperature and expansion measurements.

Fig. 4.5 (a) shows the temperature as a function of time for different experiments on niobium. The distance between the wire contacts and the load voltage were kept constant. The solid lines indicate temperatures that result from the above described baseline subtraction. Resulting temperature traces are highly irreproducible and yield temperatures that are too high. Dotted lines show the evaluated temperature signal that results if the flash is not triggered (separate temperature measurement). The resulting temperature traces are highly reproducible for successive experiments. In some experiments, gray filters (GF) were used to resolve the highest temperatures, while in others, the temperature traces are capped due to the saturation voltage of the pyrometer's photo diode. The dotted green line was obtained with a direct pyrometer view, all other traces were recorded via the beam-splitter. No difference in evaluated temperature is visible.

Fig. 4.5 (b) shows the raw current signals as a function of time for various experiments on niobium (including the experiments shown in Fig. 4.5 (a)). Because of the fixed sample length and the unchanged load voltage, the current traces are highly reproducible. Furthermore, the data show no pressure dependence in the investigated pressure regime.

Given the high reproducibility it was decided to conduct temperature and thermal expansion experiments separately and time-match the obtained data afterwards. The acquired current traces serve as plausibility check. Note that this decoupled measurement approach has further advantages over the simultaneous measurement of temperature and thermal expansion. First, the beamsplitter is not needed in expansion measurements, it can be moved out of the way - the intensity reaching the camera is thus increased which is advantageous for expansion measurements. Second, the notch filter becomes irrelevant because there is no need for flash light in exclusive temperature measurements. This also increases the background illumination intensity and enhances the signal-to-noise ratio in acquired shadow images.

Possible systematic effects influencing the expansion measurement

LINEARITY Another systematic effect could be a nonlinear behavior of the imaging system. Thankfully, the linearity of the system can be easily checked by acquiring shadow images of unheated wires with different diameters.

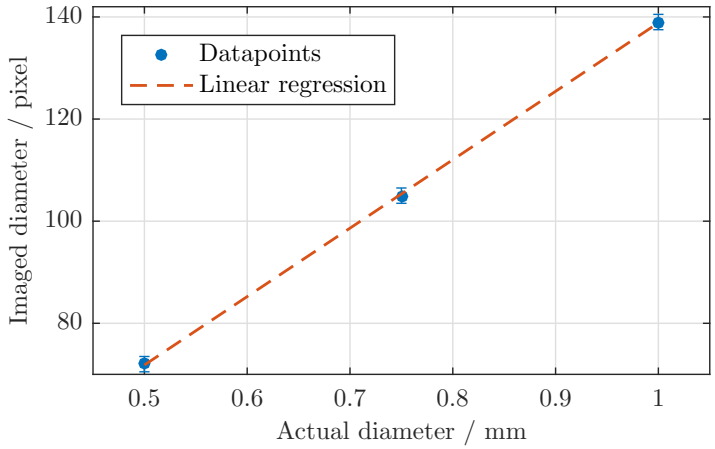

Figure 4.6.: Linearity check of the imaging system used in the high-pressure setup. Data points imaged at a pressure of 1000 bar. Uncertainties represent a 95 % confidence interval. The imaging system behaves linearly.

This was done for wires with diameters of 0.5, 0.75 and 1.0 mm. As plotted in Fig. 4.6, the imaging system behaves linearly.

WIRE MOVEMENT A moving wire is always a source for potential systematic errors in thermal expansion measurements. While a wire movement perpendicular to the camera axis can be diagnosed easily, a movement towards or away from the camera could be difficult to recognize and may yield apparent enlarged expansion values.

Measures to ensure a non-moving wire are:

1. Increase the stability by using short wires ($\approx$ 40 mm length).
2. Prevent bending of the wire due to axial expansion caused by a heating rate, that is too low.
3. Prevent lateral forces acting on the wire by ensuring vertical alignment.

From this perspective, either a changing index of refraction, or a wire movement remain as possible candidates to explain the thermal expansion discrepancy.

4.2. Discrepancy of the discrepancy - consistent expansion for Ir and Re

High-pressure expansion data under water atmosphere for the metals niobium and tantalum, showing a thermal expansion discrepancy, were shown already in Fig. 4.1. Such experiments were also conducted for the metals iridium (Ir) and rhenium (Re). Interestingly, the above discussed discrepancy does not occur for neither iridium nor rhenium as shown in Fig. 4.7. Within experimental uncertainty, the data sets obtained in nitrogen with the low-pressure setup (open symbols) are equal to the expansion data acquired in water with the high-pressure setup (filled symbols). High-pressure data for both metals were acquired at pressures between 2 kbar to 3 kbar.

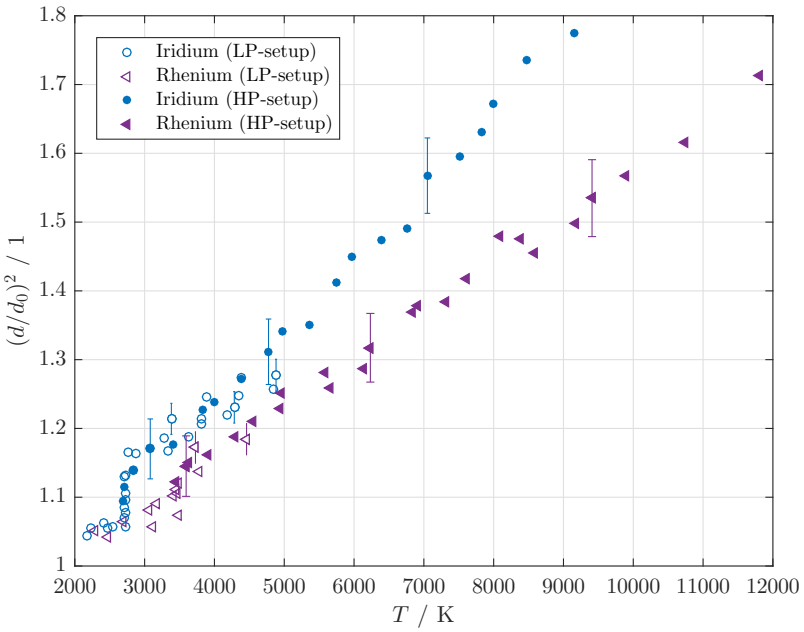

Figure 4.7.: Relative thermal radial expansion squared $(d(T)/d_0)^2$ (relative volume expansion) as a function of temperature T for iridium (circles) and rhenium (triangles) in high-pressure experiments (filled symbols, 2 kbar to 3 kbar, H_2O) and low-pressure experiments (open symbols, 2.3 bar, N_2). No discrepancy between the low-pressure and high-pressure data sets are observable.

4.3. Further investigations

While a thermal expansion discrepancy was observed for the metals niobium and tantalum, no such discrepancy could be found for iridium and rhenium - these two metals behaved consistently, independent of the pulse-heating setup used. If a change in the index of refraction throughout an experiment would cause the discrepancy, this would imply that different metals act differently on the water. Imaginable explanations for this could for instance be a very different thermal conductivity that allows a different amount of heat to flow into the water, changing its refractive index. In any case, similarities or distinctions between the two groups should be visible when comparing their thermophysical properties.

4.3.1. Comparison of thermophysical properties and experimental parameters

Fig. 4.8 shows a comparison of the thermophysical properties specific enthalpy $H(T)$, electrical resistivity $\rho_{\mathrm{el}}(T)$, thermal diffusivity $a(T)$ and thermal conductivity $\lambda(T)$ for the metals Nb, Ta, Ir and Re. a and λ data are given in the liquid phase only, with iridium as exception. No trend towards clustering into the groups Ir, Re and Nb, Ta is visible for any property.

Tab. 4.3 lists the specific heat capacity in the liquid phase for these metals. No grouping can be seen in the specific heat capacity. When calculating the absolute heat capacity C_{p} for predefined geometric dimensions via the room temperature density, it becomes obvious that Ir and Re exhibit a 30 % to 60 % higher C_{p} than Nb and Ta. However, the sample's heat capacity should not affect the properties of the surrounding medium, but only affect the amount of energy needed to raise the sample's temperature and thus reach the boiling point.

From this perspective, a dynamic gradient in the water's index of refraction seemed rather unlikely, because it should occur independently of the metal investigated.
However, when comparing the heating rates applied for the different metals, it becomes obvious that a smaller heating rate was achieved for the

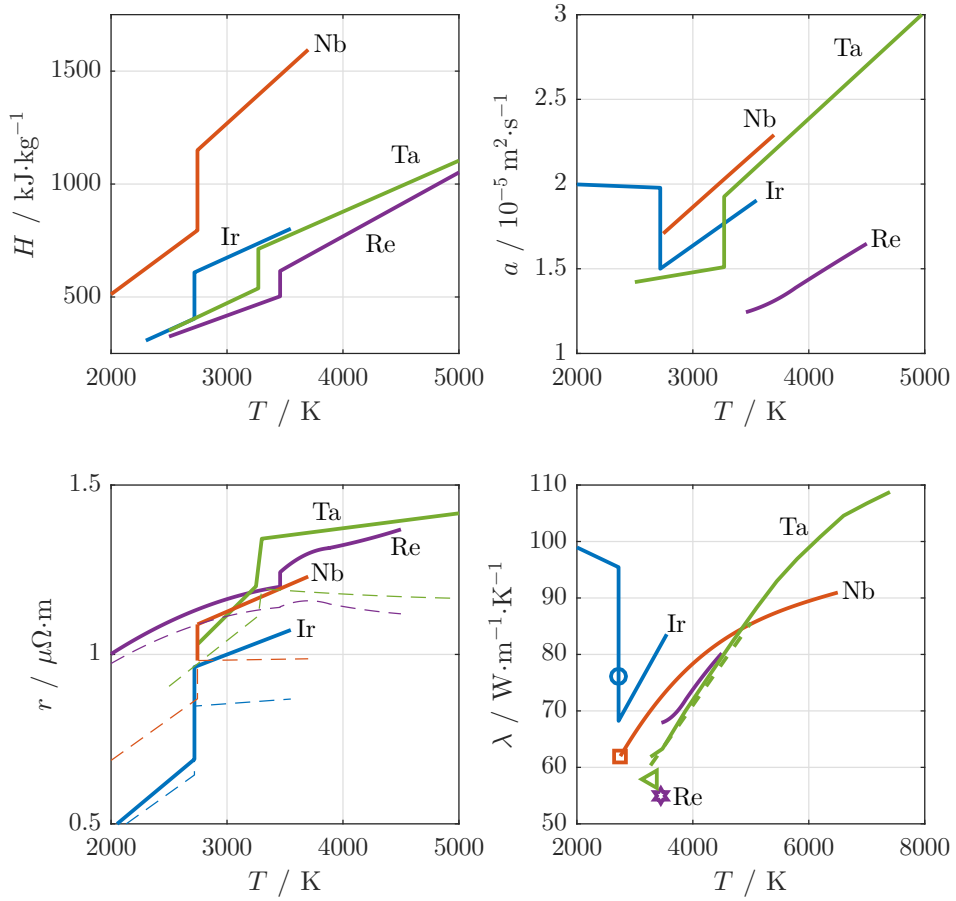

Figure 4.8.: Comparison of thermophysical property data as a function of temperature T for the metals Nb, Ta, Ir and Re. Clockwise starting from the top left graph: Specific enthalpy H, thermal diffusivity a, thermal conductivity λ and electrical resistivity r. The dashed lines in the $r(T)$ plot depict uncorrected resistivity data of the respective metals. Data on Nb by Wilthan et al. [69] except for $\lambda(T)$ which was derived using r-data given by Gallob et al. [70] and the Wiedemann-Franz-law (WFL). Data on Ir by Cagran and Pottlacher [71]. Data on Re by Hüpf et al. [72], data for a and λ derived via WFL. Data on Ta by Pottlacher and Seifter [23] and by Jäger et al. [73] (solid green line in $\lambda(T)$ plot). Symbols in $\lambda(T)$ plot are recommended values by Mills et al. [74] for the beginning of the liquid phase.

Table 4.3.: Comparison of the specific heat capacity c_p and the absolute heat capacity C_p for liquid Nb, Ta, Ir and Re wires with 0.5 mm diameter and 40 mm length. The absolute heat capacity is calculated from the sample's mass m via the room temperature density ρ_0 and its geometric dimensions.

	ρ_0 / kg · m^{-3}	Ref.	m / g	c_p / J · kg^{-1} · K^{-1}	Ref.	C_p / 10^{-2} J · K^{-1}
Nb	8570	[75]	0.067	466	[69]	(3.13 ± 0.02)
Ta	16 654	[76]	0.131	226	[23]	(2.95 ± 0.02)
Ir	22 560	[77]	0.177	233	[71]	(4.13 ± 0.03)
Re	21 020	[76]	0.165	283	[64]	(4.67 ± 0.03)

problematic metals Nb and Ta, than for Ir and Re, compare Fig. 4.9. While heating rates of approximately 2×10^8 K · s^{-1} were reached for Nb and Ta, values between $(4 \text{ to } 5) \times 10^8$ K · s^{-1} were achieved for Ir and Re.

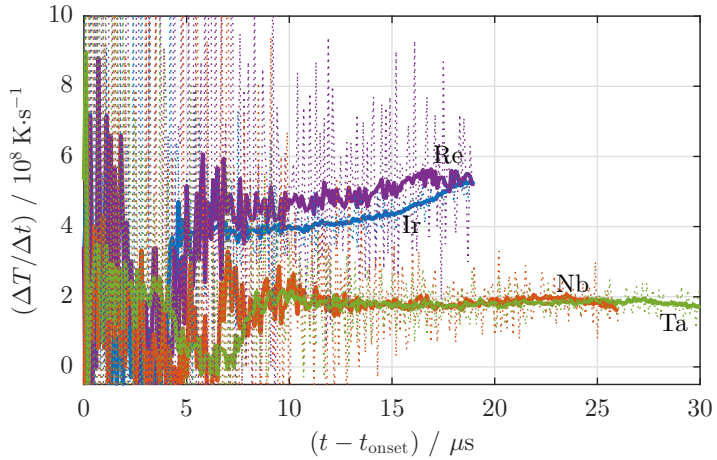

Figure 4.9.: Smoothed heating rates $(\Delta T/\Delta t)$ as a function of time $(t - t_{\text{onset}})$, with t_{onset}, the pyrometer onset temperature in typical high-pressure experiments. The heating-rates for the metals showing no thermal expansion discrepancy (Ir, Re) is higher by a factor two than the heating-rates for the metals showing the discrepancy (Nb, Ta).

These considerations support the speculation that the discrepancy may be a systematic effect due to a moving wire.

4.3.2. Ensuring a non-moving wire

The above speculations support the hypothesis of a potentially problematic sample-holder that may introduce a lateral force acting on the wire. In this sample holder, a little protruding nose is used to tension the wire by firmly pulling it over said nose while it is clamped on the other end. Once the wire is tensioned and completely upright, the wire is also fixed at this end. Using this approach for metals with a very high stiffness, such as Ir and Re, produces highly problematic expansion sequences with inclined flanks because a lateral force is introduced into the wire. This force is freed once the wire becomes liquid. Evaluating such an expansion sequence can lead to an apparent increased expansion of up to 17 %. Data for Ir and Re were thus acquired without tensioning the wire over the above mentioned nose. Due to their high stiffness, these wires could be mounted upright and force-free without tensioning them. In the case of Ta and Nb, exhibiting lower stiffness values, the tensioning turned out to be necessary in order to produce an apparent valid expansion sequence[5].

The assumption was that Ta and Nb wires may move along the imaging axis due to a sample-holder induced lateral force acting on the wires. As a result, the sample holder was modified to meet the following demands:

1. Provide a possibility to tension the wires without introducing a lateral force,
2. Ensure central and vertically upright positioning of wire,
3. Electrodes must be easily changeable,
4. Use as much as possible of the original sample holder.

The result is depicted in Fig. 3.4 (b). The electrodes used were adopted from the low-pressure setup. They are drilled into brass pieces that connect the sample holder to the discharge circuit and are as such easily changeable. At the upper sample holder side, a small bore allows to vertically feed the

[5]Using the same approach as with Ir and Re results in moving wires.

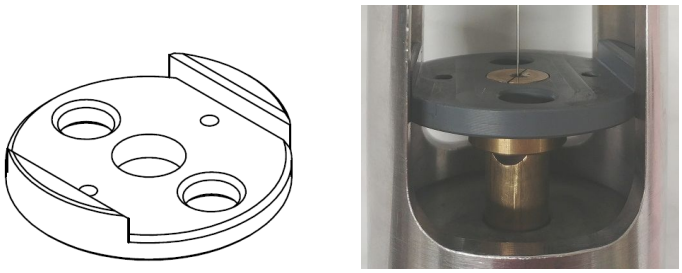

(a) (b)

Figure 4.10.: (a) Centering disc to ensure perfect vertical alignment of the electrodes and thus the wire. (b) Application of the centering disc on the lower electrode in a high-pressure sample-holder.

wire through the sample holder. The wire is fixed at the bottom via a brass clamp. The tensioning of the wire is done via the big recess hole in the upper electrode where the tensioning force is now acting along the wire axis, but not lateral to it as before. The specimen is then cut off from the wire in this hole.
In addition, a centering disc (CD) was CNC-machined to ensure absolute vertical symmetry, compare Fig. 4.10.

Experiments on Nb at a static pressure of $p = 1\,\mathrm{kbar}$ were repeated with the *new sample holder* and for *different heating rates* ($\Delta T/\Delta t$):

- $\approx 2.0 \times 10^8\,\mathrm{K \cdot s^{-1}}$ Same heating rate as previously, compare Fig. 4.1
- $\approx 2.9 \times 10^8\,\mathrm{K \cdot s^{-1}}$ Increased heating rate
- $\approx 4.6 \times 10^8\,\mathrm{K \cdot s^{-1}}$ Further increased heating rate, w/o and w/ CD

Care was taken to only change one parameter or condition at a time. Fig. 4.11 depicts the result and relates it to the previously obtained low-pressure and high-pressure data (compare Fig. 4.1).
Comparing the filled green circles to the filled grey circles, both acquired at the same heating rate, indicates that the mounting mechanism of the old sample holder (SH) poses no problem for Nb - the data perfectly coincide.
Increasing the heating rate (squares and triangles) leads to a small decrease in the slope of thermal expansion data, but using the centering disc (CD) seems to again shift the data up to higher values.

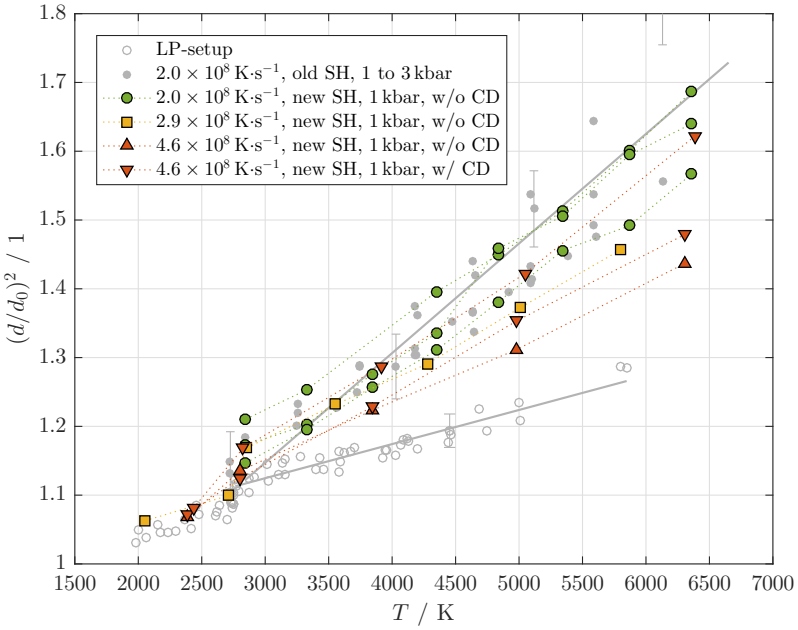

Figure 4.11.: Influence of an adapted sample holder (SH), ensuring absence of lateral forces, and increased heating-rates on the thermal expansion $(d/d_0)^2$ of Nb as a function of temperature T at 1 kbar in water. CD indicates the use or non-use of a centering disc. Neither the old sample holder, nor too low heating-rates can explain the discrepancy between data obtained with the high-pressure setup and data obtained with the low-pressure (LP) setup.

The statistics are not sufficient and the question remains whether the heating rate has a significant influence on apparent thermal expansion data, but the conclusion can be drawn that the discrepancy between high-pressure expansion data in water and low-pressure expansion data in nitrogen remains, independently of measures taken to avoid a wire movement - neither the old sample holder, nor potentially too-low heating rates can explain the observed apparent enlarged expansion.

Note that in these experiments, some data points for the thermal expansion at the end of the solid phase were captured as well. Interestingly, the discrepancy seems to be very small or even absent prior to the melting transition.

At this point it becomes striking how inferior the precision of these data is compared to data acquired with the low-pressure setup. As the sample holder and the heating-rates can be eliminated from the trouble-shooting process, the only remaining hypothesis to explain the thermal expansion discrepancy is that of a dynamically changing index of refraction.

4.3.3. Index of refraction

With all other potential effects made implausible, the hypothesis of a changing index of refraction during the heating experiment is the only potential problem remaining. The question is: How is the index of refraction $n(T, p)$ affected by a temperature and/or pressure change and how does this change affect the acquired wire image.

Effect of temperature and pressure on the index of refraction

The effect of temperature on the index of refraction of H_2O is plotted in Fig. 4.12 (a) for different isobars (wavelength $\lambda = 514.5\,\text{nm}$). At each of these isobars, the index of refraction decreases with increasing temperature, until the boiling point at the given pressure is reached and the index of refraction drops discontinuously[6] to $n \approx 1$, its value in the vapor phase. Above the critical pressure of water, the index of refraction drops continuously. The higher the temperature, the bigger the change in refractive index with pressure and temperature. At 20 °C, a change from 500 bar to 1000 bar increases the index of refraction by 0.48 %. The same increase in pressure at a temperature of 500 °C yields an increase of 8.3 % in n.

Fig. 4.12 (b) depicts a simplified drawing of the wire with two circular regions around it. If the temperature close to the wire is heated to a temperature T_1, while the region at a greater distance to the wire remains at the cooler temperature T_2, light emitted from the wire would be refracted away from the optical axis, since $n_1 < n_2$.

[6]Note that the jump plotted here is not discontinuous due to the insufficient data resolution.

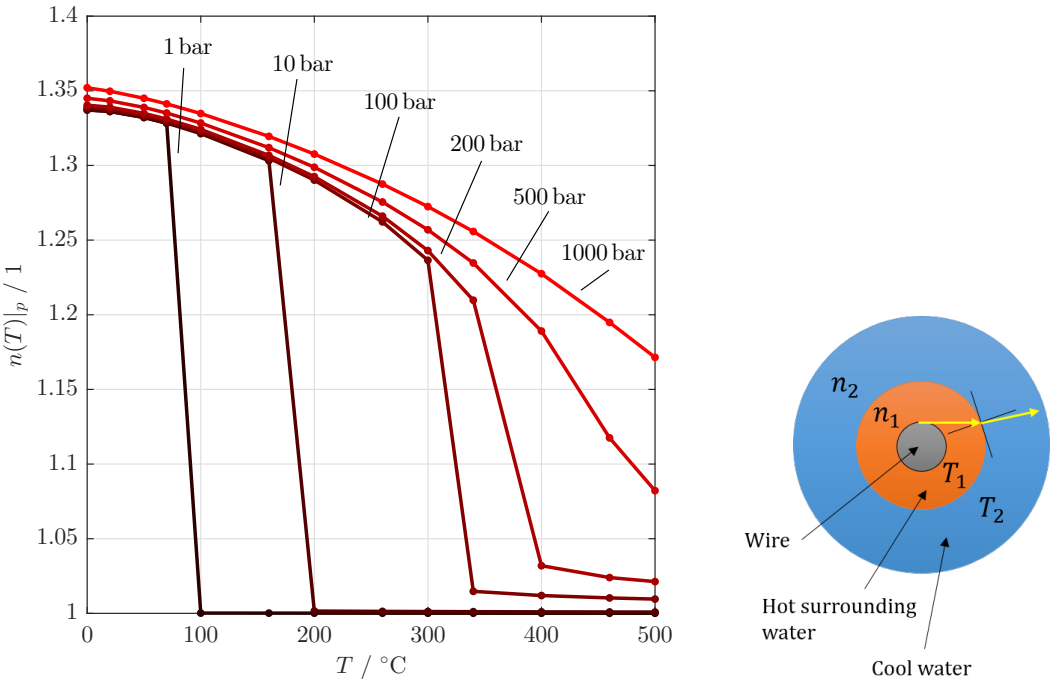

(a) (b)

Figure 4.12.: (a) Index of refraction $n(T)|_p$ of H_2O as a function of temperature T for different isobars. Data taken from [78]. (b) Simplified model of refraction at an interface with discrete jump in index of refraction, where $T_1 > T_2$, thus $n_1 < n_2$.

Fig. 4.13 shows the effect of pressure on the index of refraction of H_2O on different isotherms at $\lambda = 514.5\,\text{nm}$. The index of refraction increases with increasing pressure. The change in index of refraction with pressure is higher for higher temperatures. At a pressure of 500 bar, a temperature rise from 20 °C to 500 °C decreases the index of refraction by 19 %. At a pressure of 1000 bar, the same rise in temperature decreases the index of refraction by 13 %.

Fig. 4.13 (b) depicts the path of light that is emitted from the wire, if the pressure in a tube close to the wire, p_1, exceeds the pressure that is pertinent at a greater distance, p_2. As in this case $n_1 > n_2$, the light is refracted

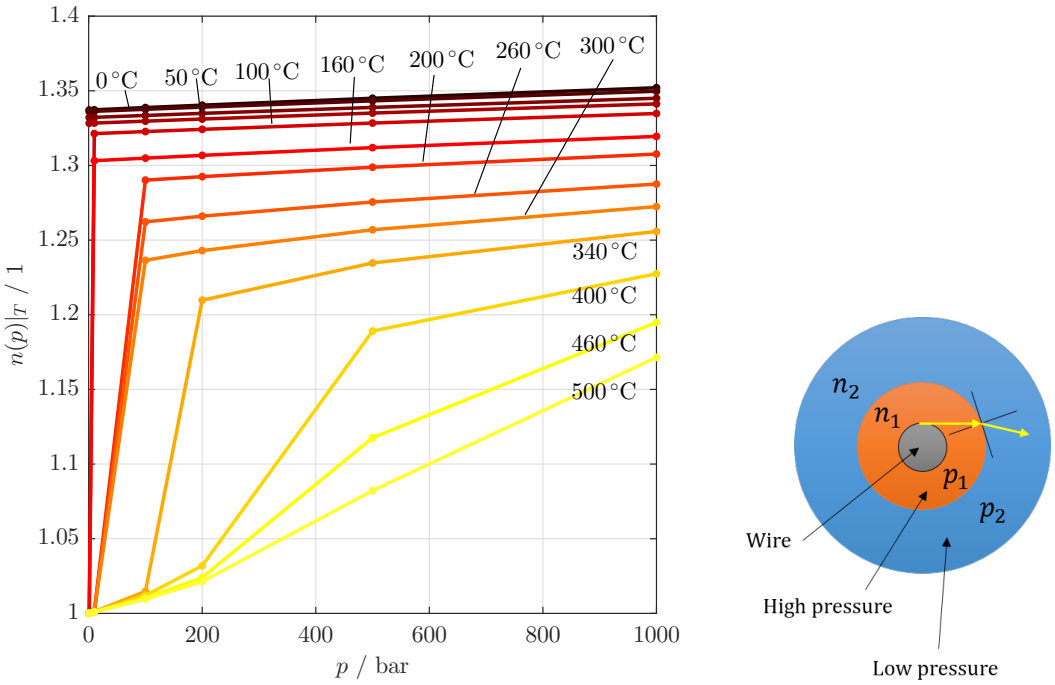

(a) (b)

Figure 4.13.: (a) Index of refraction $n(p)|_T$ of H_2O as a function of pressure p for different isotherms. Data taken from [78]. (b) Simplified model of refraction at an interface with discrete jump in index of refraction, where $p_1 > p_2$, thus $n_1 > n_2$.

towards the optical axis. Pressure and temperature have an opposite effect on the index of refraction of water. The next step is to investigate how these different effects affect the imaging of the wire.

Raytracing simulation in a toy system

To investigate the effect of a changing index of refraction as a consequence of a temperature rise, a simplified ray tracing simulation[7] was conducted.

[7] `https://ricktu288.github.io/ray-optics/simulator/`.

The aim was to show the principle direction of refractive index effects acting on the resulting image size. For that purpose, point sources at the edges of the wire were used to construct the image of these points, as indicated in Fig. 4.14.

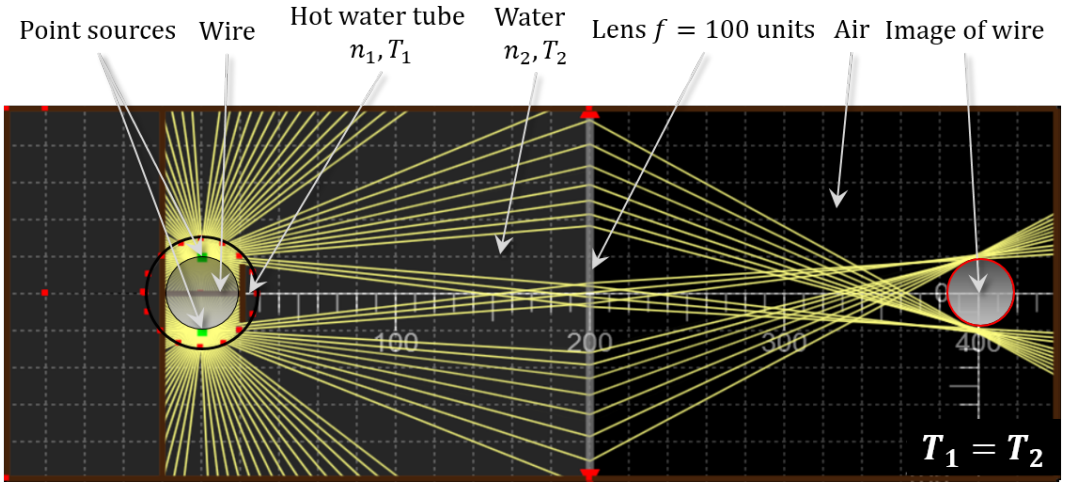

(a) $T_1 = T_2 \quad \Rightarrow \quad n_1 = n_2 = 1.35$

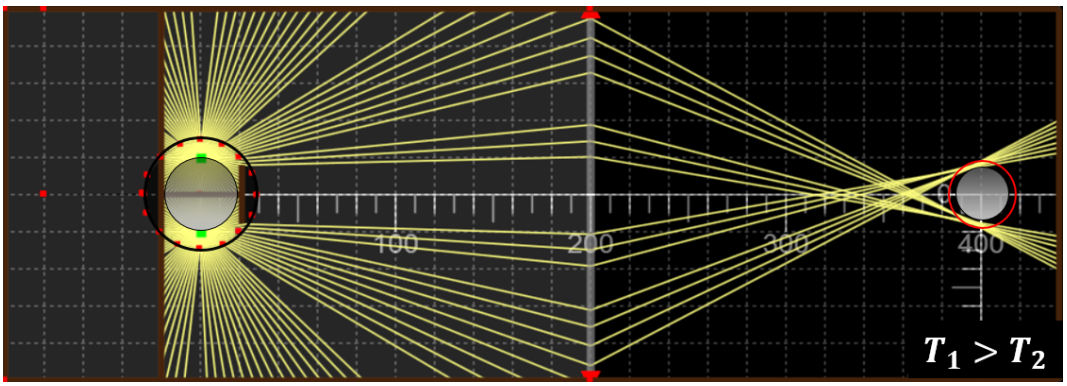

(b) $T_1 = 550\,°\text{C} > T_2 = 20\,°\text{C} \quad \Rightarrow \quad n_1 = 1.10 < n_2 = 1.35$

Figure 4.14.: Raytracer simulation to study the effect of a hot water tube surrounding the wire on the image size. (a) If no temperature difference is present, a certain image size results. (b) If the water tube around the wire is hotter than at a farther distance, the image size is decreased compared to case (a). Refractive indices at indicated temperatures and a pressure of 1 kbar taken from [78].

Fig. 4.14 (a) shows the simulation for the case where no water temperature difference is present. A certain image size is the result. Fig. 4.14 (b) depicts the effect of a hot water tube evolving around the wire on the image size. In this case, the resulting image size is decreased compared to case (a), where no temperature difference was present.

This simulation proves that a hot water tube around the wire can not explain the apparent increased expansion observed in high-pressure experiments, but would lead to an apparent decreased expansion. As the effect of pressure on the index of refraction acts in the opposite direction, a dynamic pressure increase as depicted in Fig. 4.13 (b), could explain the observed thermal expansion discrepancy.

Note that an absolute raytracing simulation is very difficult, if not impossible without knowing precise conditions of the system, such as the time evolution of the temperature and pressure gradient in the tube surrounding the water, and also the diameter of this tube. Without knowing these conditions, deviations in light path[8] are estimated to be variable between 0° to 20°.

Laser experiments

T. Hüpf performed laser experiments in the past, where he shot a laser close by a heated wire, but did not find a deviation of the laser spot that would indicate a dynamic change in the index of refraction [52]. However, given the above considerations, it was decided to repeat the experiments. A schematic depiction of the experimental setup can be seen in Fig. 4.15. A laser[9] is shot into the high-pressure (HP) chamber. Two kind of experiments were performed on niobium at a static pressure of 1 kbar and at a heating rate of $4.6 \times 10^8\,\mathrm{K \cdot s^{-1}}$:

1. *Diffraction* experiment: Laser hits wire directly.
2. *Refraction* experiment: Laser passes wire in a small distance.

[8] Calculation using SNELL's law: Angle of refraction as a function of angle of incidence for different temperatures.

[9] 5 mW at a wavelength of 635 nm.

In both cases, the manipulated laser light was monitored with the system's CCD-camera, using an exposure time of 1 µs.

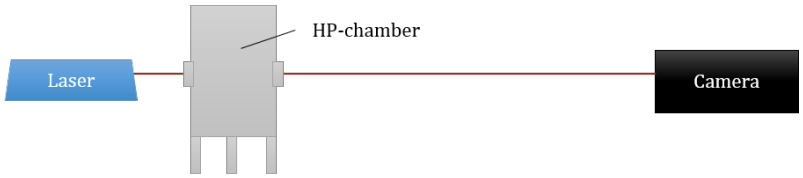

Figure 4.15.: Schematic setup for laser diffraction and refraction experiments to investigate a potential change in index of refraction during pulse-heating experiments. No lenses are used in the optical path in order to avoid a widening of the laser beam.

DIFFRACTION EXPERIMENTS A diffraction pattern emerges if the laser hits the wire directly. The change of this pattern, i.e., the relative distance of the peaks, was monitored throughout pulse-heating experiments on Nb at 1 kbar. Fig. 4.16 (a) and (b) show the result for two experiments. The distance between the diffraction peaks of the heated wire (thick colored lines) decreases as the temperature increases.

Possible explanations for this behavior are either a change in refractive index, with a pressure gradient present, or the diffraction is merely caused by the change of wire diameter itself. According to BABINET's principle, the opaque wire with diameter d acts identically to a slit with width d - as such, an increasing wire diameter due to thermal expansion would decrease the distance between the diffraction peaks, much like a wider slit would produce diffraction peaks being closer to each other. Therefore, the question arises whether the observed diffraction pattern can be explained by thermal expansion only.

If *yes*, there is no change in the refractive index during heating, but if *no*, there must be some kind of change in the optical path and as such a change in the index of refraction.

To tackle the problem, the effect of a potential change in the refractive index was eliminated from the experiment, by investigating the diffraction pattern of *unheated* wires but with different diameters, again in water at 1 kbar, and comparing it to the corresponding diffraction pattern of the *heated* wire. The

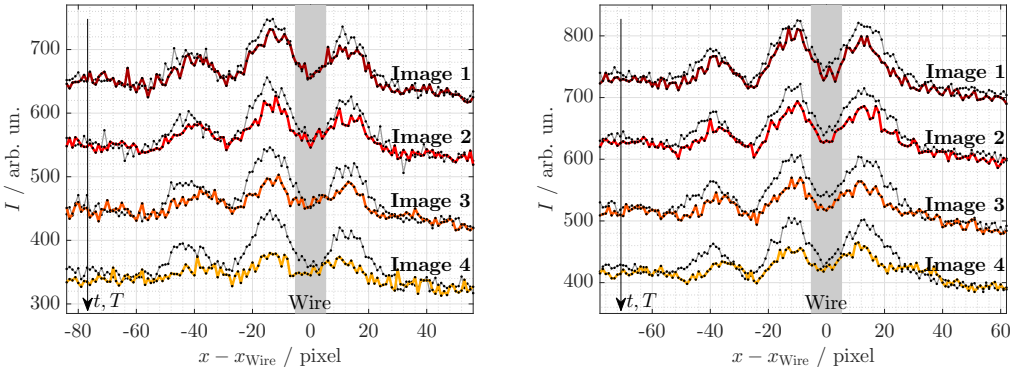

Figure 4.16.: Laser diffraction pattern of two pulse-heated niobium wires (a) and (b) at 1 kbar - intensity I as a function of relative pixel position $x - x_{\mathrm{Wire}}$. Thin grey lines indicate the intensity signal of the respective image prior to pulse-heating. Colored thick lines show the diffraction pattern caused by the heated wire. Time t and temperature T increase from top to bottom. The distance between the diffraction peaks decreases as the temperature increases.

referencing temperature was chosen at 7000 K, which corresponds to image 4 in Fig. 4.16 (a) and (b).

Two wires were processed to exhibit the diameters that the low-pressure nitrogen and the high-pressure water experiments suggest at 7000 K. For this purpose, expansion data as given in Fig. 4.11 were extrapolated up to this temperature. The resulting diameter expected, $d(7000\,\mathrm{K})$, was obtained via equation (4.3),

$$d(7000\,\mathrm{K}) = \sqrt{\left(\frac{d(7000\,\mathrm{K})}{d_0}\right)^2} \cdot d_0\,, \tag{4.3}$$

where $d_0 = 0.5\,\mathrm{mm}$ is the diameter at room temperature. Diffraction experiments for the resulting two diameters were conducted:

LP nitrogen experiment	$d(7000\,\mathrm{K}) = (0.579 \pm 0.013)\,\mathrm{mm}$
HP water experiment	$d(7000\,\mathrm{K}) = (0.65 \pm 0.03)\,\mathrm{mm}$

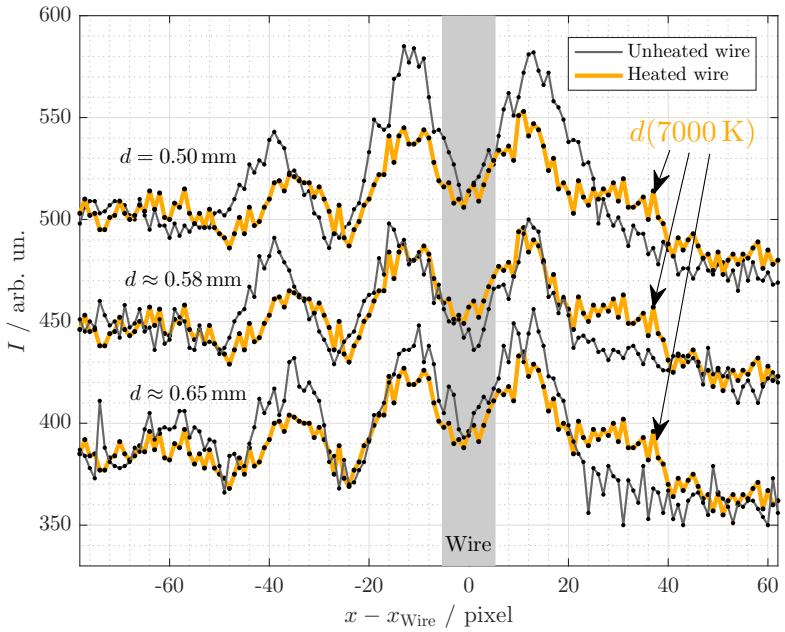

Figure 4.17.: Laser diffraction patterns of unheated wires (thin gray lines) with diameters that are expected from low-pressure nitrogen experiments ($d \approx 0.58\,\mathrm{mm}$) and from high-pressure water experiments ($d \approx 0.65\,\mathrm{mm}$) compared to the corresponding diffraction image under heating-conditions at the same temperature (thick line, $d(7000\,\mathrm{K})$). Intensity I is plotted as a function of relative pixel position $x - x_{\mathrm{Wire}}$. Data obtained at a pressure of 1 kbar.

Fig. 4.17 shows the result of this experiment. The thick colored line, indicted by $d(7000\,\mathrm{K})$ represents the diffraction pattern of a heated-wire at 7000 K as already depicted in Fig. 4.16 (b), image 4. The thin solid lines represent the diffraction image of the unheated wires with diameters that are predicted in the low-pressure and high-pressure experiments, as outlined above.

The unheated wire with 0.58 mm in diameter produces a diffraction image with peaks that are further apart (smaller obstacle) than those obtained at the same reference temperature under heating conditions. Therefore, the physical wire expansion alone can *not* explain the diffraction pattern observed under heating conditions. There must be an additional effect under heating conditions that makes the wire appear larger than it is.

Another interesting conclusion can be drawn: The unheated wire with 0.65 mm in diameter produces the same diffraction image as the heated-wire at the reference temperature - the diffraction method and expansion method thus yield the same results. This is a valuable indication of the consistency between the diffraction and the expansion method. Hence, the experiment further corroborates the above result, that the thermal expansion alone is not enough to explain the diffraction pattern under heating-conditions.

REFRACTION EXPERIMENTS For refraction experiments, the laser spot was positioned with a micrometer screw such that the light passes the wire in a distance of (1.5 ± 0.5) mm. Experiments were performed on both sides of the wire. The line profile of the laser spot was then calculated for each image slice captured during heating by summing over the pixel lines of the respective image. From each line profile, the centroid position, indicated by red circles, was calculated by numerical integration[10]. Fig. 4.18 show the resulting line profile time evolution for laser experiments on the left (a) and on the right side (b) of the wire (time propagates from top to bottom). A net refraction of the laser spot towards the wire is visible which was observed in three successive experiments. This proves that an index of refraction gradient is in fact evolving during pulse-heating. For the better of the liquid phase, the index of refraction is higher in the vicinity of the wire than at greater distances, thus leading to a refractive effect towards the optical axis (compare Fig. 4.13 (b)).

Fig. 4.18 (c) and (d) show the centroid position for successive image slices, corresponding to (a) and (b), relative to the first image in more detail. The shift reaches values of up to 3 pixel which corresponds to approximately 15 % of the line profile's FWHM. Taking a look at the thermogram for these experiments, depicted in Fig. 4.19, correlates the first strong deflection towards the wire (image no. 5) to the melting transition. At melting, the volume of the wire shows a discontinuous increase which may generate a shock wave. In fact, such melting shock waves were previously observed in pulse-heating experiments by G. Pottlacher [27]. The shockwaves, being longitudinal waves, travel at the speed of sound according to the pressure and temperature present. Assuming a temperature of 40 °C, the speed of sound at 1 kbar is $c = 1698\,\mathrm{m \cdot s^{-1}}$ [79]. Within 1 µs, the time between melt-

[10] GAUSS's area formula. A linear baseline was subtracted from the data before integration.

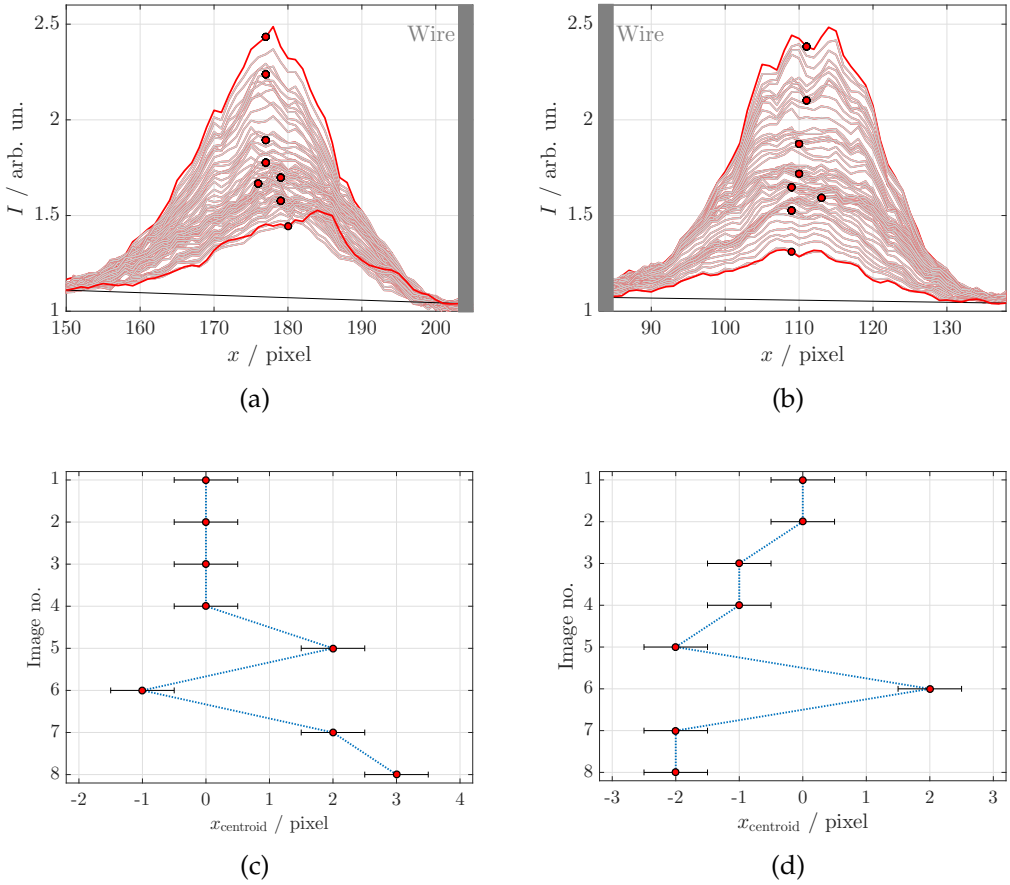

Figure 4.18.: Refraction of laser light passing a heated Nb wire from two sides at $p = 1\,\mathrm{kbar}$. (a) and (b) show the time evolution of the laserspot's line profile, intensity I as a function of pixel position x. Time propagates downwards. Red circles indicate the centroid position at a specific image. (c) and (d) show the above obtained centroid positions x_{centroid} relative to the position observed at the first image. A net refraction of the laser beam towards the wire can be observed.

ing onset and acquisition of image 5, the shockwave will have propagated approximately 1.7 mm which is in perfect agreement with the distance of the laser spot to the wire surface. Due to its longitudinal nature, a pressure minimum must follow the pressure maximum which might explain the opposed laserspot movement at image 6, shortly after the melting transition

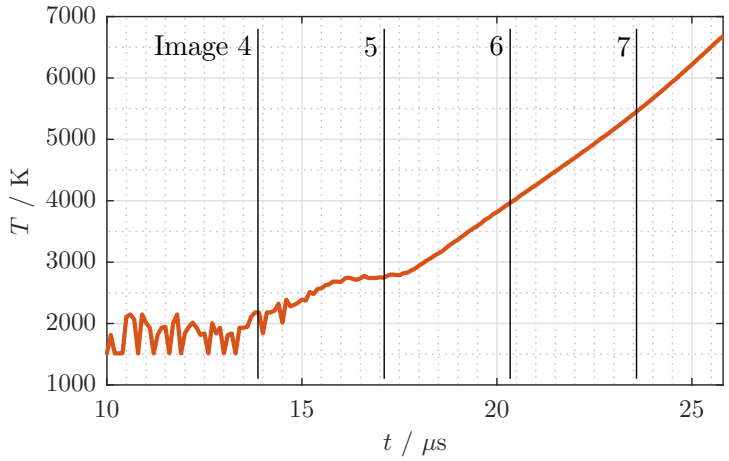

Figure 4.19.: Temperature T as a function of experimental duration t for Nb at the experimental conditions present in laser refraction experiments. Vertical lines mark the instants in time at which images are taken.

occurred.

If the laserspot is moved to a distance of (3.5 ± 1.0) mm to the wire, a refractive effect cannot be observed anymore. This indicates that the shock wave's energy is dissipated quickly - as a result, the misleading effect is confined to a potentially very small region surrounding the wire. This may also be the reason, why T. Hüpf did not observe a laser deflection in his experiments.

The laser refraction experiment was repeated for Ir, a metal that exhibited no signs of a thermal expansion discrepancy. The obtained evolution of the laser line profile and the relative centroid positions are depicted in Fig. 4.20. Consistent with the absence of a thermal expansion discrepancy, no laser deflection is observable for Ir in the liquid phase (apart from the melting shockwave). The deflection observed during melting is much stronger than for Nb. This may be related to the higher jump in volume ΔV during the melting transition (compare Fig. 4.7 and Fig. 4.1), where $\Delta V_{\mathrm{Ir}} \approx 8\,\%$ and $\Delta V_{\mathrm{Nb}} \approx 3\,\%$. It is a sheer speculation that this property might play a role in the explanation of the differently acting index of refraction for these two metals.

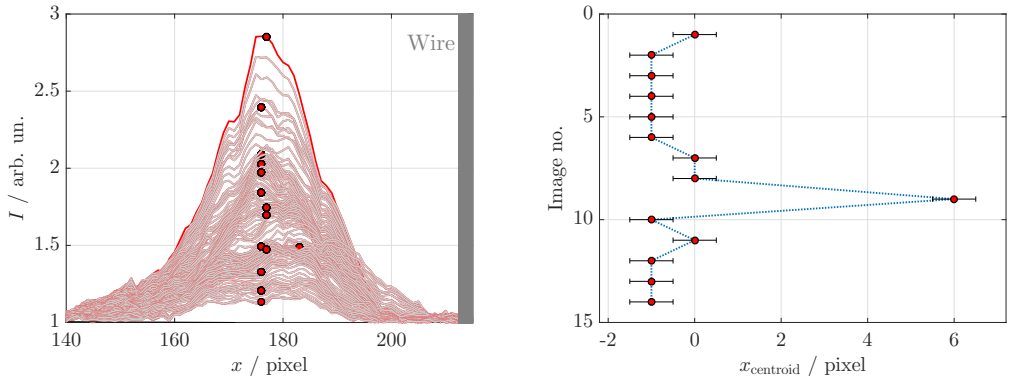

(a) (b)

Figure 4.20.: Refraction of laser light passing a heated Ir wire at $p = 1\,\mathrm{kbar}$. (a) shows the time evolution of the laserspot's line profile, intensity I as a function of pixel position x. Time propagates downwards. Red circles indicate the centroid position at a specific image. (b) shows the obtained centroid positions x_{centroid} relative to the position observed at the first image. Apart from image no. 9 (during melting transition) no net refraction of the laser beam towards the wire can be observed.

4.3.4. Conclusive remarks

It was proven in laser diffraction and laser refraction experiments, that light passing a heated Nb wire in a small distance is deflected (1 kbar, H_2O as medium). Due to the direction of this deflection, the most promising explanation for the observed thermal expansion discrepancy is a change in the index of refraction that originates from a dynamic pressure rise during the pulse-heating process in the vicinity of the wire.

The hypothesis that the observed deflection is responsible for the thermal expansion discrepancy is corroborated by the fact that this deflection is absent in an experiment on iridium, a metal that does not exhibit the discussed thermal expansion discrepancy.

The investigations conducted in this chapter show that it can be problematic for several metals, such as Nb and Ta, to measure the density with the high-pressure setup. Problems are:

- The potentially present influence of the sample material on the index of refraction of water,
- The significantly higher experimental effort due to the decoupled temperature and expansion measurement,
- A smaller wire resolution in the expansion measurement due to geometric constraints,
- Less background intensity for imaging due to the utilization of water as ambient medium.

Apart from the arising problems, the non-linear density regime (as a function of temperature) approaching the critical point could not be reached.

5. Results and Discussion

Summarized results for density as a function of temperature as well as critical point and phase diagram data are given in this chapter. Details on specimen wires used in this thesis are specified in Tab. 5.1. Liquid-phase density polynomials are stated in Tab. 5.2. Phase diagram and critical point data are summarized in Tab. 5.3 and Tab. 5.4. For detailed results and discussion of the metals Al, Ta, Nb and W, the reader is directly referred to the corresponding publication, appended at the end of this thesis.

Table 5.1.: Specifications of the wire specimens used in this thesis. The purity is specified in wt. %. "ann." abbreviates annealed, "as dr." abbreviates as drawn.

	Purity	Condition	Supplier	Catalog no.	ID no.
Al	99.999	Temper as dr.	Advent	AL501115	Gi2389
Ta	99.9	Temper ann.	Advent	TA550615	Gi1109
Nb	99.9	Temper ann.	Advent	NB537115	Gi1592
W	99.95	Clean	Goodfellow	W005160/18	LS73129JF
Ir	99.9	Temper ann.	Advent	IR524809	Gi2147
Re	99.99	Temper ann.	Advent	RE545909	Gi4101

5.1. Density as a function of temperature

Tab. 5.2 summarizes the density results obtained during this work. Data on aluminum are omitted here because they were measured by A. Schmon within the scope of his doctoral thesis [21]. Where possible, high-pressure

density data were combined with low-pressure density data to improve statistics and thus increase significance. This is the case for Ir and Re, metals which did not show a thermal expansion discrepancy. Regressions obtained from these combined data are indicated with a diamond symbol (◇). Furthermore, regressions derived from exclusive high-pressure (●) or low-pressure (○) data are given, if reasonable. High-pressure data for metals exhibiting a thermal expansion discrepancy, such as Ta and Nb, are omitted. Note that W was not investigated using the high-pressure setup, therefore, only low-pressure density data are given.

Table 5.2.: Fit-coefficients a and b for the liquid-phase density ρ as a function of temperature T in the form $\rho(T) = a - b \cdot T$. The temperature range of applicability is given. The relative density-uncertainty $U(\rho) \cdot \rho^{-1}$ at a fixed temperature T is given from the beginning of the liquid phase (first value) up to the highest temperature measured (second value), compare Sec. 6.1.3. All uncertainties are reported at a 95 % confidence level ($k = 2$).
○ . . . Derived from low-pressure (LP) data
● . . . Derived from high-pressure (HP) data
◇ . . . Derived from combined LP and HP data

	a	b	$U(\rho) \cdot \rho^{-1}$	Temperature range
	$10^3\,\mathrm{kg \cdot m^{-3}}$	$\mathrm{kg \cdot m^{-3} \cdot K^{-1}}$	1	K
○ Ta	17.25 ± 0.17	0.68 ± 0.04	0.014 to 0.023	$3280 \leq T \leq 6400$
○ Nb	8.52 ± 0.09	0.304 ± 0.019	0.013 to 0.022	$2745 \leq T \leq 5847$
○ W	19.8 ± 0.4	0.71 ± 0.08	0.028 to 0.038	$3687 \leq T \leq 5631$
○ Ir	22.38 ± 0.26	0.99 ± 0.07	0.016 to 0.025	$2719 \leq T \leq 4880$
● Ir	22.8 ± 0.5	1.16 ± 0.08	0.028 to 0.079	$2719 \leq T \leq 9160$
◇ Ir	22.96 ± 0.20	1.17 ± 0.05	0.012 to 0.049	$2719 \leq T \leq 9160$
● Re	20.9 ± 0.4	0.76 ± 0.06	0.025 to 0.073	$3485 \leq T \leq 11\,800$
◇ Re	21.0 ± 0.4	0.77 ± 0.05	0.021 to 0.065	$3485 \leq T \leq 11\,800$

Tantalum

The reader is referred to publication II appended at the and of this thesis [59]: *Density of Liquid Tantalum and Estimation of Critical Point Data*

Niobium

The reader is referred to publication III appended at the end of this thesis [80]: *Density of Liquid Niobium and Tungsten and the Estimation of Critical Point Data*

Tungsten

The reader is referred to publication III appended at the end of this thesis [80]: *Density of Liquid Niobium and Tungsten and the Estimation of Critical Point Data*

Iridium

Density as a function of temperature of iridium is depicted in Fig. 5.1. The plotted linear regression was calculated combining high-pressure and low-pressure data sets and considering their individual uncertainties. The corresponding fit coefficients are given in Tab. 5.2 ($\diamond$ Ir). Experimental data are tabulated in the Appendix (Tab. B.1 and B.2).

For temperature deduction, a normal spectral emissivity ε as function of radiance temperature T_r was adopted from Cagran and Pottlacher [71],

$$\varepsilon_\mathrm{Ir}(684.5\,\mathrm{nm}, T_\mathrm{r}) = 0.3293 + 7.988 \times 10^{-6} \cdot T_\mathrm{r}\ ,$$

valid in the range $2365\,\mathrm{K} < T_\mathrm{r} < 3650\,\mathrm{K}$. The normal spectral emissivity was assumed to continue linearly above a radiance temperature of 3650 K. A true melting temperature of $T_\mathrm{m} = 2719\,\mathrm{K}$ was adopted from [81]. To convert the measured volume expansion into density data, a room-temperature density of $\rho_0 = (22\,562 \pm 20)\,\mathrm{kg \cdot m^{-3}}$ was applied [77].

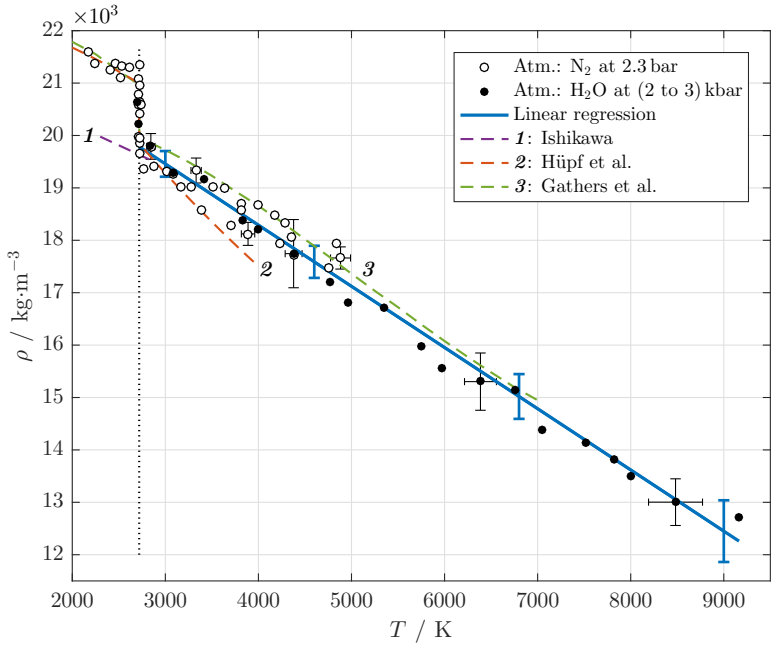

Figure 5.1.: Density ρ as a function of temperature T of iridium. The dotted vertical line marks the melting temperature. Symbols and solid line: This work's experimental data and corresponding linear regression of the combined data set. All uncertainties are given at a 95 % confidence level ($k = 2$). Dashed lines represent data reported in the literature: Ishikawa (priv. comm. 2019), Hüpf et al. [82], Gathers et al. [15].

The obtained density as a function of temperature exhibits a very good consistence with the literature at the end of the solid phase and at the beginning of the liquid phase, where a density of $\rho(T_{\mathrm{m,l}}) = (19.78 \pm 0.24) \times 10^3\,\mathrm{kg \cdot m^{-3}}$ ensues from the combined linear regression[1]. This value is in excellent agreement to all three literature sources, residing within the stated $k = 2$ uncertainty interval.

Ishikawa[2] reports a density value at the liquidus point that is 0.74 % lower than this work's value. The decrease in density with temperature reported by Ishikawa is slightly less pronounced than in this work but in very good

[1] Subscript "l" in $T_{\mathrm{m,l}}$ indicates the liquid phase.
[2] Private communication via email: T. Ishikawa, 2019.

agreement. The author used a levitation method, undercooling a liquid metal droplet in vacuum. Owing to the undercooling, density data at temperatures below the melting temperature are to be understood as an extension of the liquid phase.

Previous data reported by our group[3] (Hüpf et al. [82]) are in excellent agreement at the beginning of the liquid phase, being 0.35 % higher than this work's data. However, the extraordinary strong decrease of liquid-phase density with temperature reported could not be reproduced. Data reported by Hüpf et al. were acquired with the low-pressure setup in inert gas atmosphere.

Gathers et al. [15] report a value at the beginning of the liquid phase that is 0.92 % higher than this work's value. The consistence in both solid and liquid phase is remarkable and resides within or very close to the 95 % uncertainty interval throughout the whole reported data range. These data were acquired with a pulse-heating technique at a pressure of 0.3 GPa in inert gas atmosphere. This result is particularly interesting as it once more reinforces that typical pressures applied in high-pressure pulse-heating experiments only have a negligible impact on density measurements.

High-pressure experiments on Ir allowed to extend the accessible temperature range by more than 4000 K compared to low-pressure experiments. The reported data reach more than 2000 K further into the liquid phase than previously reported literature data do. Even though the temperature range was greatly increased, a non-linear behavior of density as a function of temperature could still not be be resolved.

Rhenium

Density as a function of temperature of rhenium is depicted in Fig. 5.2. The given linear regression was calculated combining low-pressure and high-pressure data sets and considering their individual uncertainties. The corresponding fit coefficients are given in Tab. 5.2 (◇ Re). Experimental data are tabulated in the Appendix (Tab. B.3 and B.4).

[3]Published thermal expansion data were converted into density data with the above stated room-temperature density.

For temperature deduction, a normal spectral emissivity ε as function of radiance temperature T_r was adopted from Cagran et al. [83],

$$\varepsilon_{Re}(684.5\,nm, T_r) = 0.3130 - 8.5186 \times 10^{-6} \cdot T_r \ ,$$

valid in the range $2870\,K < T_r < 4100\,K$. The stated emissivity polynomial was assumed to be valid also at radiance temperatures beyond 4100 K. A melting temperature of $T_m = 3458\,K$ was adopted from [75] for temperature calibration. To derive density data from the measured thermal expansion data, a room-temperature density of $\rho_0 = (21\,020 \pm 20)\,kg \cdot m^{-3}$ was applied [76].

Only a few valid data points in the liquid phase could be obtained with the low-pressure setup because of evolving inhomogeneities in sample diameter.

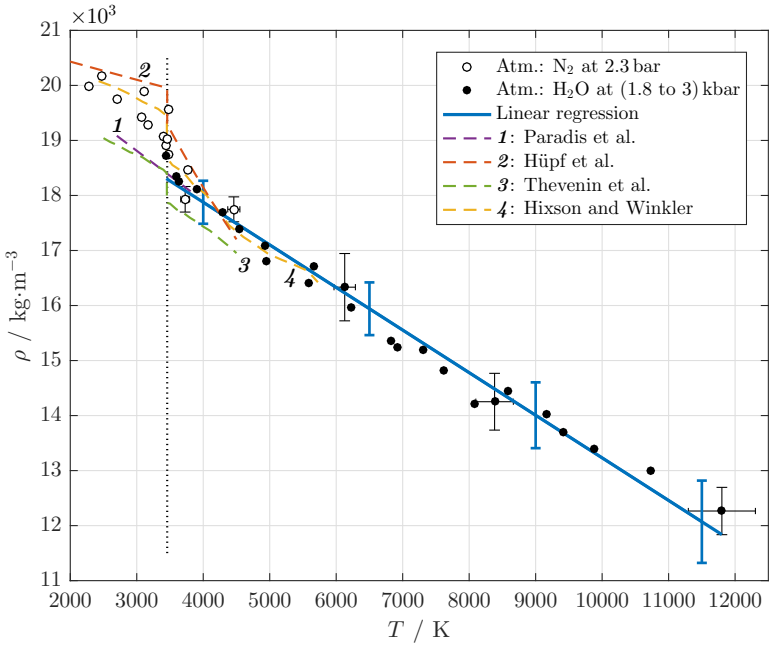

Figure 5.2.: Density ρ as a function of temperature T of rhenium. The dotted vertical line marks the melting temperature. Symbols and solid line: This work's experimental data and corresponding linear regression of the combined data set. All uncertainties are given at a 95 % confidence level ($k = 2$). Dashed lines represent data reported in the literature: Paradis et al. [6], Hüpf et al. [72], Thévenin et al. [20], Hixson and Winkler [19].

These inhomogeneities, leading to an apparent increased expansion, render an evaluation impossible. Fortunately, this problem could be suppressed by increasing the static pressure acting on the sample's surface (high-pressure experiments).

At the beginning of the liquid phase, the combined data evaluation yields a density of $\rho(T_{m,l}) = (18.3 \pm 0.4) \times 10^3\,\mathrm{kg \cdot m^{-3}}$.

This value is in excellent agreement with that reported by Paradis et al. [6], being only 0.34 % higher than this work's value. The concordance of the slope of liquid density as a function of temperature with this work's data is in extraordinary agreement. Data reported by Paradis et al. were acquired by investigating a levitated liquid metal droplet at a pressure of 10^{-5} Pa in a super-cooled state. Data reported below the melting temperature are thus an extension of the liquid phase density to lower temperatures.

Data reported previously by our group[4] (Hüpf et al. [72]) show a deviation in density already at the end of the solid phase. At the beginning of the liquid phase, the Hüpf value is 5.2 % higher than this work's data suggests, thus outside the uncertainty boundaries. Especially the decrease in density with temperature reported in these previous data is questionably strong and inconsistent with this work's data as well as other data reported in the literature. The data were acquired with the low-pressure setup in inert gas atmosphere. Given the arising problems observed when using this very same setup suggests that evolving inhomogeneities in sample diameter may be the reason for the strong density gradient reported by Hüpf et al.

Density data reported by Thévenin et al. [20] are inconsistent at the end of the solid phase. These density data are as low as other authors report at the beginning of the liquid phase. In the liquid phase, the slope of density as a function of temperature is highly consistent with this work's data and most of the literature data. The value at the beginning of the liquid phase is 2.6 % lower than this work's value and thus just outside the 95 % confidence interval. These data were acquired with a pulse-heating setup at a pressure of 0.12 GPa in an argon gas atmosphere.

[4] Published thermal expansion data were converted into density data with the above stated room-temperature density.

Density data reported by Hixson and Winkler [19] are in very good agreement both at the end of the solid and at the beginning of the liquid phase. At the beginning of the liquid phase, the reported value is 1.9 % higher than this work's data suggest. Hixson et al. used a high-pressure pulse-heating system operating at 0.2 GPa in an inert gas atmosphere.

Performing high-pressure experiments on Re allowed to greatly extend the temperature range up to almost 12 000 K, surpassing the highest temperature accessed in this work's low-pressure experiments by more than 7000 K. No non-linearity of the density as a function of temperature could be observed in the accessed temperature range.

5.2. Critical point data and phase diagrams

The phase diagram and critical point of the metals were estimated by density extrapolation according to the algorithm published by Schröer and Pottlacher [24]. Summarized phase diagram and critical point data are given in Tab. 5.3 and Tab. 5.4.

Table 5.3.: Estimated phase diagram parameters of the investigated high-melting metals according to equations (2.22) and (2.21). Temperature range of validity from melting temperature T_m up to the critical temperature T_c of the respective metal. a, c, b and b_2 are the obtained fitting coefficients, ρ_c is the critical density.
○ . . . Derived from low-pressure (LP) density regression
◇ . . . Derived from combined LP and HP density regression

	ρ_c $\mathrm{kg \cdot m^{-3}}$	T_c K	a $10^{-5}\,\mathrm{K^{-1}}$	c $10^{-3}\,\mathrm{K^{-2/3}}$	b $\mathrm{kg \cdot m^{-3} \cdot K^{-1/3}}$	b_2 $10^{-4}\,\mathrm{K^{-2/3}}$
○ Ta	3322	13 389	5.16	1.57	298	3.48
○ Nb	1722	14 231	4.42	1.42	147	3.13
○ W	3945	14 357	4.50	1.43	338	3.16
◇ Ir	3636	12 015	8.28	2.13	379	5.11
◇ Re	3472	16 248	5.66	1.66	319	3.91

Table 5.4.: Summarized values and corresponding uncertainties for critical temperature T_c and critical density ρ_c of the investigated high-melting metals. Stated uncertainties represent the possible change due to the uncertain density fit coefficients.
○ . . . Derived from low-pressure (LP) density regression
◇ . . . Derived from combined LP and HP density regression

	T_c $10^3\,\mathrm{K}$	ρ_c $10^3\,\mathrm{kg\cdot m^{-3}}$
○ Ta	13.4 ± 0.7	3.32 ± 0.09
○ Nb	14.2 ± 0.9	1.72 ± 0.05
○ W	14.4 ± 1.6	3.95 ± 0.19
◇ Ir	12.0 ± 0.4	3.64 ± 0.15
◇ Re	16.3 ± 0.9	3.47 ± 0.22

Tantalum

The reader is referred to publication II appended at the and of this thesis [59]: *Density of Liquid Tantalum and Estimation of Critical Point Data*

Niobium

The reader is referred to publication III appended at the end of this thesis [80]: *Density of Liquid Niobium and Tungsten and the Estimation of Critical Point Data*

Tungsten

The reader is referred to publication III appended at the end of this thesis [80]: *Density of Liquid Niobium and Tungsten and the Estimation of Critical Point Data*

Iridium

Fig. 5.3 depicts the estimated phase diagram of iridium and its corresponding critical point. For the critical temperature T_c and the critical density ρ_c one obtains

$$T_c = (12.0 \pm 0.4) \times 10^3\,\mathrm{K}\,,$$
$$\rho_c = (3.64 \pm 0.15) \times 10^3\,\mathrm{kg \cdot m^{-3}}\,.$$

When available in the literature, (T_c, ρ_c)-pairs were plotted along with this work's data in Fig. 5.3. It can be observed that this work's critical density is lower than those reported in the literature, while the critical temperature resides at an intermediate position compared to the three literature sources considered.

The value reported by Hess and Schneidenbach [39], using the Likalter relation together with a vapor pressure curve, resides at a density of $\rho_c = 10.0 \times 10^3\,\mathrm{kg \cdot m^{-3}}$ which is very close to the value observed at the highest temperatures experimentally accessed. The reported value thus appears to be rather high for the critical density. However, the critical temperature $T_c = 10\,636\,\mathrm{K}$ is in good concordance with this work's prediction.

Data reported by Gathers et al. [15] using the soft sphere van der Waals model ($\rho_c = 5.6369 \times 10^3\,\mathrm{kg \cdot m^{-3}}$, $T_c = 10\,335\,\mathrm{K}$) show a satisfactory agreement with this work's critical point, although the data appear to show higher consistency with this work's simplified Ising phase diagram.

The critical point reported by Fortov et al. [84], $\rho_c = 6.77 \times 10^3\,\mathrm{kg \cdot m^{-3}}$, resides at a density value that is incompatible with this work's experimentally obtained liquid phase density. Even when extrapolating this work's density data linearly, Fortov's critical point can not be reached. The reported critical temperature of $T_c = 15\,380\,\mathrm{K}$ appears rather high as well (Grosse method).

Further critical temperatures reported in the literature range between values as low as $T_c = 9723\,\mathrm{K}$ (Hess and Schneidenbach [39], Guldberg rule) to values as high as $T_c = (17\,760 \pm 790)\,\mathrm{K}$ (Lang [31], Kopp-Lang rule). Very good consistence is also achieved with a recently reported value by Blairs

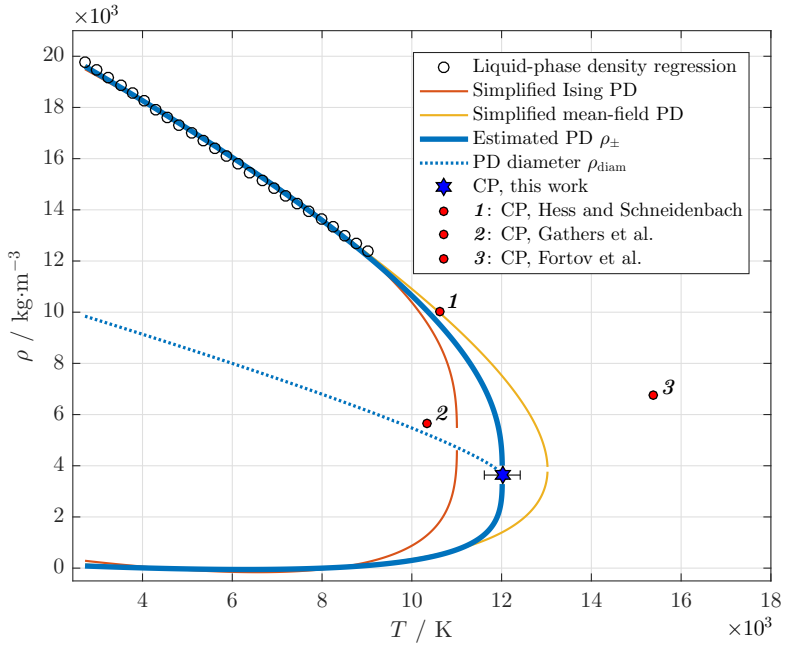

Figure 5.3.: Density ρ as a function of temperature T of iridium up to the critical point (CP). Open circles represent data points generated from the density regression. Thin solid lines show the estimated phase diagram (PD) according to a simplified Ising and mean-field behavior. The best estimate for the phase diagram $\rho_{\pm}$ is indicated by a thick solid line, terminating in the critical point (star). The corresponding phase diagram diameter ρ_{diam} is plotted as dotted line. Critical points reported in the literature are indicated by red dots: Hess and Schneidenbach [39], Gathers et al. [15], Fortov et al. [84].

and Abbasi [34], $T_c = 11\,498\,\text{K}$ (Guldberg rule) and with a prediction reported by Hess and Schneidenbach [39], $T_c = 12\,009\,\text{K}$ (Goldstein scaling proposal).

A critical pressure of $p_c = 0.950\,13\,\text{GPa}$ [15] up to $p_c = 1.55\,\text{GPa}$ [39] is reported in the literature.

The influence of temperature range accessed in density measurements on the estimated critical point was investigated for Ir, depicted in Fig. 5.4. The extrapolation algorithm was repeated for density fits ranging from the melting temperature to the highest temperature reached in low-pressure

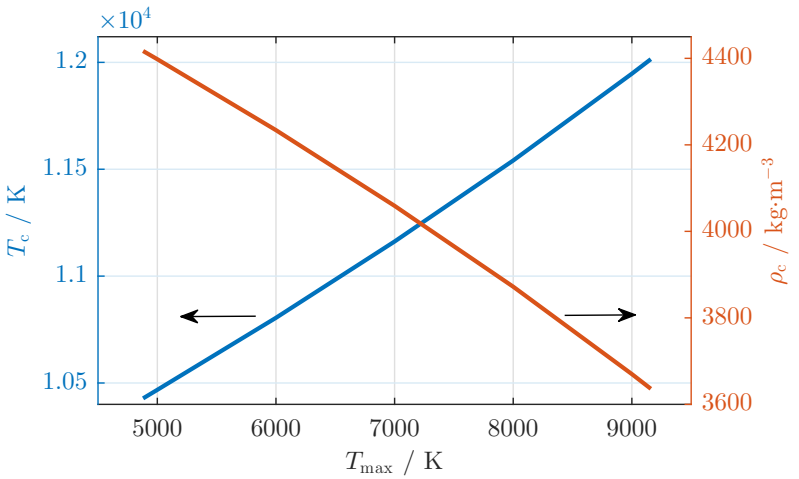

Figure 5.4.: Estimated critical temperature T_c and critical density ρ_c of Ir as a function of input data's temperature range, ranging from the melting temperature up to T_{max}. The algorithm provides a lower limit for the critical temperature and an upper limit for the critical density.

experiments ($T_{max} \approx 5000\,K$) and from the melting point to the highest temperature reached in high-pressure experiments ($T_{max} \approx 9000\,K$). The fit equation used for the analysis was kept constant applying the coefficients derived from the combined data evaluation ($\diamond$ Ir, Tab. 5.2). In the considered temperature range, the estimated critical temperature increases by $\Delta T_c/\Delta T_{max} \approx 0.37\,K \cdot K^{-1}$ while the critical density decreases by $\Delta\rho_c/\Delta T_{max} \approx 0.18\,kg \cdot m^{-3} \cdot K^{-1}$ with increasing T_{max}. Over the whole considered temperature range, the critical temperature thus increases by 15 %, the critical density decreases by 18 %. Therefore, the algorithm used generally provides a lower limit for the estimated critical temperature, and an upper limit for the estimated critical density.

Rhenium

Fig. 5.5 shows the critical point and estimated phase diagram of rhenium. For the critical temperature T_c and the critical density ρ_c one obtains by

extrapolation

$$T_c = (16.3 \pm 0.9) \times 10^3\,\mathrm{K}\,,$$
$$\rho_c = (3.47 \pm 0.22) \times 10^3\,\mathrm{kg \cdot m^{-3}}\,.$$

The obtained critical point exhibits the lowest critical density among previously reported values. The value reported by Young and Alder applying the hard-sphere van der Waals model [44], $\rho_c = 5.37 \times 10^3\,\mathrm{kg \cdot m^{-3}}$, is in satisfactory consistence with the simplified mean-field phase diagram, but it is considerably higher than this work's value. However, the reported critical temperature $T_c = 17\,293\,\mathrm{K}$ is in good agreement with our value.

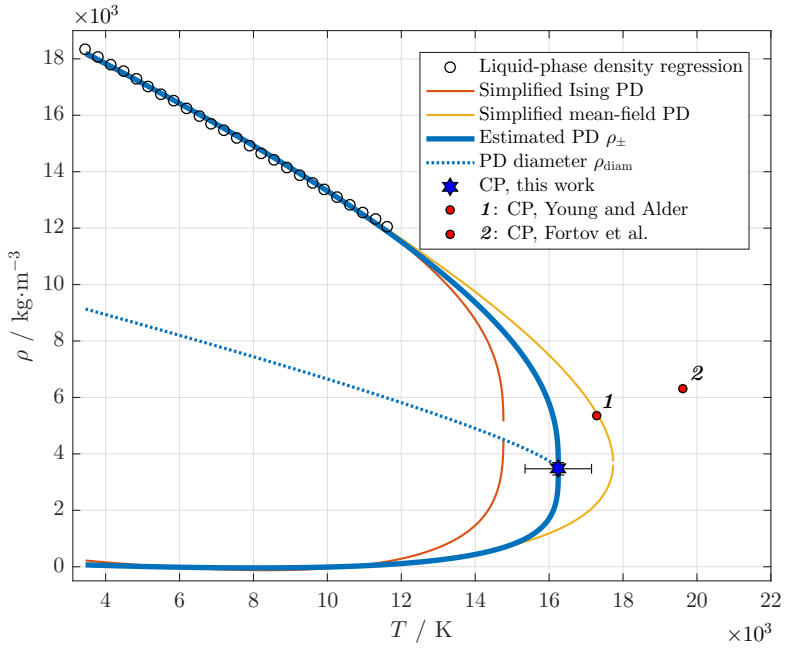

Figure 5.5.: Density ρ as a function of temperature T of rhenium up to the critical point (CP). Open circles represent data points generated from the density regression. Thin solid lines show the estimated phase diagram (PD) according to a simplified Ising and mean-field behavior. The best estimate for the phase diagram $\rho_\pm$ is indicated by a thick solid line, terminating in the critical point (star). The corresponding phase diagram diameter ρ_{diam} is plotted as dotted line. Critical points reported in the literature are indicated by red dots: Young and Alder [44], Fortov et al. [84].

Fortov et al. report a critical density of $\rho_c = 6.32 \times 10^3\,\mathrm{kg \cdot m^{-3}}$ and a critical temperature of $T_c = 19\,600\,\mathrm{K}$ [84] (Grosse method). This extraordinary high critical temperature could only be reached, if our experimental data were extrapolated linearly up to this very high temperature.

Further critical temperature values reported in the literature range from $T_c = 12\,138\,\mathrm{K}$ (Hess and Schneidenbach [39], Guldberg rule) to $T_c = (20\,660 \pm 540)\,\mathrm{K}$ (Lang [31], Kopp-Lang rule), where values reported earlier tend to be higher than more recent values. This is also the case for a critical temperature reported in 1961 by Grosse, $T_c = 20\,500\,\mathrm{K}$ [35] (Grosse method). More recent values given by Blairs and Abbasi [34] indicate that the critical temperature is lower than that: $T_c = 14\,608\,\mathrm{K}$ (modified Gates-Thodos rule) and $T_c = 13\,398\,\mathrm{K}$ (relation to surface tension).

For the critical pressure of rhenium, values of $p_c = 0.157\,\mathrm{GPa}$ [84] and $p_c = 0.148\,77\,\mathrm{GPa}$ [44] are stated in the literature.

6. Uncertainty Estimation

This chapter focuses on the uncertainty analysis of density and critical point data as these quantities are mainly addressed in this thesis. For uncertainty estimation of properties such as enthalpy or electrical resistivity as a function of temperature, the reader is referred to the doctoral thesis of B. Wilthan [85].

6.1. Density uncertainty

The uncertainty estimation of density data measured by means of ohmic-pulse heating faces some difficulties when conducted according to the *guide to the expression of uncertainty in measurement* (GUM) [86].

The GUM principle can only be easily applied if there is a functional relation between the measurand Y and all N input quantities X_i:

$$Y = f(X_1, X_2, ..., X_N)\,. \tag{6.1}$$

In such a case, the combined[1] standard uncertainty $u_c(y)$, where y and x_i are estimates of Y and X_i, is given by

$$u_c^2(y) = \sum_{i=1}^{N} \underbrace{\left(\frac{\partial f}{\partial x_i}\right)^2}_{c_{x_i}^2} u^2(x_i)\,. \tag{6.2}$$

Here, c_{x_i} are the so-called sensitivity coefficients, describing how f changes with a small change in x_i, and $u(x_i)$ is the standard uncertainty of the i-th

[1] Subscript "c".

component of x. In case of density $\rho(T)$ obtained by ohmic pulse-heating, we can define a functional relation according to

$$\rho(T) = \rho_0 \cdot \left(\frac{d_0}{d_T}\right)^2 , \tag{6.3}$$

where ρ_0 is the density at room temperature (literature value), and d_0 and d_T are the diameters at room temperature and at a specific temperature T recorded throughout an experiment.

As the temperature dependence is only given implicitly in d_T, the analysis is divided into three parts:

1. The uncertainty of each data point in x- and y-direction is calculated according to the respective functional relation of temperature and density.
2. A regression for the density behavior is calculated and the least-squares formula is used to obtain the uncertainties of the slope b and the intercept a according to the GUM. By this means, the individual uncertainties of the data points are included in the uncertainties of the regression coefficients.
3. The linear fit equation is treated according to the GUM together with the uncertainties of slope b, intercept a and temperature T to obtain a fit uncertainty in y. Uncertainties in x are thus converted into uncertainties in y.

All uncertainties are considered to be uncorrelated, yielding a worst-case estimate for the uncertainty.

6.1.1. Step 1 - uncertainty of data points

In this first step, the uncertainties of the single data points are calculated from their functional relations.

Uncertainty in x: Temperature

The temperature uncertainty is obtained with the MATLAB program *MAPHS* written by T. Macher [54]. It is based on the doctoral thesis of B. Wilthan [85] and directly calculates the expanded uncertainty of the temperature $U(T)$,

$$U(T) = k \cdot u_c(T)\,, \tag{6.4}$$

with the coverage factor $k = 2$ (95 % confidence).

Considered influencing parameters are the effective wavelength, the skin effect, alignment of the pyrometer, the temperature dependence of the calibration constant, the resolution of the transient recorder card and the uncertainty of the literature value for the melting temperature.

Uncertainty in y: Density

According to equation (6.2), the combined uncertainty $u_c(\rho)$ of the data points in y-direction can be estimated by

$$u_c^2(\rho) = \left(\frac{\partial\rho}{\partial d_0}\right)^2 u^2(d_0) + \left(\frac{\partial\rho}{\partial d_T}\right)^2 u^2(d_T) + \left(\frac{\partial\rho}{\partial\rho_0}\right)^2 u^2(\rho_0)\,, \tag{6.5}$$

with the standard uncertainties of the evaluated diameters $u(d_0)$ and $u(d_T)$, and the standard uncertainty of the room-temperature density $u(\rho_0)$. Note that an uncertainty in ρ_0 would result in a systematic shift of all data to higher or lower values, but would not change the (statistical) uncertainty of an individual data point. This systematic contribution will thus be neglected as far as the uncertainty of the individual data points are concerned. It will however later contribute to the total uncertainty.
The values for $u(d_0)$ and $u(d_T)$ can be estimated by evaluating the same diameter several times and calculating the standard deviation of the mean value. The procedure was repeated for all image slices. The maximum of the so-obtained standard deviations was doubled to account for possible systematic effects and taken as uncertainty, independent of temperature:

$$u(d_0) = \begin{cases} 0.16\,\text{pixel} & \text{low-pressure experiments} \\ 0.46\,\text{pixel} & \text{high-pressure experiments} \end{cases}$$
$$u(d_T) = \begin{cases} 0.30\,\text{pixel} & \text{low-pressure experiments} \\ 0.54\,\text{pixel} & \text{high-pressure experiments.} \end{cases}$$

From equation (6.5) and with the functional relation defined in equation (6.3) we obtain the two sensitivity coefficients

$$c_{d_0} = \rho_0 \cdot \frac{2d_0}{d_T^2}, \qquad c_{d_T} = -\rho_0 \cdot \frac{2d_0^2}{d_T^3}\,. \tag{6.6}$$

6.1.2. Step 2 - uncertainty of fit coefficients

Now we need to obtain the uncertainty of the slope b and the intercept a of our linear regression. For this we use the relations derived by Matus [87] that allow to include the uncertainties of the individual data points $(x_i, y_i) \mathrel{\widehat{=}} (T_i, \rho_i)$ into the uncertainties of the two fit coefficients a and b.

We take the usual definition for the mean values $\bar{x}$ and $\bar{y}$,

$$\bar{x} = \frac{1}{n}\sum_{i=1}^{n} x_i, \qquad \bar{y} = \frac{1}{n}\sum_{i=1}^{n} y_i\,, \tag{6.7}$$

where n is the number of data points. In addition we define

$$S_{xx} \equiv \sum_{i=1}^{n}(x_i - \bar{x})^2\,, \qquad S_{xy} \equiv \sum_{i=1}^{n}(x_i - \bar{x})(y_i - \bar{y})\,. \tag{6.8}$$

In the typical linear regression in y, the slope b and intercept a are then given by

$$b = \frac{S_{xy}}{S_{xx}}, \qquad a = \bar{y} - b\bar{x}\,. \tag{6.9}$$

Note that both equations in (6.9) are given as $f(x_1, ..., x_n, y_1, ..., y_n)$. Therefore, equation (6.2) can be applied to calculate the combined uncertainties according to the GUM.

Uncertainty of the slope b

The combined uncertainty of the slope b is given by

$$u_c^2(b) = \sum_{i=1}^{n} \left(\frac{\partial b}{\partial x_i} \right)^2 u^2(x_i) + \sum_{i=1}^{n} \left(\frac{\partial b}{\partial y_i} \right)^2 u^2(y_i) \,. \tag{6.10}$$

The sensitivity coefficients in this case are

$$c_{x_i,b} = \frac{(y_i - \bar{y}) - 2b(x_i - \bar{x})}{S_{xx}}, \qquad c_{y_i,b} = \frac{(x_i - \bar{x})}{S_{xx}} \,. \tag{6.11}$$

Uncertainty of the intercept a

The same procedure is now conducted for the intercept a:

$$u_c^2(a) = \sum_{i=1}^{n} \left(\frac{\partial a}{\partial x_i} \right)^2 u^2(x_i) + \sum_{i=1}^{n} \left(\frac{\partial a}{\partial y_i} \right)^2 u^2(y_i) + u^2(\rho_0) \,, \tag{6.12}$$

with the sensitivity coefficients

$$c_{x_i,a} = \frac{S_{xy} + n\bar{x}(y_i - \bar{y}) - 2bn\bar{x}(x_i - \bar{x})}{nS_{xx}} \,, \qquad c_{y_i,a} = \frac{S_{xx} - n\bar{x}(x_i - \bar{x})}{nS_{xx}} \,. \tag{6.13}$$

Note that the last term in equation (6.12) accounts for the uncertainty in density due to the uncertainty of the literature value ρ_0 which was neglected in Step 1.

6.1.3. Step 3 - uncertainty of fit equation

In this last step, we want to calculate the uncertainty of the fit ρ_{fit} at a given temperature T.

In a general form, the fit is given by the equation

$$\rho_{\text{fit}}(T) = a + b \cdot T \,. \tag{6.14}$$

Therefore, we can again apply the GUM method and transform the temperature uncertainty into a density uncertainty. For better readability, the temperature dependent density obtained via the fit $\rho_{\text{fit}}(T)$ is now referred to as ρ_{fit}.

$$u_{\text{c}}^2(\rho_{\text{fit}}) = \left(\frac{\partial \rho_{\text{fit}}}{\partial a}\right)^2 u^2(a) + \left(\frac{\partial \rho_{\text{fit}}}{\partial b}\right)^2 u^2(b) + \left(\frac{\partial \rho_{\text{fit}}}{\partial T}\right)^2 u^2(T)\,, \tag{6.15}$$

where the sensitivity coefficients are now given as

$$c_{a,\rho_{\text{fit}}} = 1\,, \qquad c_{b,\rho_{\text{fit}}} = T\,, \qquad c_{T,\rho_{\text{fit}}} = b\,. \tag{6.16}$$

The expanded uncertainty is then calculated as

$$U(\rho_{\text{fit}}) = k \cdot \sqrt{u_{\text{c}}^2(\rho_{\text{fit}})}\,, \tag{6.17}$$

with $k = 2$ (95 % confidence).

6.1.4. Uncertainty budget

We start with equation (6.15) to calculate the relative contributions of the four quantities d_0, d_T, T and ρ_0 on the fit uncertainty. We replace $u_{\text{c}}^2(b)$ and $u_{\text{c}}^2(a)$ by equations (6.10) and (6.12) and write out the variance $u^2(y_i)$ according to equation (6.5).

Rewriting equation (6.15) and sorting the terms then yields

$$\begin{aligned} u_{\text{c}}^2\left(\rho_{\text{fit}}(x_i)\right) = & \underbrace{x_i^2 \sum_{i=1}^{n} c_{x_i,b}^2 u_{x_i}^2 + b^2 u_{x_i}^2 + \sum_{i=1}^{n} c_{x_i,a}^2 u_{x_i}^2}_{u^2(T)} \\ & + \underbrace{x_i^2 \sum_{i=1}^{n} c_{y_i,b}^2 (c_{d_0}^2 u_{d_0}^2) + \sum_{i=1}^{n} c_{y_i,a}^2 (c_{d_0}^2 u_{d_0}^2)}_{u^2(d_0)} \\ & + \underbrace{x_i^2 \sum_{i=1}^{n} c_{y_i,b}^2 (c_{d_T}^2 u_{d_T}^2) + \sum_{i=1}^{n} c_{y_i,a}^2 (c_{d_T}^2 u_{d_T}^2)}_{u^2(d_T)} \\ & + u^2(\rho_0)\,, \end{aligned} \tag{6.18}$$

where the sensitivity coefficients as given in equation (6.16) were already applied because of their simple nature. The relative contribution at the value $x_i \equiv T_i$ of one of the four quantities d_0, d_T, T, ρ_0 (abbreviated as $\cdots$), referred to as *Index* in GUM-language, is then simply computed by

$$Index(\cdots) = \frac{u^2(\cdots)}{u_c^2\left(\rho_{\text{fit}}(x_i)\right)}\,, \tag{6.19}$$

and can be plotted as a function of T.

6.2. Critical point uncertainty

The uncertainty of the critical point is estimated by monitoring the effect of changed algorithm input quantities, i.e., intercept a and slope b of the density regression, on the resulting critical point. The algorithm was conducted three times, for pairs of intercept and slope[2] that are changed in a worst-case fashion according to their uncertainties:

1. (a, b): Normal density behavior,
2. $(a + u(a), b + u(b))$: High and flat density behavior,
3. $(a - u(a), b - u(b))$: Low and steep density behavior.

Here, $u(x)$ denotes the $k = 1$ uncertainty of x, derived above.

The doubled standard deviation for critical temperature and density, resulting from the three evaluations is then given as a measure for the uncertainty of the critical point. Note that this uncertainty is only a measure of how the critical point can change due to the uncertain fit coefficients, but cannot account for a possibly inappropriate model.

[2] Recall $\rho_{\text{fit}}(T) = a + b \cdot T\,, \quad b < 0.$

7. Conclusion and Outlook

The liquid-phase density of niobium, tantalum, tungsten, iridium and rhenium was experimentally determined by means of low-pressure and high-pressure ohmic pulse-heating. As proposed by A. Schmon, exclusive density measurements were conducted.
An extraordinary good consistence can be observed between the newly obtained data and the very precise data reported by the JAXA group (Paradis et al.). This is particularly true for the density at the beginning of the liquid phase that deviates by less than 1 % from the JAXA data in all cases except for tungsten. However, also in the case of tungsten, the data reported by Paradis et al. are within the stated uncertainty interval. The very steep decrease of the density versus temperature in the liquid phase, that was previously reported by our work group for most of the investigated metals, could not be reproduced. The strong decrease in density with temperature in these previous studies might be related to the simultaneous measurement of density and electrical data, using voltage knives that exert lateral forces onto the wire, as indicated by A. Schmon.

On the road to further push the upper temperature limit and even resolve the non-linear density regime, the high-pressure pulse-heating setup was reestablished. As previously reported by Hüpf, a discrepant behavior between density data obtained in nitrogen at low pressure and density derived in high-pressure experiments in water atmosphere could be confirmed. Interestingly, the described discrepancy, leading to an apparent enlarged thermal expansion in high-pressure experiments, does not occur for all investigated metals. Investigations indicate that the observed effect can be correlated to a dynamic change in the index of refraction during pulse-heating. However, the reason why this dynamic change does not occur for all elements remains to be unveiled and stimulates further research.

The original aim of directly measuring density data points in the non-linear region of the phase diagram, and thus positively affect the extrapolative estimate of critical point data, could not be achieved by means of high-pressure ohmic pulse-heating. The critical point and the phase diagram of the investigated metals were thus obtained from the derived linear density regressions, applying the Schröer-Pottlacher algorithm. For the investigated metals, this algorithm yields values for the critical temperature that are located in the lower middle range compared to the estimates reported in the literature. A trend of decreasing critical temperature predictions over the years can be observed.
The critical density derived by means of the Schröer-Pottlacher approach was found to be rather low compared to estimates reported in the literature. This may partially be correlated to the frequent application of the rectilinear diameter rule in the literature.
In general, the Schröer-Pottlacher algorithm yields satisfactory results but is strongly dependent on the temperature range of the input data. As long as no non-linearity in the density-temperature behavior is observed, i.e., as long as the obtained density shows a linear decrease with temperature, the algorithm provides a lower limit for the critical temperature, and an upper limit for the critical density. In other words, a density regression reaching to higher temperatures will result in a higher critical temperature and a lower critical density estimate.
The influence of the uncertainty of the density fit coefficients on the resulting critical point was investigated. For the metals studied in this thesis, estimates of the critical density may vary between approximately 3 % to 6 % and estimates of the critical temperature by roughly 4 % to 11 % due to the uncertain fit coefficients.

Future high-pressure experiments would strongly benefit from a combined temperature and thermal expansion measurements. In that context, acquiring a tailored dichroic beam splitter, that reflects (close to) 100 % of the light at the pyrometer's narrow wavelength range, while transmitting (close to) 100 % in the remaining spectral region, would be a possibility. Together with an appropriate notch filter placed after the flash, the problem of decoupled temperature and expansion measurement could be solved.
Another improvement may be the application of a high intensity laser as background illumination instead of the commercial photoflash. An addi-

tional advantage of a laser would be its monochromatic wavelength, that could be chosen in a suitable spectral distance to the pyrometer's measuring wavelength. Also a great improvement for the expansion measurement would be the acquisition of a modern high-speed camera exhibiting a better image- and time resolution.
To tackle the problem of a changing refractive index in high-pressure experiments, two measures are imaginable. First, a medium may be used that exhibits a lower sensitivity of the index of refraction at the wavelength used for backlighting. Second, the wavelength of the background illumination may be changed to a regime, where the index of refraction is insensitive to pressure or temperature changes. In that context, an X-ray imaging system may be an interesting possibility.

8. Publications

I M. Leitner, T. Leitner, A. Schmon, K. Aziz and G. Pottlacher. "Thermophysical Properties of Liquid Aluminum." In: *Metall. Mater Trans. A* 48.6 (2017), pp. 3036-3045.

II M. Leitner, W. Schröer and G. Pottlacher. "Density of Liquid Tantalum and Estimation of Critical Point Data." In: *Int. J. Thermophys.* 39.11 (2018), p. 124.

III M. Leitner and G. Pottlacher. "Density of Liquid Niobium and Tungsten and the Estimation of Critical Point Data." In: *Metall. Mater Trans. A* 50.8 (2019), pp. 3646-3653.

8.1. Thermophysical Properties of Liquid Aluminum

M. Leitner, T. Leitner, A. Schmon, K. Aziz and G. Pottlacher. "Thermophysical Properties of Liquid Aluminum." In: *Metall. Mater Trans. A* 48.6 (2017), pp. 3036-3045. DOI: https://doi.org/10.1007/s11661-017-4053-6.

SHORT SUMMARY

A comprehensive set of thermophysical properties was obtained for aluminum making use of the ohmic pulse-heating and the electromagentic levitation method. All data are extensively compared to those reported in the literature.

REMARKS ON AUTHORSHIP

M. Leitner performed pulse-heating measurements to derive the thermophysical properties H, ρ, λ and a as well as critical point data. He wrote section II A, sections III A, B, C, D, E, G, H as well as section IV and V.
T. Leitner performed surface tension and density measurements by means of electromagnetic levitation under the supervision of **K. Aziz** and evaluated the obtained data. He wrote the sections related to electromagnetic levitation, II B and III F as well as parts of III A.
A. Schmon performed density measurements using the ohmic pulse-heating setup and evaluated the resulting raw data.
G. Pottlacher supervised the measurement and publication process, wrote *Abstract* and *Introduction* and was involved in the literature survey.

All authors were involved in the text revision process.

Thermophysical Properties of Liquid Aluminum

MATTHIAS LEITNER, THOMAS LEITNER, ALEXANDER SCHMON, KIRMANJ AZIZ, and GERNOT POTTLACHER

Ohmic pulse-heating with sub-microsecond time resolution is used to obtain thermophysical properties for aluminum in the liquid phase. Measurement of current through the sample, voltage drop across the sample, surface radiation, and volume expansion allow the calculation of specific heat capacity and the temperature dependencies of electrical resistivity, enthalpy, and density of the sample at melting and in the liquid phase. Thermal conductivity and thermal diffusivity as a function of temperature are estimated from resistivity data using the Wiedemann–Franz law. Data for liquid aluminum obtained by pulse-heating are quite rare because of the low melting temperature of aluminum with 933.47 K (660.32 °C), as the fast operating pyrometers used for the pulse-heating technique with rise times of about 100 ns generally might not be able to resolve the melting plateau of aluminum because they are not sensitive enough for such low temperature ranges. To overcome this obstacle, we constructed a new, fast pyrometer sensitive in this temperature region. Electromagnetic levitation, as the second experimental approach used, delivers data for surface tension (this quantity is not available by means of the pulse-heating technique) and for density of aluminum as a function of temperature. Data obtained will be extensively compared to existing literature data.

DOI: 10.1007/s11661-017-4053-6

I. INTRODUCTION

ALUMINUM is a silvery-whitish light metal. It is the third most common element occurring in the crust of the earth. The world aluminum statistics reports, for March 2016, the production of 4856 metric tons of aluminum worldwide. Aluminum is used in all kinds of industries, ranging from cans for drinks and foils to wrap food, to the building industry for roofing and windows, to the automotive and aerospace industries, where it is used for lightweight structures.

In production, aluminum is first melted and then undergoes different forming processes, such as casting, pressure die casting, and continuous casting. In current industrial practice, computer-based simulations allow modeling of casting, melting and remelting processes, heat transport, solidification shrinkage, residual stress, heat treatment, welding, forging, rolling, and cutting, or even predictions of microstructures. A key limitation to the successful introduction of these models is the lack of thermophysical data. Thus, experimentally obtained thermophysical properties of pure metals are of great importance as input parameters for various simulation tools and will lead to a better scientific understanding of liquid metals and alloys as well as help in the final production to reduce waste.

Within this article, we will present a full set of experimentally obtained thermophysical properties of solid and liquid aluminum that can be used as input parameters for numerical simulations. The data presented are extensively compared to existing literature values and the range of experimental uncertainty is given for each property.

II. EXPERIMENTAL PROCEDURE AND DATA REDUCTION

A. *Ohmic Pulse-Heating Experiments*

High-purity aluminum wires (99.999 at. pct) with a diameter of 0.5 mm (Catalogue No. AL501115, Advent) were investigated using an ohmic pulse-heating technique. The details of the experimental pulse-heating setup have already been described extensively in References 1 through 3.

The samples with about 60 mm length were treated with abrasive paper (grade 1200), cleaned with acetone, and subsequently resistively heated under N_2 atmosphere at a pressure of 2.3 bar, starting at room temperature. A current pulse peaking at about 10 kA was discharged through the specimens and measured using an inductive coil (Model Number 3025, Pearson Electronics). At the same time, the voltage drop against common ground was measured using two Mo-foil voltage knives attached horizontally to the wire with subsequent voltage division. Due to the high heating rates of about 2×10^8 K s^{-1} needed to avoid a loss of

MATTHIAS LEITNER, THOMAS LEITNER, and GERNOT POTTLACHER are with the Institute of Experimental Physics, Graz University of Technology, NAWI Graz, Petersgasse 16, 8010, Graz, Austria. Contact e-mail: pottlacher@tugraz.at ALEXANDER SCHMON is with the Patent Attorney Dipl.-Ing. Dr. Gernot Wirnsberger, Leoben, Austria. KIRMANJ AZIZ is with the EPCOS OHG a TDK Group Company, Deutschlandsberg, Austria.

The original version of this article was revised: corrections were made in the Results and Discussion section as detailed in the erratum.

Manuscript submitted December 2, 2016.

Article published online March 23, 2017

contact, the experiments had a relatively short duration of about 35 μs.

To relate the time-resolved voltage drop and current behavior to a temperature, the surface radiance was simultaneously monitored by a Peltier-cooled IR pyrometer operating at a mean effective wavelength of $\lambda_{\text{eff}} = 2315$ nm with approximately 390 nm effective bandwidth. In order to *in-situ* calibrate the pyrometer, the surface radiance at the melting plateau, observed in the radiance-over-time development, was assigned to the melting temperature of Al, *i.e.*, $T_{\text{m}} = 933.47$ K (660.32 °C).[4] Expressing the measured pyrometer signals by Planck's law of radiation, the surface radiance $J(T)$ measured at any time t can then be related to the observed radiance $J(T_{\text{m}})$ at the melting point by simply taking the ratio and solving for T:

$$T = \frac{c_2}{\lambda_{\text{eff}} \cdot \ln\left(\frac{J(T_{\text{m}})}{J(T)} \cdot \frac{\varepsilon(\lambda_{\text{eff}},T)}{\varepsilon(\lambda_{\text{eff}},T_{\text{m}})} \cdot \left\{ e^{\frac{c_2}{\lambda_{\text{eff}} \cdot T_{\text{m}}}} - 1 \right\} + 1\right)}, \quad [1]$$

where $c_2 = 0.014388$ m K is the second radiation constant. Due to the lack of spectral emissivity data at the extreme measuring wavelength, it was further assumed that the emissivity ε takes the value that is true at the melting point, *i.e.*, $\frac{\varepsilon(\lambda_{\text{eff}},T)}{\varepsilon(\lambda_{\text{eff}},T_{\text{m}})} = 1$, over the entire temperature range. Note that the assumption of constant emissivity is mostly feasible in the liquid phase, while this is usually not the case for the solid phase. The data presented in this publication thus focus on the liquid phase, while the solid phase data are also given as an overall estimate.

To obtain data for the density $D(T)$, an adapted fast CCD system taking shadowgraph images of the backlit expanding wire was used (details in Reference 5). The shadow images with an exposure time of 600 ns were captured about 5 μs apart. The diameter $d(T)$ as a function of temperature can then be obtained by evaluating the full-width-at-half-maximum in the calculated intensity profile of each image. By relating this temperature-dependent diameter to the diameter d_0 imaged before the experiment, the density can be derived using a room-temperature value of $D_0 = 2.70 \times 10^3$ kg m^{-3}.[6] The constraint $\frac{d_0}{d[298\text{ K}(25\text{ °C})]} = 1$ and, therefore, $D[298\text{ K}(25\text{ °C})] = D_0$ was applied for the solid phase data fitting.

$$D(T) = D_0 \cdot \left(\frac{d_0}{d(T)}\right)^2. \quad [2]$$

Note that using this approach, longitudinal expansion must be inhibited to a high degree. This is ensured by applying high heating rates, which have shown to result in an increased radial thermal expansion at the cost of absent longitudinal expansion.[7,8] Furthermore, it is crucial to achieve a nonmoving vertical liquid metal column in order to deduce precise diameters from the intensity profiles. Therefore, density measurements were conducted as separate experiments without voltage knives that can push the metal column. In addition, the wire length was shortened to about 40 mm to increase its stability.[8]

For nondensity experiments conducted with the pulse-heating apparatus, the electrical resistivity and the specific enthalpy can be derived. From the measured time-dependent voltage drop $U(t)$ across the investigated length l, the time-dependent current $I(t)$, and the diameter at room temperature d_0 (measured with a Keyence LS-7010 laser micrometer), the specific resistivity at initial geometry (IG) is obtained as

$$\rho_{\text{IG}}(t) = \frac{U(t)}{I(t)} \cdot \frac{d_0^2 \pi}{4 \cdot l}. \quad [3]$$

In order to correct for thermal volume expansion (VE), the radial expansion data obtained for density measurements are used. The correction is made under the assumption of absent longitudinal expansion, which is justified due to the experimental constraints, as described previously.

$$\rho_{\text{VE}}(T) = \rho_{\text{IG}}(T) \cdot \left(\frac{d(T)}{d_0}\right)^2 \quad [4]$$

Furthermore, the time-dependent specific enthalpy $H(t)$ starting from room temperature can be derived by integrating the power over time and relating it to the sample mass m that is calculated from room-temperature density D_0 and diameter d_0, as well as the distance between the voltage knives l,

$$H(t) = \frac{1}{m} \cdot \int_0^t U\left(t'\right) \cdot I\left(t'\right) \mathrm{d}t'. \quad [5]$$

Due to the isobaric characteristics of the experiment, the specific heat capacity at constant pressure c_{p} can be evaluated from the slope of the $H(T)$ curve:

$$c_{\text{p}} = \left(\frac{\partial H}{\partial T}\right)_{\text{p}}. \quad [6]$$

In order to estimate thermal conductivity $\lambda(T)$, the Wiedemann–Franz law was used. The Lorenz number was assumed constant at the theoretical value of $L = 2.45 \times 10^{-8}$ V^2 K^{-2}. This assumption is justified, as the phonon conductivity of Al is reported to be very small (for more information, see Klemens and Williams.[9])

$$\lambda(T) = \frac{L \cdot T}{\rho_{\text{VE}}(T)}. \quad [7]$$

Thermal diffusivity $a(T)$ can be estimated using thermal conductivity $\lambda(T)$, specific heat capacity at constant pressure c_{p}, and density $D(T)$. Note that applying the Wiedemann–Franz law to the respective equation and inserting Eqs. [4] and [2] yields an expression independent of thermal expansion.

$$a(T) = \frac{\lambda(T)}{c_p \cdot D(T)} \equiv \frac{L \cdot T}{c_p \cdot \rho_{IG}(T) \cdot D_0}. \quad [8]$$

Thermal diffusivity, therefore, can be estimated with a relatively low uncertainty.[10]

B. *Electromagnetic Levitation Experiments*

An electromagnetic levitation (EML) setup was used to investigate the surface tension of liquid aluminum as well as to obtain additional reference data for the density of aluminum in the liquid phase. A detailed description of the EML setup was already part of precedent publications.[11–14]

In the EML experiments, small aluminum samples of high purity (99.999 at. pct) with a mass in the range of 100 to 140 mg were investigated. The samples were cut off from a high-purity aluminum rod with a diameter of 5.0 mm (Catalogue No. AL501907, Advent). Each sample was cleaned with acetone in an ultrasonic bath, followed by determining the mass on a precision balance.

A clean environment in the probe chamber was ensured by first evacuating the chamber to a pressure lower than 5×10^{-6} mbar and then flooding it close to atmospheric pressure (850 mbar) with high-purity gas mixtures of argon with 2.4 vol. pct hydrogen (AirLiquide Arcal10) and helium with 4 vol. pct hydrogen (AirLiquide custom gas mixture). The ratio of the gas mixtures was adapted throughout the experiment in order to control the heat dissipation from the sample and, thus, realize different sample temperatures. The idea of using hydrogen-enriched gas mixtures was to hinder aluminum oxide (alumina) formation and reduce already present aluminum oxide on the sample surface back to aluminum and vapor.[15]

The contactless temperature measurement was performed *via* a commercial NIR pyrometer (IMPAC IGA 6 Advanced, LumaSense), operating in the bandwidth of 1.45 to 1.80 μm. The temperature values recorded by the software (InfraWin 5.0.1.52) relate to the blackbody temperature (T_{bb}) of the detected radiance. In order to obtain the true temperature, the emissivity at a reference temperature was determined by assigning the recorded blackbody temperature at the solidification plateau of the sample under investigation to the real melting temperature of Al, *i.e.*, T_m = 933.47 K (660.32 °C),[4] using formula [9], as given in Reference 16

$$\varepsilon = \exp\left(\frac{c_2}{\lambda} \cdot \left(\frac{1}{T_m} - \frac{1}{T_{bb}}\right)\right) \quad [9]$$

with c_2 = 0.014388 m K, the second radiation constant. Assuming that emissivity ε does not change its value in the liquid phase over the entire temperature range, the true temperature (T_t) of each recorded blackbody temperature value can be recovered:[16]

$$T_t = \left(\frac{1}{T_{bb}} + \frac{\lambda}{c_2} \cdot \ln \varepsilon\right)^{-1}. \quad [10]$$

In the EML experiment, a high-frequency current (≈380 kHz) is applied to the levitation coil that generates an inhomogeneous radio frequency electromagnetic field, inducing eddy currents in the sample material. These eddy currents, according to Lenz's rule, generate an opposing electromagnetic field leading to a repulsive force that pushes the sample towards areas of lower field strength.[17]

Simultaneously, the ohmic losses of the eddy currents heat the sample to the liquid phase. Stable temperatures are obtained when heat dissipation by the atmosphere in the chamber and induced heating power are balanced.

When liquefied, oscillations of the sample around its equilibrium shape can be observed. Those variations in the radius of the sample can be described mathematically by spherical harmonics Y_l^m. Lord Rayleigh deduced a relation between the frequency of the oscillation of a spherical droplet and the surface tension (γ) that acts as the restoring force, but it is only valid under nonterrestrial conditions where the sample is force free and not rotating.[18] The fundamental frequency, called Rayleigh frequency (ν_R), is obtained for $l = 2$ and is fivefold degenerated (with M being the sample's mass):

$$\nu_R^2 = \frac{8 \cdot \gamma}{3 \cdot \pi \cdot M}. \quad [11]$$

Under terrestrial conditions, those requirements are violated and the degeneracy is removed. Instead of one single oscillation frequency, up to five different oscillation modes can be observed for aspherical, rotating droplets. Cummings and Blackburn[19] derived a sum rule that recovers the original Rayleigh frequency from those five oscillation frequencies so that the surface tension can be calculated from the frequencies observed in the experiment by

$$\gamma = \frac{3}{8} \cdot \pi \cdot M \cdot \left[\frac{1}{5} \cdot \left(\nu_{2,0}^2 + 2 \cdot \nu_{2,1}^2 + 2 \cdot \nu_{2,2}^2\right) - \nu_\tau^2 \cdot \left(1.9 + 1.2 \cdot \left(\frac{z_0}{a}\right)^2\right)\right], \quad [12]$$

$$z_0 = \frac{g}{2 \cdot (2 \cdot \pi \cdot \nu_\tau)^2}, \quad [13]$$

$$a = \sqrt[3]{\frac{3 \cdot M}{4 \cdot \pi \cdot D}}, \quad [14]$$

where z_0 is proportional to the relative position of the droplet in the field; g is the gravitational acceleration; and a is the radius of the sample, which can be calculated from the sample's mass M and density D. The term ν_τ in Eqs. [12] and [13] is the mean value of the squared translation frequencies in all three spatial dimensions denoted by ν_i with i = 1, 2, 3.

$$\nu_\tau^2 = \frac{1}{3} \cdot \sum_{i=1}^{3} \nu_i^2. \quad [15]$$

The value $v_{2,0}$ in Eq. [12] is the observed frequency for the oscillation mode $l = 2$, $m = 0$. The terms $v_{2,1}$ and $v_{2,2}$ in Eq. [12] can be calculated by

$$v_{2,m} = \frac{1}{2} \cdot \left(v_{2,+m}(\Omega) + v_{2,-m}(\Omega) \right) \qquad [16]$$

since the split of the observed frequencies for the oscillation modes $l = 2$, $m = 1, 2$ due to the rotation of the sample with frequency Ω denoted by $v_{2,\pm m}(\Omega)$ is symmetrical.

The sample movement and oscillations were recorded from the top taking advantage of the vertical axis symmetry. A high-speed camera recorded 4096 images per temperature point. The framerate of the camera, typically 600 frames per second (fps) at a resolution of 1024 px · 1024 px, had to be decreased to a value as low as 200 fps for low sample temperatures to allow shutter times as high as 5 ms. This adjustment was necessary in order to ensure a sufficient brightness on the recorded images, since the spectral radiance in the visible range declined to a very low level at temperatures close to the melting point.

The image series were analyzed using an edge-detection software that detects position and size of the sample on the images. The software generates a table that holds for each image the coordinates of the center of mass as well as the radii as a function of the azimuthal angle in steps of 5 deg. Using this table, a spectrum of the coordinates as well as of the radii can be obtained by applying a fast Fourier transform to the according time series.

In order to identify the five oscillation frequencies, additional spectra of the sum and difference of two arbitrary perpendicular radii were used, as presented in Reference 13.

For the density measurement, a series of 4100 shadowgraph images acquired from the side were recorded at a framerate of 120 fps for each temperature point. From these shadowgraph images, the mean shape of the sample was determined by a software using edge detection algorithms to determine the position and size of the sample in the images.

High-precision ball bearing spheres of known diameter levitated by an argon airflow through the cooling nozzle were used to relate the area of the sample on the shadowgraph images to a real (metric) quantity. Assuming vertical axis symmetry of the droplet, the volume is calculated and, with the known sample mass, the density is determined.

III. RESULTS AND DISCUSSION

This section discusses and summarizes the new results in graphical form. It also provides the necessary polynomial coefficients to calculate the physical properties at desired temperatures (Table I). Furthermore, a collection of data values in steps of 50 K is given in Table II. The deviation of reported literature values with respect to our newly obtained values is given in parentheses within the text. Note that an aluminum oxide layer (nanometers) will always form on the surface. The effect on temperature reduction is negligible within the investigated temperature range, however, due to the transparency of the oxide at the measuring wavelength.[20,21]

A. *Density*

Density was determined by means of pulse-heating and EML. In Figure 1, the results are depicted together with literature values. Extrapolating the quadratic least-squares fit describing the solid phase to the melting temperature, we obtain a density of 2514 kg m^{-3} for the onset of melting. Upon melting, the density decreases to a value of 2391 kg m^{-3}. The data obtained by averaging seven levitation experiments show a similar temperature coefficient but are shifted to lower values. However, the uncertainties of the two datasets overlap.

For comparison to other EML experiments, datasets generated from the fit coefficients reported in References 22 and 23 are depicted in Figure 1. Whereas the data of Schmitz *et al.*[23] are in good agreement with the reference data from the literature, the data of Peng *et al.*[22] show a shift to lower density values similar to our data, but the shift and its cause are not discussed. The shift of EML data to smaller density values in this publication is assumed to stem from a slight systematic overestimation of the measured sample volume caused by strong deformation oscillations or even a slight static deformation caused by the levitation coils, resulting in a violation of vertical axis symmetry. The fact that heavy samples showing larger deformations also show a bigger scatter in the density data is a strong indication for this thesis. The authors plan to extend the current experimental setup in a manner that will permit simultaneous observation of the sample from two sides in order to account for this effect by detecting deformations that violate vertical axis symmetry.[8]

The accordance of the pulse-heating data to reported literature data is promising. Assael *et al.*[24] recommend values for the liquid phase density of Al that deviate less than 0.8 pct from our data over the entire liquid phase. At the onset of melting, Mills[25] reports a density of 2558 kg m^{-3} (+1.8 pct) and 2380 kg m^{-3} after the melting transition (−0.5 pct). Touloukian[26] reports a decrease from 2542 kg m^{-3} (+1.1 pct) to 2379 kg m^{-3} (−0.5 pct) upon melting. In *Smithells Metals Reference Book*,[27] we find a value of 2385 kg m^{-3} (−0.3 pct) at the beginning of the liquid phase. Drotning[28] reports a density of 2389 kg m^{-3} (−0.1 pct) directly after melting. From specific volume data reported by Gathers,[29] the density at the beginning of the liquid phase was calculated as 2418 kg m^{-3} (+1.1 pct). His measurements were conducted at a pressure of 0.3 GPa.

B. *Electrical Resistivity*

Figure 2 depicts electrical resistivity as a function of temperature. Data of electrical resistivity and specific enthalpy were obtained by averaging six consecutive measurements. The dashed line represents the melting temperature, while the solid lines show the applied

Table I. Polynomial Coefficients to Describe the Results of the Present Study for Density D and Electrical Resistivity at Initial Geometry ρ_{IG}, and Corrected for Volume Expansion ρ_{VE}, Specific Enthalpy H, Thermal Conductivity λ, Thermal Diffusivity a, as well as Surface Tension γ of Al as a Function of Temperature T

Property y	Unit	Polynomial Coefficients $y = a + bT + cT^2$			Range T (K)	State
		a	b	c		
$D(T)$	kg m^{-3}	2648	0.322	-4.99×10^{-4}	$592 \le T \le T_m$	s
$D(T)$	kg m^{-3}	2670	−0.299	—	$T_m \le T \le 1680$	l
$D^*(T)$	kg m^{-3}	2553	−0.267	—	$T_m \le T \le 1495$	l
$\rho_{IG}(T)$	$\mu\Omega$ m	−0.014	1.379×10^{-4}	—	$712 \le T \le T_m$	s
$\rho_{IG}(T)$	$\mu\Omega$ m	0.128	1.063×10^{-4}	—	$T_m \le T \le 1491$	l
$\rho_{VE}(T)$	$\mu\Omega$ m	−0.030	1.638×10^{-4}	—	$712 \le T \le T_m$	s
$\rho_{VE}(T)$	$\mu\Omega$ m	0.097	1.681×10^{-4}	—	$T_m \le T \le 1491$	l
$H(T)$	kJ kg^{-1}	−379	1.199	—	$712 \le T \le T_m$	s
$H(T)$	kJ kg^{-1}	48	1.127	—	$T_m \le T \le 1491$	l
$\lambda(T)$	W m^{-1} K^{-1}	248	−0.067	—	$712 \le T \le T_m$	s
$\lambda(T)$	W m^{-1} K^{-1}	33.9	7.892×10^{-2}	-2.099×10^{-5}	$T_m \le T \le 1491$	l
$a(T)$	10^{-5} m^2 s^{-1}	7.023	-9.31×10^{-4}	—	$712 \le T \le T_m$	s
$a(T)$	10^{-5} m^2 s^{-1}	0.965	0.31×10^{-2}	-6.306×10^{-7}	$T_m \le T \le 1491$	l
$\gamma^*(T)$	mN m^{-1}	993	−0.127	—	$T_m \le T \le 1550$	l

The terms s and l denote the solid and liquid phase, respectively. Measurements performed with EML are marked with an asterisk. The temperature range of applicability is given. T_m = 933.47 K (660.32 °C) designates the melting point.

Table II. Thermophysical Properties of Al for Different Temperatures T

T (K)	T (°C)	D (kg m^{-3})	ρ_{IG} ($\mu\Omega$ m)	ρ_{VE} ($\mu\Omega$ m)	H (kJ kg^{-1})	λ (W m^{-1} K^{-1})	a (10^{-5} m^2 s^{-1})	γ (mN m^{-1})
600	326.85	2662	—	—	—	—	—	—
650	376.85	2646	—	—	—	—	—	—
700	426.85	2629	—	—	—	—	—	—
750	476.85	2609	0.0894	0.0929	520	197.8	6.325	—
800	526.85	2586	0.0963	0.1010	580	194.4	6.278	—
850	576.85	2561	0.1032	0.1092	640	191.1	6.232	—
900	626.85	2534	0.1101	0.1174	700	187.7	6.185	—
(s)933.47	660.32	2514*	0.1147*	0.1228*	740*	185.5*	6.154*	—
(l)933.47	660.32	2391*	0.2272*	0.2539*	1100*	89.3*	3.309*	874.9*
950	676.85	2386	0.2290*	0.2567*	1119*	89.9*	3.341*	872.7*
1000	726.85	2371	0.2343*	0.2651*	1175*	91.8*	3.434*	866.3*
1050	776.85	2356	0.2396*	0.2735*	1231*	93.6*	3.525*	860.0
1100	826.85	2341	0.2449*	0.2819*	1288*	95.3*	3.612*	853.6
1150	876.85	2326	0.2502	0.2903	1344	96.9	3.696	847.3
1200	926.85	2311	0.2556	0.2987	1400	98.4	3.777	840.9
1250	976.85	2296	0.2609	0.3071	1457	99.8	3.855	834.5
1300	1026.85	2281	0.2662	0.3155	1513	101.0	3.929	828.2
1350	1076.85	2266	0.2715	0.3239	1569	102.2	4.001	821.8
1400	1126.85	2251	0.2768	0.3323	1626	103.2	4.069	815.5
1450	1176.85	2236	0.2821	0.3407	1682	104.2	4.134	809.1
1500	1226.85	2222	0.2874	0.3492	1739	105.1	4.196	802.8
1550	1276.85	2207	—	—	—	—	—	796.4
1600	1326.85	2192	—	—	—	—	—	—
1650	1376.85	2177	—	—	—	—	—	—

*Values extrapolated to the melting temperature T_m: solid state (s) and liquid state (l).

D: density obtained *via* pulse-heating, ρ_{IG}: electrical resistivity at IG, ρ_{VE}: electrical resistivity corrected for VE, H: specific enthalpy, λ: thermal conductivity, a: thermal diffusivity, and γ: surface tension.

least-squares fits. Due to the fast heating rates, the transition from the solid to the liquid phase is smeared out rather than being pronounced as expected for pure elements. The fits, therefore, were extrapolated to the melting temperature. Note that data in the solid phase must be regarded as an estimate, since the temperature determination is based on the assumption of a non-changing emissivity in the liquid phase.

In the initial geometry, a value of ρ_{IG} = 0.1147 $\mu\Omega$ m is obtained at T_m. At the end of melting, we see a value of 0.2272 $\mu\Omega$ m. Consequently, we observe a jump in resistivity of 0.1125 $\mu\Omega$ m upon the melting process.

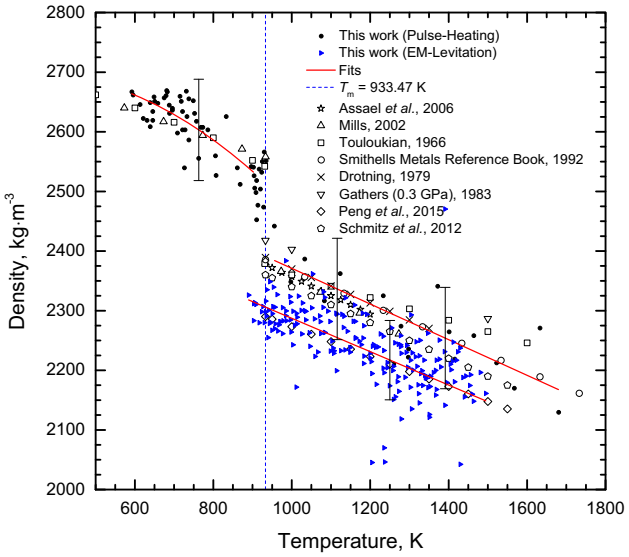

Fig. 1—Density of Al. The dashed line marks the melting temperature. The solid lines represent the least-squares fits to best describe the experimental data determined in this work. Solid circles: Data obtained by pulse-heating. Solid triangles: Data obtained by EML. Diamonds: Peng *et al.*,[22] pentagons: Schmitz *et al.*,[23] stars: Assael *et al.*,[24] up-triangles: Mills,[25] squares: Touloukian,[26] big circles: *Smithells Metals Reference Book*,[27] crosses: Drotning,[28] and down-triangles: Gathers (0.3 GPa).[29]

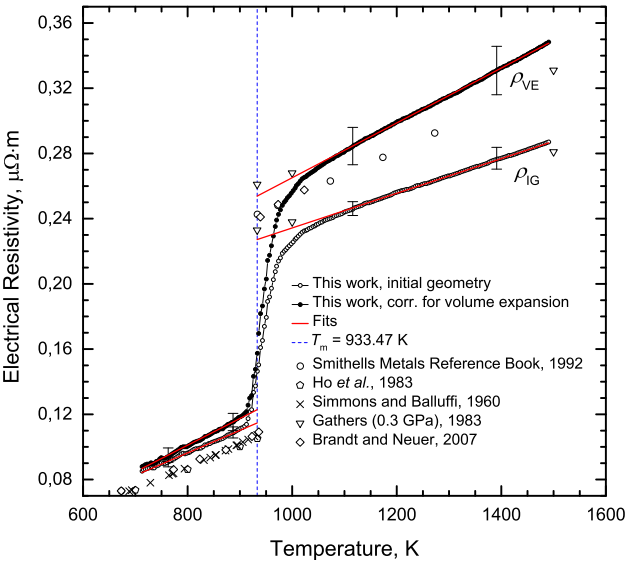

Fig. 2—Electrical resistivity of Al in initial geometry (open circles) and corrected for volume expansion (solid circles). The dashed line marks the melting point. The solid lines show the least-squares fits to the experimental data determined in this work. Diamonds: Brandt and Neuer,[32] down-triangles: Gathers, measured at 0.3 GPa,[29] big circles: *Smithells Metals Reference Book*,[27] crosses: Simmons and Balluffi,[31] and pentagons: Ho *et al.*[30]

The data obtained in IG were corrected using the thermal expansion data measured for density determination. For the corrected electrical resistivity ρ_{VE}, values of 0.1228 and 0.2539 $\mu\Omega$ m were observed at the onset of melting and at the end of melting, respectively. This yields an increase in resistivity of 0.1311 $\mu\Omega$ m upon melting.

The recommended values reported by Ho *et al.*[30] were not corrected for thermal expansion. At the melting point, they report a resistivity of 0.10516 $\mu\Omega$ m (−8.3 pct). Simmons and Balluffi[31] observe a corrected value of 0.10733 $\mu\Omega$ m (−12.6 pct) at the melting point. Brandt and Neuer[32] found a corrected resistivity value of 0.1092 $\mu\Omega$ m (−11.1 pct) at the onset of melting and 0.2410 $\mu\Omega$ m (−5.1 pct) at the end of melting. This yields a jump of 0.1318 $\mu\Omega$ m upon melting, which is in excellent accordance with our newly obtained data (+0.5 pct). The data for the liquid phase reported in *Smithells Metals Reference Book*[27] were also corrected for thermal expansion. They recommend a value of 0.2425 $\mu\Omega$ m at the beginning of the liquid phase (−4.5 pct). Gathers reports liquid phase data for both the uncorrected and the corrected electrical resistivity.[29] These measurements were conducted under a pressure of 0.3 GPa but still show good agreement with our data. For the uncorrected and corrected resistivity, values of 0.233 $\mu\Omega$ m (+2.6 pct) and 0.261 $\mu\Omega$ m (+2.8 pct) are reported after the melting transition. The coefficients of the four least-squares fits are summarized in Table I, including the range of applicability.

C. *Enthalpy*

Specific enthalpy as a function of temperature is depicted in Figure 3, where the value at room temperature was chosen as zero. Upon melting, we observe a jump from 740 to 1100 kJ kg^{-1} yielding a heat of fusion of ΔH = 360 kJ kg^{-1}.

A considerable amount of reference data for specific enthalpy and specific heat is present in the literature. Unfortunately, the available data are given in numerous different units, which complicates intuitive comparison. In order to keep the integrity of the discussed literature data, these values are given in their original units. However, for the sake of comparison, the literature data were additionally converted into SI units and are summarized in Table III.

Mills reports a value of 663 kJ kg^{-1} (−10.4 pct) at the beginning and 1060 kJ kg^{-1} (−3.6 pct) at the end of melting.[25] This results in a heat of fusion of ΔH = 397 kJ kg^{-1} (+10.3 pct). Values reported by McDonald[33] are 4328 cal mol^{-1} (−9.3 pct) for the onset and 6888 cal mol^{-1} (−2.8 pct) at the end of melting, yielding a latent heat of ΔH = 2560 cal mol^{-1} (+10.3 pct). Values of Schmidt *et al.*[34] show an increase from 17,430 J (g-atom)$^{-1}$ (−12.7 pct) to 28,130 J (g-atom)$^{-1}$ (−5.2 pct) upon melting. Consequently, they report a heat of fusion of ΔH = 10,700 J (g-atom)$^{-1}$ (+10.2 pct). The recommended data given by Desai[35] are 18,090 J mol^{-1} (−9.4 pct) at the beginning of melting and 28,670 J mol^{-1} (−3.4 pct) at the end, yielding ΔH = 10,580 J mol^{-1} (+8.9 pct). Desai states an uncertainty of 1.4 pct for his data.

Specific enthalpy data are also reported by Marchidan and Ciopec,[36] Buyco and Davis,[37] and Ditmars *et al.*[38] for the solid phase only. Marchidan and Ciopec report data up to a temperature of 879.26 K (606.11 °C) that are in close agreement to the literature data

discussed earlier in the text. The data of Buyco and Davis, on the other hand, 201.1 cal g^{-1} (+13.8 pct) at the beginning of melting, show a significant offset compared to the values discussed earlier, but are consistent with the value of Ditmars, *i.e.*, 22,521 J mol^{-1} (+12.8 pct), at melting. At the beginning of the liquid phase, Gathers proposes a value of 1068 kJ kg^{-1} (+2.9 pct).[29] These measurements were conducted under a pressure of 0.3 GPa but are in close agreement to the other data reported. The fit coefficients for enthalpy *vs* temperature are listed in Table I.

The specific heat at constant pressure is obtained from the slope of the temperature-dependent specific enthalpy. From Table I, c_p in the liquid phase is 1.127 kJ kg^{-1} K^{-1}.

Mills[25] reports a value of c_p = 1.18 J g^{-1} K^{-1} (+4.7 pct), and McDonald reports 7.59 cal mol^{-1} K^{-1} (+4.5 pct).[33] Buyco and Davis[37] present a recommended value of c_p = 0.2813 cal g^{-1} K^{-1} (+4.5 pct). Desai recommends a value of c_p = 31.757 J mol^{-1} K^{-1} (+4.4 pct) with an uncertainty of 3 pct.[35] The specific heat in the liquid phase proposed by Schmidt *et al.*[34] varies between c_p = 27.8 J (g-atom grad)$^{-1}$ (−8.6 pct) and c_p = 29.9 J (g-atom grad)$^{-1}$ (−1.7 pct) with an uncertainty of 3 pct.

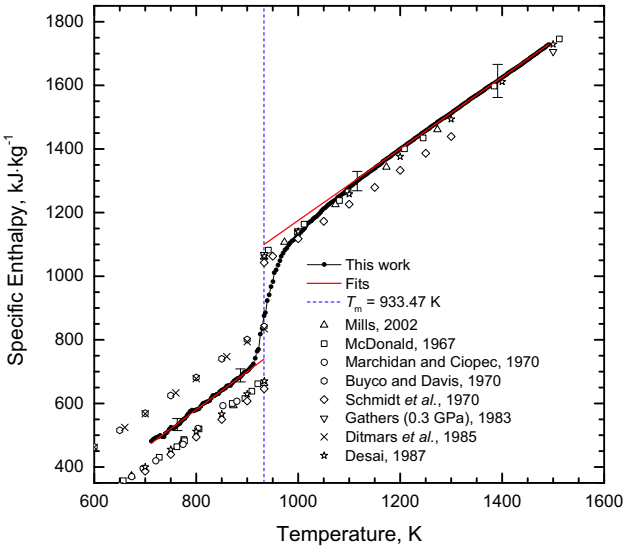

Fig. 3—Specific enthalpy of Al. The dashed line indicates the melting temperature. The solid lines mark the applied linear fits to the experimental data determined in this work (solid circles). Up-triangles: Mills,[25] squares: McDonald,[33] diamonds: Schmidt *et al.*,[34] stars: Desai,[35] circles: Marchidan and Ciopec,[36] hexagons: Buyco and Davis,[37] crosses: Ditmars *et al.*,[38] and down-triangles: Gathers, measured at 0.3 GPa.[29]

D. *Thermal Conductivity*

In Figure 4, thermal conductivity estimated from our data using the Wiedemann–Franz law is presented as a function of temperature. The liquid phase data conform well with the reported literature data.

At the beginning of melting, we obtain a value of λ = 185.5 W m^{-1} K^{-1}. A drop in thermal conductivity is observed, resulting in 89.3 W m^{-1} K^{-1} at the end of melting.

Touloukian *et al.*[39] report λ = 211 W m^{-1} K^{-1} (+13.7 pct) at the onset and λ = 90.7 W m^{-1} K^{-1} (+1.6 pct) at the end of the melting process. For the solid phase, Mills[25] proposes a thermal conductivity on the basis of the Touloukian *et al.* values. At the beginning of the liquid phase, Mills reports a value of λ = 91 W m^{-1} K^{-1} (+1.9 pct). *Smithells Metals Reference Book*[27] states λ = 94.03 W m^{-1} K^{-1} (+5.3 pct) at the end of melting. Brandt and Neuer[32] calculated a value of λ = 209.6 W m^{-1} K^{-1} (+13 pct) at the end of the solid phase and λ = 95.3 W m^{-1} K^{-1} (+6.7 pct) at the beginning of the liquid phase. It can be seen from Figure 4 that their data are in close agreement to the values reported by Mills and Touloukian *et al.* as well as the recommended data given in *Smithells Metals Reference Book* for the liquid phase. Giordanengo *et al.*[40] report a value at the beginning of the liquid phase that is consistent with those of *Smithells Metals Reference Book* and Brandt and Neuer, *i.e.*, λ = 96.2 W m^{-1} K^{-1} (+7.7 pct). The slope at the beginning of the liquid phase, however, is higher so that the deviation with respect to our data rises to 12.3 pct at a temperature of 1400 K (1127 °C).

The data of Brandt and Neuer[32] indicate that the Wiedemann–Franz law, together with the theoretically predicted Lorenz number, is indeed also applicable at

Table III. Comparison of Specific Enthalpy Values at the End of the Solid Phase $H_S(T_m)$ and at the Beginning of the Liquid Phase $H_l(T_m)$ as well as the Heat of Fusion ΔH. In addition, the Specific Heat c_p in the Liquid Phase is Given

	$H_S(T_m)$ (kJ kg^{-1})	$H_l(T_m)$ (kJ kg^{-1})	ΔH (kJ kg^{-1})	c_p (kJ kg^{-1} K^{-1})
This work	740	1100	360	1.127
Mills[25]	663	1060	397	1.18
McDonald[33]	671.5	1069	397.2	1.18
Schmidt *et al.*[34]	646.03	1042.6	396.6	1.03
Desai[35]	670.50	1062.6	392.1	1.1771
Buyco and Davis[37]	841.8	—	—	1.178
Ditmars *et al.*[38]	834.73	—	—	—
Gathers[29]	—	1068	—	—

For conversion into SI units, the factor 4.186 cal mol^{-1} and a molar weight of 26.98 g mol^{-1} were used.

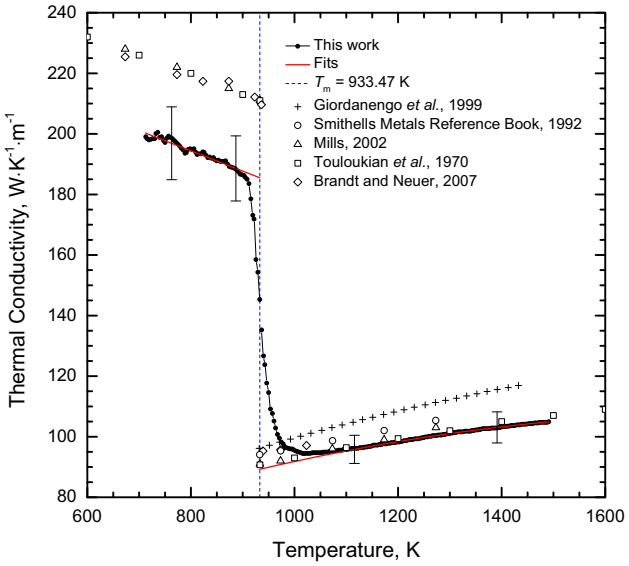

Fig. 4—Thermal conductivity of Al estimated using the Wiedemann–Franz law. The dashed line marks the melting temperature. The solid lines represent least-squares fits to the experimental data determined in this work (solid circles). Up-triangles: Mills,[25] diamonds: Brandt and Neuer,[32] circles: *Smithells Metals Reference Book*,[27] squares: Touloukian *et al.*,[39] and pluses: Giordanengo *et al.*[40]

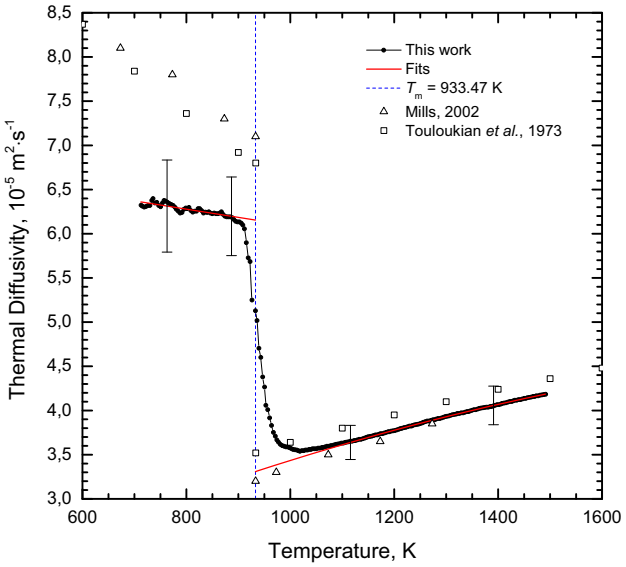

Fig. 5—Thermal diffusivity of Al. The dashed line indicates the melting temperature. The solid lines represent the least-squares fits applied to represent the data determined in this work (solid circles). Up-triangles: Mills,[25] squares: Provisional values of Touloukian *et al.*[41]

the end of the solid phase. It can be shown that our lower thermal conductivity in the solid phase is a direct result of our higher electrical resistivity applied in the Wiedemann–Franz law.

E. *Thermal Diffusivity*

By applying the Wiedemann–Franz law, thermal diffusivity can be estimated *via* the uncorrected electrical resistivity, the room-temperature density, and the specific heat derived from our $H(T)$ behavior (Figure 5). At the end of the solid phase, we report a value of $a = 6.154\ 10^{-5}\ \mathrm{m^2\ s^{-1}}$. Upon melting, thermal diffusivity decreases. At the end of the melting transition, we obtain a value of $a = 3.309\ 10^{-5}\ \mathrm{m^2\ s^{-1}}$.

Thermal diffusivity at the end of the solid phase reported by Mills[25] is $a = 7.1 \times 10^{-5}\ \mathrm{m^2\ s^{-1}}$ (+15.4 pct). Touloukian *et al.*[41] gives a value of $a = 6.80 \times 10^{-5}\ \mathrm{m^2\ s^{-1}}$ (+10.5 pct). The discrepancy in the solid phase is again caused by the discrepancy in solid phase electrical resistivity. The behavior in the liquid phase is consistent with literature data, Mills reporting $a = 3.2 \times 10^{-5}\ \mathrm{m^2\ s^{-1}}$ (−3.3 pct) and Touloukian *et al.* giving a provisional value of $a = 3.52 \times 10^{-5}\ \mathrm{m^2\ s^{-1}}$ (+6.4 pct) at the end of melting. The coefficients needed for the calculation of the newly obtained fits are summarized in Table I.

F. *Surface Tension*

Surface tension was determined by means of EML. Figure 6 depicts the results of six experiments together with reference data from literature. Due to the low radiance in the visible spectrum of aluminum at low

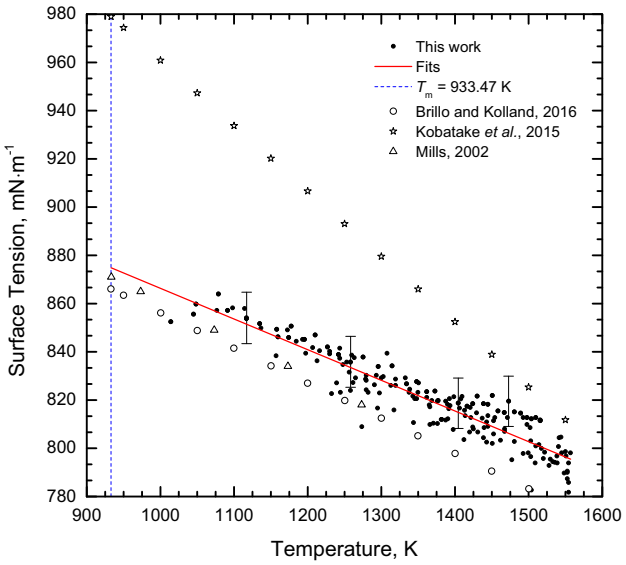

Fig. 6—Surface tension of Al. The dashed line marks the melting temperature. The solid line represents the least-squares fit to best describe the experimental data determined in this work. Solid circles: This work. Triangles: Mills,[25] stars: Kobatake *et al.*,[45] and circles: Brillo and Kolland.[44]

temperatures, data could be obtained just as close as 1014 K ± 21 K to the melting point. The surface tension at the melting point was extrapolated from the linear fit of the data yielding a value of 875 mN m^{-1}. Datasets generated from the fit coefficients reported in 44 and 45 are added to Figure 6 or comparison with other electromagnetic levitation experiments.

Numerous publications of surface tension data of pure aluminum based on different measurement

techniques are available, but only selected publications are used here for comparison since the specification whether or not the sample material was oxygen saturated is crucial. Our samples are assumed to be oxygen saturated as the oxygen contamination of the surface is practically inevitable unless enormous effort is expended in the preparation of the experiment (*e.g.*, vacuum transfer chamber) since a nanometer-thick oxide layer[42] will form immediately after exposure of the sample to regular air.

Mills[25] data, based on a literature review by Keene,[43] have been suggested to represent oxygen saturated aluminum. The experimental data of this work are in good agreement with the reference values of Mills, who reported a surface tension of 871 mN m^{-1} (−0.5 pct) at the melting point. Our data coincide within measurement uncertainty with recent data from Brillo and Kolland.[44] Using an EML setup, they reported a surface tension of 866 mN m^{-1} (−1.0 pct) at the melting point. For the sake of completeness, data from Kobatake *et al.*[45] for pure aluminum under oxygen-reduced conditions are also depicted in Figure 6, showing a significantly higher surface tension value at the melting point of 979 mN m^{-1} (+11.9 pct) and a steeper slope for the temperature dependence.

G. *Viscosity*

Although our laboratory is not capable of measuring viscosity, for the sake of completeness, we cite the equation recommended by Assael *et al.*[24]

$$\log_{10}\left(\frac{\eta}{\eta^0}\right) = -a_1 + \frac{a_2}{T} \quad 933 \le T(\mathrm{K}) \le 1270,$$

where η^0 = 1 mPa s, a_1 = 0.7324, and a_2 = 803.49 K. This equation is reported with a standard deviation of 13.7 pct at the 95 pct confidence level.

H. *Critical Point Data*

By extrapolating the liquid density data obtained by pulse-heating, the critical temperature T_c and the critical density ρ_c were estimated according to the algorithm given in the publication of Schröer and Pottlacher,[46] implemented in MATLAB R2016a.

$$T_c = \left(4.5\,^{+1.1}_{-0.7}\right) \times 10^3\ \mathrm{K}$$
$$\rho_c = (0.55 \pm 0.04)\ \mathrm{g\ cm^{-3}}.$$

Morel *et al.*[47] estimated T_c and ρ_c with different methods. Giving a full review, they recommend a critical temperature of $T_c = (6.7 \pm 0.8) \times 10^3$ K, which is almost 50 pct higher than our estimated value. However, the estimated values reported by different authors show a broad variation, ranging from 5115 K (5388 °C) (+13.6 pct)[48] to 9502 K (9775 °C) (+111 pct).[49] Also, further reported literature values for the critical density are as low as ρ_c = 0.28 g cm^{-3} (−49 pct)[50] and as high as ρ_c = 1.03 g cm^{-3} (+87 pct).[51] The critical density values reported by Morel *et al.*[47] are 0.566 g cm^{-3} (+2.9 pct) and 0.556 g cm^{-3} (+1.1 pct), respectively, which is in close agreement to our value.

IV. UNCERTAINTIES

The uncertainties in this work were estimated according to the *Guide to the Expression of Uncertainty in Measurement*[52] and are reported with a coverage factor of k = 2. Note that errors in the temperature determination due to the unknown behavior of the emissivity cannot be considered. The effect will be notable, in particular, in the solid phase, while in the liquid phase, the resulting error is typically very small. An elaborate investigation of the individual contributions to the uncertainty budgets for the setup at Graz, University of Technology, can be found in References 53, 8, and 54. As a detailed description would go well beyond the scope of this document, we give the overall uncertainties for the reported quantities in Table IV. The uncertainties for the critical temperature and the critical density were estimated from the uncertainty of the two coefficients of the $D(T)$ equation.

V. CONCLUSIONS

Thermophysical properties of aluminum were measured using two approaches. First, by means of ohmic pulse-heating, density, electrical resistivity, and specific enthalpy were obtained. Subsequently, thermal conductivity and thermal diffusivity were estimated from the derived data. Second, EML was used to measure the surface tension and the density in the liquid phase.

The newly obtained results, ranging about 600 K into the liquid phase, show excellent agreement with the literature data. The data are represented in the form of fit equations as well as in tabular form and provide another set of independent data for this important material.

Table IV. Relative Expanded Uncertainties (k = 2) for the Density D Obtained by Pulse-Heating, the Electrical Resistivity at IG ρ_{IG} and Corrected for VE ρ_{VE}, the Jump in Resistivity $\Delta\rho_{IG}$ and $\Delta\rho_{VE}$, Specific Enthalpy H, Latent Heat ΔH, Specific Heat Capacity at Constant Pressure c_p, Thermal Conductivity λ, Thermal Diffusivity a and Surface Tension γ

	D	ρ_{IG}	$\Delta\rho_{IG}$	ρ_{VE}	$\Delta\rho_{VE}$	H	ΔH	c_p	λ	a	γ
s	±3.3 pct	±3.4 pct	±5.7 pct	±4.8 pct	±8.9 pct	±3.5 pct	±12 pct	±5.3 pct	±6.1 pct	±8.2 pct	—
l	±3.8 pct	±2.4 pct		±4 pct		±3.3 pct		±4 pct	±5 pct	±5.4 pct	±1.5 pct

The terms s and l denote the solid and liquid phases.

In addition, critical temperature and critical density were estimated by extrapolating the liquid phase density to high temperatures. The so-obtained critical temperature is considerably lower than most values reported in the literature. The critical density, however, lies somewhere in the middle field in the broad range of reported values.

ACKNOWLEDGMENTS

Open access funding provided by Graz University of Technology. This work was partially funded by the Austrian Science Fund (FWF), Project No. P23838-N20, and the Austrian Research Promotion Agency (FFG), Project "Surfacetension-Steel" (No. 855678).

OPEN ACCESS

REFERENCE

1. A. Schmon, K. Aziz, M. Luckabauer, and G. Pottlacher: *Int. J. Thermophys.*, 2015, vol. 7, pp. 1618–26.
2. B. Wilthan, C. Cagran, C. Brunner, and G. Pottlacher: *Thermochim. Acta*, 2004, vol. 415, pp. 47–54.
3. C. Cagran, T. Hüpf, B. Wilthan, and G. Pottlacher: *High Temp.-High Press.*, 2008, vol. 37, pp. 205–19.
4. H. Preston-Thomas: *Metrologia*, 1990, vol. 27, pp. 3–10.
5. G. Pottlacher and T. Hüpf: in *Thermal Conductivity 30/Thermal Expansion 18*, D.S. Gaal, ed., DEStech Publications, Inc., Lancaster, 2010, pp. 195–206.
6. D. R. Lide, Ed.: *CRC Handbook of Chemistry and Physics*, 85th ed., CRC Press, Boca Raton, FL, 2004–2005, pp. 12/219.
7. T. Hüpf: Ph.D. Thesis, Graz University of Technology, Graz, 2010.
8. A. Schmon: Ph.D. Thesis, Graz University of Technology, Graz, 2016.
9. P.G. Klemens and R.K. Williams: *Int. Met. Rev.*, 1986, vol. 31 (5), p. 208.
10. B. Wilthan, W. Schützenhöfer, and G. Pottlacher: *Int. J. Thermophys.*, 2015, vol. 36, pp. 2259–72.
11. K. Aziz, A. Schmon, and G. Pottlacher: *High Temp.-High Press.*, 2014, vol. 43, pp. 193–200.
12. K. Aziz, A. Schmon, and G. Pottlacher: *High Temp.-High Press.*, 2015, vol. 44, pp. 475–81.
13. K. Aziz, A. Schmon, E. Kaschnitz, J. Rattenberger, and G. Pottlacher: *Int. J. Thermophys.*, 2016, vol. 37, p. 15.
14. A. Schmon, K. Aziz, and G. Pottlacher: *Metall. Mater. Trans. A*, 2015, vol. 46A, pp. 2674–79.
15. O. Braaten, A. Kjekshus, and H. Kvande: *JOM*, 2000, vol. 52, pp. 47–53.
16. F. Henning: *Temperaturmessung*, Springer, Berlin, 1977, p. 136.
17. I. Egry, G. Lohöfer, and S. Sauerland: *Int. J. Thermophys.*, 1993, vol. 14, pp. 573–84.
18. J.W.S. Rayleigh: *Proc. R. Soc. Lond.*, 1897, vol. 29, pp. 71–97.
19. D.L. Cummings and D.A. Blackburn: *J. Fluid Mech.*, 1991, vol. 224, pp. 395–416.
20. O. Rozenbaum, D. De Sousa Meneses, Y. Auger, S. Chermanne, and P. Echegut: *Rev. Sci. Instrum.*, 1999, vol. 70 (10).
21. V.A. Petrov and A.Y. Vorobyev: *High Temp.-High Press.*, 2003–2007, vol. 35–36, pp. 677–89.
22. H.L. Peng, T. Voigtmann, G. Kolland, H. Kobatake, and J. Brillo: *Phys. Rev. B*, 2015, vol. 92 (18), p. 184201.
23. J. Schmitz, B. Hallstedt, J. Brillo, I. Egry, and M. Schick: *J. Mater. Sci.*, 2012, vol. 47, pp. 3706–12.
24. M.J. Assael, K. Kakosimos, R.M. Banish, J. Brillo, I. Egry, R. Brooks, P.N. Quested, K.C. Mills, A. Nagashima, Y. Sato, and W.A. Wakeham: *J. Phys. Chem. Ref. Data*, 2006, vol. 35 (1), pp. 285–300.
25. *Recommended Values of Thermophysical Properties for Selected Commercial Alloys*, K.C. Mills, ed., Woodhead Publishing Ltd, Cambridge, United Kingdom, 2002, pp. 19–25.
26. *Recommended Values of the Thermophysical Properties of Eight Alloys, Major Constituents and Their Oxides*, Y.S. Touloukian, ed., Lafayette, IN, 1966, pp. 434–35.
27. *Smithells Metals Reference Book*, 7th ed., E.A. Brandes and G.B. Brook, eds., Butterworth-Heinemann, Oxford, United Kingdom, 1992, pp. 14/7–14/10.
28. W.D. Drotning: *High Temp. Sci.*, 1979, vol. 11, pp. 265–76.
29. G.R. Gathers: *Int. J. Thermophys.*, 1983, vol. 4 (3), pp. 209–26.
30. C.Y. Ho, M.W. Ackerman, K.Y. Wu, T.N. Havill, R.H. Bogaard, R.A. Matula, S.G. Oh, and H.M. James: *J. Phys. Chem. Ref. Data*, 1983, vol. 12 (2), p. 197.
31. R.O. Simmons and R.W. Balluffi: *Phys. Rev.*, 1960, vol. 117 (1), pp. 62–68.
32. R. Brandt and G. Neuer: *Int. J. Thermophys.*, 2007, vol. 28 (5), pp. 1429–46.
33. R.A. McDonald: *J. Chem. Eng. Data*, 1967, vol. 12 (1), pp. 115–18.
34. U. Schmidt, O. Vollmer, and R. Kohlhaas: *Z. Naturforsch.*, 1970, vol. 25a, pp. 1258–64.
35. P.D. Desai: *Int. J. Thermophys.*, 1987, vol. 8 (5), pp. 621–38.
36. D.I. Marchidan and M. Ciopec: *Rev. Roum. Chimie*, 1970, vol. 15, pp. 1005–09.
37. E.H. Buyco and F.E. Davis: *J. Chem. Eng. Data*, 1970, vol. 15 (4), pp. 518–23.
38. D.A. Ditmars, C.A. Plint, and R.C. Shukla: *Int. J. Thermophys.*, 1985, vol. 6 (5), pp. 499–515.
39. *Thermophysical Properties of Matter 1—Thermal Conductivity*, Y.S. Touloukian, R.W. Powell, C.Y. Ho, and P.G. Klemens, eds., Plenum Publishing Corporation, New York, NY, 1970, p. 9.
40. B. Giordanengo, N. Benazzi, J. Vinckel, J.G. Gasser, and L. Roubi: *J. Non-Crystalline Solids*, 1999, vols. 250–252, pp. 377–83.
41. *Thermophysical Properties of Matter 10—Thermal Diffusivity*, Y.S. Touloukian, R.W. Powell, C.Y. Ho, and M.C. Nicolaou, eds., Plenum Publishing Corporation, New York, NY, 1973, p. 2.
42. T. Campbell, R.K. Kalia, A. Nakano, P. Vashishta, S. Ogata, and S. Rodgers: *Phys. Rev. Lett.*, 1999, vol. 82, pp. 4866–69.
43. B.J. Keene: *Int. Mater. Rev.*, 1993, vol. 38, pp. 157–92.
44. J. Brillo and G. Kolland: *J. Mater. Sci.*, 2016, vol. 51, pp. 4888–4901.
45. H. Kobatake, J. Brillo, J. Schmitz, and P. Pichon: *J. Mater. Sci.*, 2015, vol. 50, pp. 3351–60.
46. W. Schröer and G. Pottlacher: *High Temp.-High Press.*, 2013, vol. 43, pp. 201–15.
47. V. Morel, A. Bultel, and B.G. Chéron: *Int. J. Thermophys.*, 2009, vol. 30, pp. 1853–63.
48. S. Blairs and M.H. Abassi: *J. Coll. Interface Sci.*, 2006, vol. 304, pp. 549–53.
49. C. Boissière and G. Fiorese: *Rev. Phys. Appl.*, vol. 12, p. 857.
50. A.A. Likalter: *Phys. A*, 2002, vol. 311, pp. 137–49.
51. H.D. Jones: *Phys. Rev. A*, 1973, vol. 8 (6), pp. 3215–26.
52. Evaluation of Measurement Data—Guide to the Expression of Uncertainty in Measurement, JCGM, 2008.
53. B. Wilthan: Ph.D. Thesis, Graz University of Technology, Graz, 2005, accessible via https://www.tugraz.at/institute/iep/forschung/thermophysics-and-metalphysics/phd-theses/.
54. T. Macher: Master's Thesis, Graz University of Technology, Graz, 2014, accessible via https://www.tugraz.at/institute/iep/forschung/thermophysics-and-metalphysics/master-theses/.

8.2. Density of Liquid Tantalum and Estimation of Critical Point Data

M. Leitner, W. Schröer and G. Pottlacher. "Density of Liquid Tantalum and Estimation of Critical Point Data." In: *Int. J. Thermophys.* 39.11 (2018), p. 124. DOI: https://doi.org/10.1007/s10765-018-2439-3.

SHORT SUMMARY

Density as a function of temperature was measured for tantalum by means of low-pressure ohmic pulse-heating. The critical point was estimated from the obtained liquid-phase density data. All data are extensively compared to those reported in the literature.

REMARKS ON AUTHORSHIP

M. Leitner performed the measurements and wrote the publication.
W. Schröer was involved in the text revision process concerning the application of his proposed algorithm to derive critical point data.
G. Pottlacher supervised the measurement and publication process and was involved in text revisions.

International Journal of Thermophysics (2018) 39:124
https://doi.org/10.1007/s10765-018-2439-3

Density of Liquid Tantalum and Estimation of Critical Point Data

M. Leitner[1] · **W. Schröer**[2] · **G. Pottlacher**[1]

Received: 16 October 2017 / Accepted: 13 August 2018

Abstract

In order to determine the density of tantalum over the entire liquid phase (at the pressure applied) and several hundred K into the super-heated region, the method of ohmic pulse-heating was applied. For this purpose, images of the thermal radial expansion of the resistively heated sample wires were taken with an adapted CCD system. A newly integrated high-power photoflash and improved triggering of the experiment allowed the acquisition of high-contrast shadow images of the expanding wires. To reduce the uncertainty arising from simultaneous pyrometric temperature measurement, the change in normal spectral emissivity as a function of temperature was additionally taken into account. In this work, the density versus temperature relationship of tantalum is reported and compared to existing literature data. From the newly obtained liquid-phase density, critical point data of tantalum, such as critical temperature and critical density, were estimated via an extrapolation procedure. Furthermore, an estimate of the phase diagram in the density versus temperature plane is given. The work is concluded by a rigorous density uncertainty estimation according to the *guide to the expression of uncertainty in measurement* (GUM).

Keywords Critical point data · Liquid-phase density · Phase diagram · Pulse-heating · Tantalum

M. Leitner
matthias.leitner@tugraz.at

W. Schröer
schroer@uni-bremen.de

G. Pottlacher
pottlacher@tugraz.at

1 Institute of Experimental Physics, Graz University of Technology, NAWI Graz, Petersgasse 16, 8010 Graz, Austria

2 Faculty 02: Biology/Chemistry, Universität Bremen, Leobener Str. NW 2, 28334 Bremen, Germany

Published online: 03 September 2018

1 Introduction

Critical point data for high-melting metals are scarce but of fundamental interest. Due to the extremely high temperature and pressure at this point, it cannot easily be reached experimentally for high-melting metals. However, extrapolating the liquid-phase density according to theoretical models allows researchers to estimate the critical point [1]. Even though density data for high-melting metals exist in literature, they often suffer from large uncertainties or are not consistent with each other. The situation is aggravated by the fact that the data often do not reach far beyond the melting point.

In order to obtain the best starting conditions for the extrapolation procedure, two aspects are crucial. First, density data should extend as far as possible into the liquid phase, and second, the data should exhibit smallest possible uncertainties. To meet both requirements, the density of liquid tantalum was re-measured in this work by means of ohmic pulse-heating.

For recent density data of this group, please refer to [2–4]. For previous critical point data estimation on low-melting metals, please refer to, e.g., [5,6].

2 Experimental Procedure and Data Evaluation

Tantalum wires with a diameter of 0.5 mm and a length of 40 mm (Co. Advent, purity: 99.9 wt%, catalogue no.: Ta550615, charge no.: Gi1109, temper annealed) were resistively heated under N_2 atmosphere (2.3 bar) by means of ohmic pulse-heating, starting at room temperature (293 K). The slight overpressure that ensues in the sample chamber inhibits flash arcs between sharp edges of the sample-holder. Before each experiment, the samples were treated with abrasive paper (grade 1200) and subsequently cleaned with acetone.

The energy for the experiment is provided by a 500 μF capacitor bank that can be charged up to 10 kV. Upon triggering the experiment, a current pulse peaking at about 10 kA is discharged over the sample. Due to its ohmic resistance, the wire is heated from room temperature to the liquid phase until it explodes due to the sudden increase in volume at the liquid–gas-phase boundary. Heating rates of the order $10^8\,\mathrm{K}\cdot\mathrm{s}^{-1}$ are reached. As a consequence of the high heating rates applied, the experimental duration is very short, in this case 43 μs. Measurements can thus be performed on the expanding liquid metal column that, due to its inertia, is vertically standing during the experiment. Besides, radiative losses, chemical interactions and evaporation effects are largely inhibited due to the short timescale. Still, the sample remains in thermodynamic equilibrium (private communication Prof. G. Pottlacher with Prof. F. Hensel, Univ. Marburg, Germany, 1986) . For a more in-depth description of the pulse-heating setup, please refer to previous publications from this working group, e.g., [3,7,8].

Investigations in the past have also indicated that high heating rates result in an increased radial wire expansion while inhibiting longitudinal expansion [9,10]. Ohmic pulse-heating can thus be applied to deduce the material's temperature-dependent density by monitoring the thermal radial expansion and, at the same time, record the temperature. In total, data of seven independent experiments were evaluated.

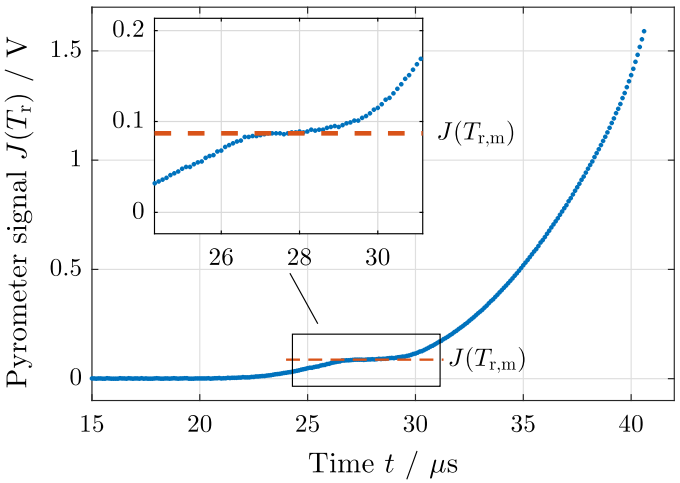

Fig. 1 Radiance-over-time development in a pulse-heating experiment on tantalum. To calculate the calibration constant of the pyrometer, the signal at the melting plateau $J(T_{r,m})$ is assigned to the radiance temperature at melting $T_{r,m}$

2.1 Temperature

In order to deduce the sample temperature, the surface radiance of the sample is monitored pyrometrically as a function of time (sampling rate: 10 MHz). The pyrometer used operates at a mean effective wavelength of $\lambda = 652\,\text{nm}$ with a filter full-width-at-half-maximum of 27 nm.

In order to convert the recorded pyrometer voltage signal to a temperature, each experiment is self-calibrated at the melting plateau, which can be observed in the radiance-over-time development (see Fig. 1). Following Planck's law of radiation, the calibration constant K can be calculated from

$$K = J(T_{r,m}) \cdot \left\{ \exp\left(\frac{c_2}{\lambda \cdot T_{r,m}} \right) - 1 \right\} , \tag{1}$$

where $T_{r,m}$ is the radiance temperature at melting, $J(T_{r,m})$ is the pyrometer signal at the melting plateau, and $c_2 = 14.388\,\mu\text{m K}$ is the second radiation constant. The radiance temperature at the melting point is calculated from the literature value for the true melting temperature ($T_m = 3280\,\text{K}$ [11]) and the normal spectral emissivity of tantalum at the melting point that was reported by Cagran et al. ($\varepsilon_m = 0.366$) [12].

Knowing the calibration constant K, the pyrometer signal $J(T_r)$ is converted into a radiance temperature T_r with

$$T_r = \frac{c_2}{\lambda \cdot \ln\left(\frac{K}{J(T_r)} + 1 \right)} . \tag{2}$$

Finally, the true temperature T above melting is deduced from the radiance temperature T_r, and the liquid-phase normal spectral emissivity $\varepsilon(\lambda, T_r)$, according to

$$T = \frac{c_2}{\lambda \cdot \ln\left\{ \varepsilon(\lambda, T_r) \cdot \left[\exp\left(\frac{c_2}{\lambda \cdot T_r} \right) - 1 \right] + 1 \right\}} , \tag{3}$$

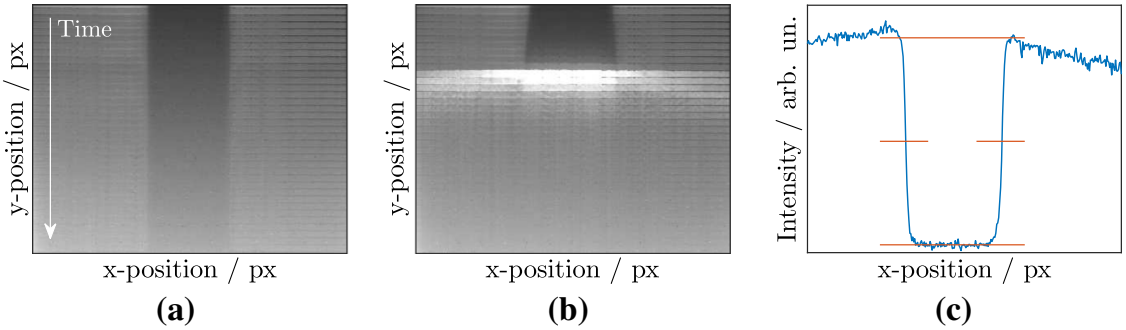

Fig. 2 (a) Image sequence captured prior to the pulse-heating start. (b) Image sequence taken during the pulse-heating experiment. Radial expansion of the wire and the phase explosion can be observed (bright horizontal band). Time and temperature can be assigned to each of the image slices. (c) Exemplary intensity profile of one streak image to deduce a precise diameter (FWHM) for density determination. These profiles are calculated by summation over the lines of the respective images

with the normal spectral emissivity given as

$$\varepsilon(684.5\,\mathrm{nm}, T_\mathrm{r}) = 0.49\,725 - 4.63\,794 \times 10^{-5} \cdot T_\mathrm{r}\,, \tag{4}$$

which is valid in the range $2820\,\mathrm{K} < T_\mathrm{r} < 4400\,\mathrm{K}$ [12].

Note that the normal spectral emissivity was measured at a wavelength of 684.5 nm, whereas the pyrometer operates at a mean effective wavelength of 652 nm. However, due to the feasibility of a gray-body assumption in this narrow wavelength interval, the cited emissivity can be applied to Eq. 3 as stated in (4). It is important to mention that in the given experiment, an assumption of a temperature-independent liquid-phase emissivity for temperature deduction would result in an error of more than $-400\,^\circ\mathrm{C}$ at the highest temperatures measured.

Due to the strong surface treatment dependence of the emittance in the solid phase, see, e.g., [13], it is difficult to find valuable reference data. The temperature in the solid phase was thus calculated under the assumption that the emittance is independent of temperature and takes the value that is true at the melting point.

2.2 Thermal Radial Expansion and Density

The thermal radial expansion of the wire is monitored by an adapted CCD system that is mounted orthogonally to the direction of the pyrometer view. The expanding wire is backlit by the collimated light of a newly integrated high-power photoflash (*Multi-blitz X10*, 1000 Ws). The shadowgraph is imaged with the adapted CCD system that first converts the incident photons into electrons (photocathode), then amplifies the signal (multi-channel-plate) and finally reconverts the electrons into photons (phosphor screen) for subsequent imaging onto a CCD chip (sensor, 384×572 pixel). The sensor is mechanically masked such that only 8 pixel lines are uncovered and thus ready for exposure. The rest of the chip serves as a fast buffer storage unit for the recorded streak images that are shifted into the masked region after acquisition. This way, numerous images can be recorded for each experiment (see Fig. 2a, b), because the time-expensive reading of the chip information can be postponed.

Time synchronization is provided by a common trigger pulse such that all measured quantities share the same time basis. A point in time and, therefore, a temperature can thus be assigned to each of the recorded image slices. Due to the high intensity of the photoflash, the exposure time could be decreased to 300 ns. The setup now takes images about every 2.5 µs, which corresponds to a frame rate of 4×10^5 fps. For more technical details about the CCD system, see, e.g., [10,14].

Figure 2 depicts a typical image sequence that is acquired before the pulse-heating experiment (a) and a sequence that is taken during the experiment (b). Note that the time propagates from top to bottom. By evaluating the full-width-at-half-maximum of the calculated intensity profiles (Fig. 2c) of each streak image, the volume expansion $V(T)/V_0 \equiv (d(T)/d_0)^2$ and from that the density $\rho(T)$ can be calculated via

$$\rho(T) = \rho_0 \cdot \left(\frac{d_0}{d(T)}\right)^2 , \tag{5}$$

where ρ_0 is the room temperature density and d_0 and $d(T)$ are the evaluated diameters obtained from the image sequence. Due to the experimental constraints, the quadratic radial expansion represents the volume expansion as indicated above.

Note that the contrast of the streak images decreases as a function of time (see Fig. 2a). As it takes about 20 µs counted from the initiation of pulse-heating, until the sample's surface radiance is high enough to be detected by the pyrometer, the camera start is timed accordingly to obtain high-contrast streak images with steep edges in the intensity profiles.

To obtain a homogeneous distribution of expansion values with respect to temperature, the camera start is shifted by steps of 0.5 µs between consecutive experiments.

2.3 Critical Point Data

The estimation of critical point data such as critical temperature T_c and critical density ρ_c is based on an extrapolation of the liquid-phase density $\rho(T)$, as proposed by Schröer and Pottlacher [1].

The main idea is to fit the liquid-phase density, indexed by a plus, according to Ising behavior $\rho_+ \propto (T_{c,I} - T)^{1/3}$ and mean field behavior $\rho_+ \propto (T_{c,mf} - T)^{1/2}$, yielding estimates for the critical temperature (fit coefficients) according to the model used. A final estimate for the critical temperature T_c is obtained by taking the arithmetic mean between the two values $T_{c,I}$ and $T_{c,mf}$.

Once this value has been obtained, estimates for the critical density ρ_c are determined in two ways. First, the rule of rectilinear diameter is applied, meaning that $\rho_{diam} = \rho_{c,lin} + a_{lin} \cdot (T_c - T)$ is fitted to the diameter $\frac{(\rho_+ + \rho_-)}{2}$, which can be approximated by $\rho_{diam} = \frac{\rho_+}{2}$ in the measuring region (compare Fig. 4). One of the two fitting parameters yields the critical density $\rho_{c,lin}$. In the second approach, the phase diagram diameter is fitted according to $\rho_{diam} = \rho_{c,2/3} + a_{2/3} \cdot (T_c - T)^{2/3}$, again giving an estimate for the critical density, i.e., $\rho_{c,2/3}$. The average of these two critical densities is taken as final estimate for ρ_c.

The phase diagram is then obtained by fitting the diameter ρ_{diam} according to

$$\rho_{\mathrm{diam}} = \frac{\rho_+}{2} = \rho_{\mathrm{c}} \left(1 + a \cdot (T_{\mathrm{c}} - T) + c \cdot (T_{\mathrm{c}} - T)^{2/3}\right) , \tag{6}$$

yielding the fitting parameters a and c. The liquid-phase density ρ_+ is then fitted following Eq. 7,

$$\rho_{\pm} = \rho_{\mathrm{diam}} \pm b \cdot (T_{\mathrm{c}} - T)^{1/3} \left(1 + b_2 \cdot (T_{\mathrm{c}} - T)^{2/3}\right) , \tag{7}$$

and the parameters b and b_2 are obtained. ρ_- describes the gas phase density.

For Alkali metals, estimates for critical data T_{c} and ρ_{c}, obtained by taking the arithmetic mean between the extrapolated values presuming Ising or mean field behavior, were in good agreement with experimentally determined critical point data [1]. Thus, this approach was applied here too.

3 Results and Discussion

In this section, results are depicted in graphical form and compared to those appearing in the existing literature. Relevant details about the references used for density comparison are listed in Table 1. Note the differences in experimental pressure applied. However, due to the low isothermal compressibility of liquid Ta, $\kappa_{\mathrm{T}} = 0.0168\,\mathrm{GPa}^{-1}$ (at the melting point) [15], pressure-related deviations in density should be less than 0.5 %. The experimentally obtained liquid-phase density values are listed in Table 3. The regression to the data is given in the form of a polynomial (Table 2).

3.1 Density

To derive density data from the measured thermal radial expansion, a room temperature density of $\rho_0 = 16\,654\,\mathrm{kg \cdot m^{-3}}$ was adopted from [20]. The result is depicted in Fig. 3 together with data given in the literature and shows a linear decrease with increasing temperature. A linear regression to the density data in the liquid phase was made. At the beginning of the liquid phase, a density of $\rho(T_{\mathrm{m,l}}) = (15.01 \pm 0.21) \times 10^3\,\mathrm{kg \cdot m^{-3}}$ is obtained by evaluating the fit equation given in Table 2. Based on the boiling temperature of tantalum $T_{\mathrm{b}} = 5731\,\mathrm{K}$ [20], a super-heating of about 670 K is achieved before the wire explodes (Table 3).

The data reported by Gathers [16], Berthault et al. [17] and Jäger et al. [18] were originally given as volume expansions $V(T)/V_0$. In the first two articles, either the specific volume V_0 or the room temperature density was also stated and the density could thus be calculated straightaway. For the data of Jäger et al., the ρ_0 value given above was applied to convert the volume expansion into density.

Paradis et al. [19] measured the density of tantalum in the liquid and supercooled liquid state via an electrostatic levitation technique. The comparison between Paradis's data and the data of this work is thus of particular interest due to the completely different methods applied.

Table 1 Comparison of experimental details of this study and comparable measurements appearing in the literature

	Ref.	Method	Purity/wt%	Pressure/Pa	$\rho(T_{m,l})/10^3$ kg · m^{-3}	Heating rate/K · s^{-1}
This work		Pulse	99.9	2.3×10^5	15.01	$\approx 10^8$
Gathers	[16]	Pulse	n.a.	$(0.1 \text{ to } 0.3) \times 10^9$	14.44	$\approx 10^8$
Berthault	[17]	Pulse	99.98	0.2×10^9	14.58	$\approx 10^8$
Jäger	[18]	Pulse	99.97[a]	0.2×10^9	14.8	$\approx 10^9$
Paradis	[19]	Levi	99.95[a]	10^{-5}	15.00	$\approx -1.7 \times 10^3$

Pulse refers to pulse-heating experiments, *Levi* to levitation experiments. $\rho(T_{m,l})$ is the liquid-phase density at the melting point

[a] It is not stated whether the purity is given in wt% or at.%

Table 2 Fit coefficients for the liquid-phase density of tantalum in the form $\rho(T) = a - b \cdot T$

Equation	a/kg · m^{-3}	b/kg · m^{-3} · K^{-1}	Temperature range
$\rho(T) = a - b \cdot T$	$(17.25 \pm 0.17) \times 10^3$	(0.684 ± 0.034)	$3280 \leq T/\mathrm{K} \leq 6400$

The density uncertainty calculated with the given fit increases from 1.4 % at the beginning of the liquid phase to 2.3 % at the highest temperature. Uncertainties are given with $k = 2$. Note that an additional, insignificant digit is given for the slope b in order to retain the original fitting curve. This curve is used in a second step to estimate critical point data

Table 3 Experimental values of density as a function of temperature $\rho(T)$ for tantalum derived from thermal expansion measurements

T/K	$\rho(T)$/kg · m^{-3}	T/K	$\rho(T)$/kg · m^{-3}	T/K	$\rho(T)$/kg · m^{-3}
2084	16 131	3299	14 941	4715	14 370
2102	16 128	3303	14 972	4765	13 716
2145	16 094	3304	15 132	4855	13 837
2263	15 924	3343	15 010	4877	14 029
2455	15 731	3361	15 028	4978	14 071
2616	15 891	3467	14 850	5090	13 710
2670	15 566	3586	14 805	5286	13 624
2672	15 776	3631	14 520	5289	13 894
2698	15 675	3653	14 743	5406	13 248
2855	15 659	3663	14 601	5490	13 352
2912	15 670	3804	14 666	5521	13 598
3035	15 495	3864	14 420	5589	13 473
3127	15 512	4045	14 509	5734	13 286
3166	15 273	4143	14 495	5856	13 149
3168	15 416	4174	14 221	5938	13 459
3175	15 326	4244	14 241	6095	12 932
3259	15 344	4252	14 351	6186	13 051
3273	15 424	4382	14 427	6217	12 907
3281	15 274	4466	14 108	6349	12 755
3290	15 111	4658	14 341	6400	12 944

The density values were obtained with a room temperature density of $\rho_0 = 16\,654\,\mathrm{kg \cdot m^{-3}}$. Combined expanded temperature uncertainty for the liquid phase ($T > 3280\,\mathrm{K}$), $U_\mathrm{c}(T)/T = 0.017$ at the beginning of the liquid phase up to $U_\mathrm{c}(T)/T = 0.028$ at the highest temperature measured. Combined expanded density uncertainty $U_\mathrm{c}(\rho)/\rho = 0.013$. Uncertainties reported with a level of confidence 0.95 ($k = 2$)

As can be seen in Fig. 3, the newly measured density data are in excellent agreement with the data found by Paradis et al. At the melting point, Paradis et al. reported $\rho(T_\mathrm{m}) = 15.0 \times 10^3\,\mathrm{kg \cdot m^{-3}}$ which corresponds to a deviation of only $-0.07\,\%$ with respect to the value derived in this work. The uncertainty is stated with $< 2\,\%$. To deduce the temperature, they assumed a constant emissivity behavior in the liquid phase. Also note the difference of ten orders of magnitude in the experimental pressure

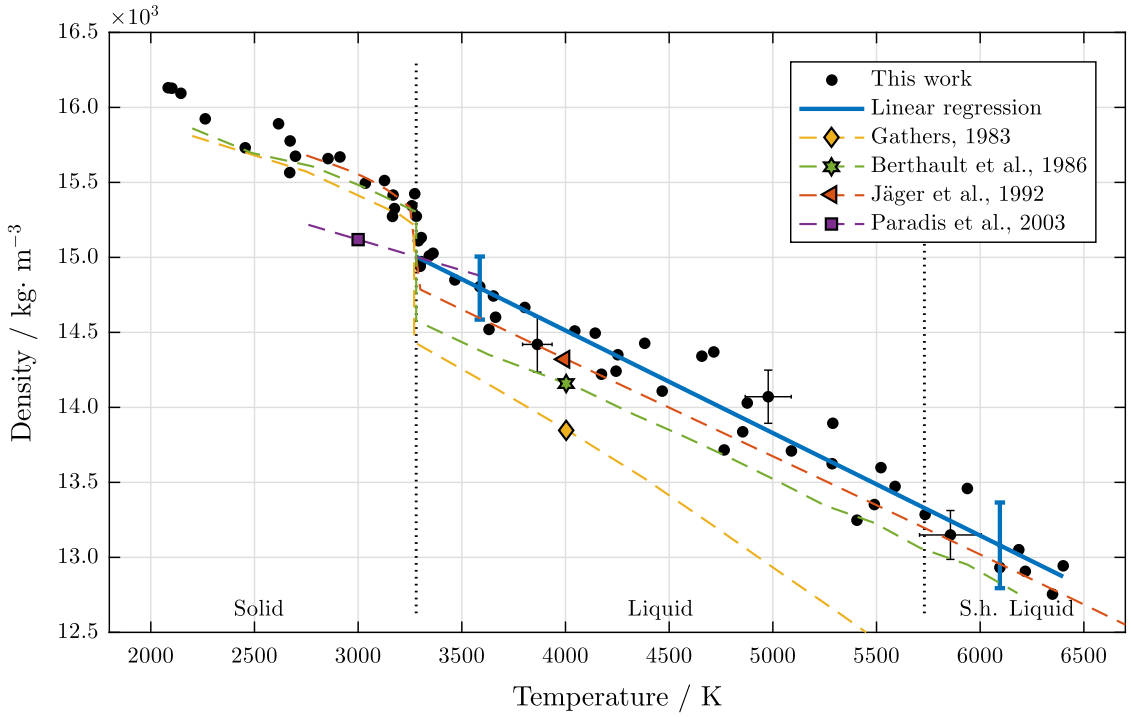

Fig. 3 Density of tantalum as a function of temperature. The vertical dotted lines delineate the melting and boiling temperatures. Above the boiling point, the sample is in a super-heated (S.h.) liquid state. Full circles and solid line: experimental data obtained during this work and corresponding liquid-phase linear regression. Gathers [16]: dashed line with diamond, Berthault et al. [17]: dashed line with star, Jäger et al. [18]: dashed line with triangle, Paradis et al. [19]: dashed line with square, measurements in the liquid and undercooled liquid state

applied and the difference between a heating rate of $10^8\,\mathrm{K}\cdot\mathrm{s}^{-1}$ in our experiments as compared to a cooling rate of about $-1.7\times10^3\,\mathrm{K}\cdot\mathrm{s}^{-1}$ achieved by Paradis et al.

The data obtained in the present study are also in very close agreement with the data reported earlier by our group (Jäger et al. [18]) as well as the data published by Berthault et al. From the data of Jäger et al., a density at the beginning of melting of $\rho(T_{\mathrm{m,l}}) = 14.8\times10^3\,\mathrm{kg}\cdot\mathrm{m}^{-3}$ can be derived. This corresponds to a deviation of only $-1.4\,\%$ with respect to our data. This is remarkable, since they used different wire diameters (0.25 mm), a heating rate that is higher by one order of magnitude (about $10^9\,\mathrm{K}\cdot\mathrm{s}^{-1}$), and took photographs of the expanding wire with a Kerr-cell camera, which can only take one picture per experiment (30 ns exposure time). Also note that these experiments were performed at a pressure that is three orders of magnitude higher than in our experiments. A constant emissivity in the liquid phase was assumed in the temperature deduction. Jäger et al. state an uncertainty of 8 % for volume expansion. However, as the coverage factor is not reported in the original publication, it is not converted into a density uncertainty here. The same is true for the data given by Berthault et al.; they state an uncertainty of 2 % for volume expansion. The data given by Berthault et al. are even lower, $\rho(T_{\mathrm{m,l}}) = 14.58\times10^3\,\mathrm{kg}\cdot\mathrm{m}^{-3}$ ($-2.9\,\%$), but still in reasonable agreement with our data. It was also assumed that the emissivity does not change in the liquid phase. These experiments were performed under a pressure of 0.2 GPa.

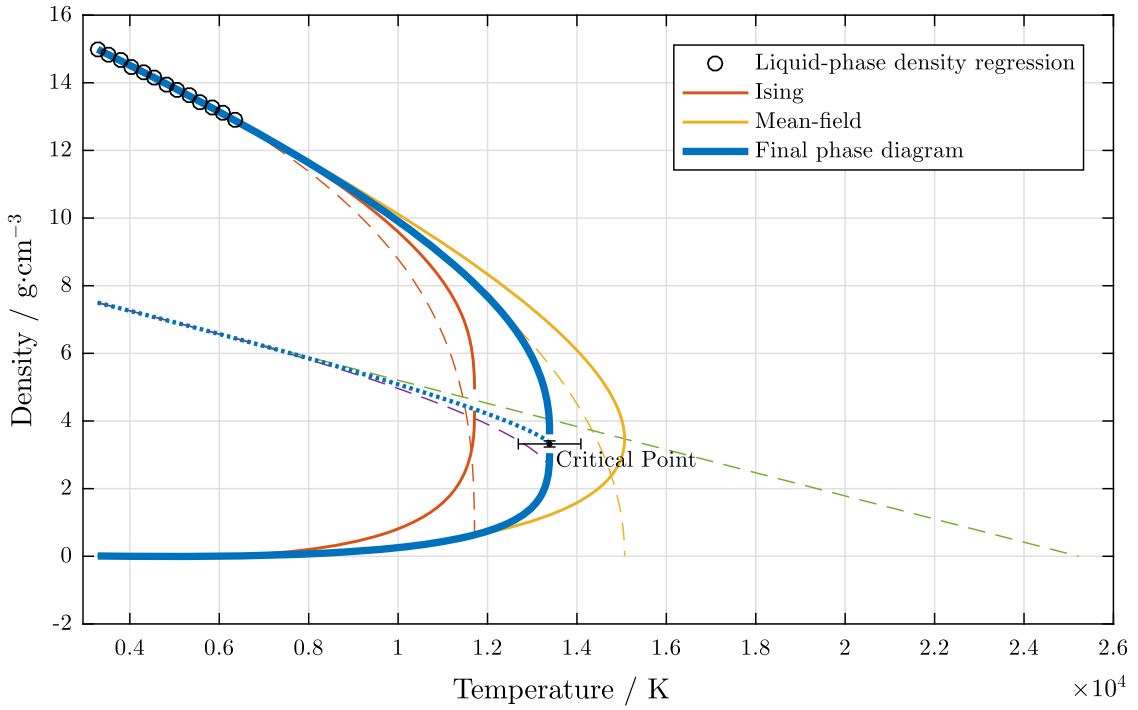

Fig. 4 Estimated phase diagram (thick solid line) with nonlinear diameter ρ_{diam} (dotted line) and critical point of tantalum. Open circles: Data generated by the linear regression of this work's experimental density data. Dashed lines: Extrapolation of the density data (fifty data points) according to mean field and Ising behavior as well as linear and nonlinear extrapolation of the phase diagram diameter. Thin solid lines: Phase diagrams according to mean field and Ising behavior

The high-pressure data measured by Shaner et al. [21] and later corrected by Gathers are about 3.8 % lower at the beginning of the liquid phase ($\rho(T_{\mathrm{m,l}}) = 14.44 \times 10^3\,\mathrm{kg \cdot m^{-3}}$). The discrepancy further increases at higher temperatures due to the difference in slope. Gathers estimated the emissivity from the pyrometer signal via a numerical procedure. No uncertainty is given.

3.2 Critical Point Data

The critical point in the (ρ, T)-plane was estimated according to the proposal of Schröer and Pottlacher [1] as briefly outlined in Sect. 2.3. Figure 4 shows density data points far away from the critical point that are used for the extrapolation (data calculated from the linear regression, Table 2). Fifty data points are fitted according to mean field and Ising theory (dashed lines). The straight dashed line shows the phase diagram diameter fit according to the rule of rectilinear diameter. Once these data have been obtained, the phase diagram according to the Ising model and to mean field theory can be plotted (thin solid lines). As outlined in Sect. 4.2, the phase diagram diameter is also fitted in a nonlinear manner (curved dashed line).

The final estimate of the phase diagram is depicted as a thick solid line, described by Eq. 7. The dotted line shows the nonlinear diameter of the estimated phase diagram according to Eq. 6. The fit coefficients needed to describe the phase diagram are listed in Table 4. Uncertainty bars show the range of variation of the critical point due to the uncertainty of the density-fit parameters, see Sect. 4.2.

Table 4 Parameters of the estimated phase diagram of tantalum according to Eqs. 6 and 7

$a/10^{-5}\mathrm{K}^{-1}$	$c/10^{-3}\mathrm{K}^{-2/3}$	$b/10^{-1}\mathrm{K}^{-1/3}$	$b_2/10^{-4}\mathrm{K}^{-2/3}$
5.16	1.57	2.98	3.48

For the critical temperature T_c and the critical density ρ_c, we obtain

$$T_c = (13.4 \pm 0.7) \times 10^3\,\mathrm{K}$$
$$\rho_c = (3.32 \pm 0.09)\,\mathrm{g \cdot cm^{-3}}$$

Critical temperatures estimated in the literature range from $T_c = 8865\,\mathrm{K}$ [22] to values as high as $T_c = 22\,000\,\mathrm{K}$ [23] depending on the method and input data used. For a detailed listing of several theoretically predicted T_c values, we would like to refer the reader to the publication of Blairs and Abbasi [24] and the references therein.

A rather recent work by Blairs and Abbasi [25] should also be mentioned in this context. Critical temperatures for metals, obtained via two different methods, are reported by these authors and compared to selected literature values. For tantalum, they obtain $T_c = 13\,284\,\mathrm{K}$ and $T_c = 14\,238\,\mathrm{K}$ in their study. Both of these values are in excellent agreement with the result of this study.

Fortov et al. [26] report $T_c = 13\,380\,\mathrm{K}$, $\rho_c = 3.83\,\mathrm{g \cdot cm^{-3}}$, which is in very good agreement with our data. In addition, they report a critical pressure of $p_c = 0.707\,\mathrm{GPa}$. In their publication, a phase diagram can be found together with other (T_c, ρ_c)-values. In general, a downward trend of the reported critical temperatures can be observed over the years. Older reported values peak between 20 000 K and 22 000 K, while more recent values peak in the range between 12 000 K and 14 000 K. For the critical density, values reported in the literature range between $\rho_c = 1.9\,\mathrm{g \cdot cm^{-3}}$ [22] and $\rho_c = 6.72\,\mathrm{g \cdot cm^{-3}}$ [27].

4 Uncertainties

This section deals with uncertainty estimation according to the *Guide to the expression of uncertainty in measurement*, shortly referred to as GUM [28].

4.1 Density

The data point error bars depicted in Fig. 3 were calculated from the respective functional relationships according to the GUM principle and are given with a coverage factor of $k = 2$. The uncertainties of the diameters were estimated by repeated image evaluation. This results in a standard deviation of up to $u(d_0) = 0.08$ pixel for cold images and up to $u(d(T)) = 0.15$ pixel for hot images, respectively. These maximum observed values were doubled to account for possible systematic effects and taken as worst case estimate for diameter uncertainty, independent of time. The temperature uncertainty was calculated as discussed in [29].

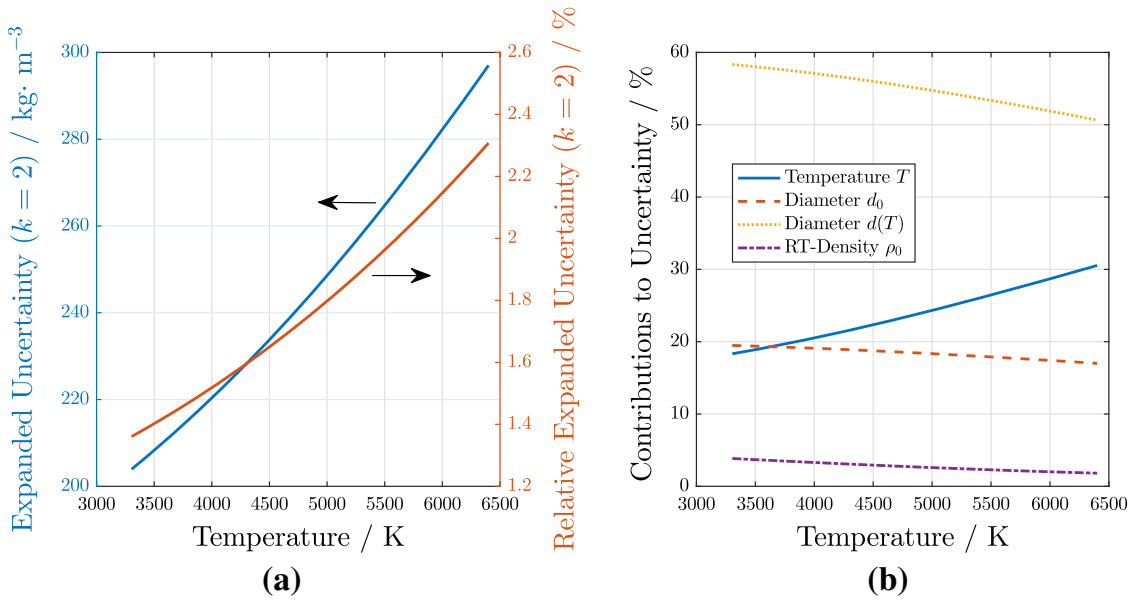

Fig. 5 Uncertainty of liquid-phase density-fit estimated according to GUM. (a) Expanded uncertainty and relative expanded uncertainty ($k = 2$) as a function of temperature. (b) Uncertainty budget as a function of temperature

In a second step, the uncertainties of the intercept a and the slope b of the linear density regression were calculated according to GUM, see [30], by including the individual x- and y-uncertainties of the data points. The room temperature density uncertainty was adopted from [31], $u(\rho_0) = 20\,\mathrm{kg \cdot m^{-3}}$, and was combined with the uncertainty of the intercept after completing the evaluation described above.

Finally, the uncertainty of the fit at any fixed temperature T was calculated according to GUM by employing the uncertainties of the fit coefficients and the temperature uncertainty to the fit equation. The absolute and relative expanded fit uncertainty ($k = 2$) thus obtained is depicted as a function of temperature in Fig. 5a. In addition, the percentual contributions of temperature T, room temperature diameter d_0, temperature-dependent diameter $d(T)$ and room temperature density ρ_0 to this uncertainty are shown in Fig. 5b. As can be seen, the temperature-dependent diameter $d(T)$ accounts for more than one half of the uncertainty over the entire liquid measuring range.

4.2 Critical Point Data

The uncertainty of the critical point (T_c, ρ_c) was estimated from the GUM conform uncertainties of the intercept a and the slope b, $b > 0$, in the liquid-phase density regression. The critical point was calculated for the pairs (a, b), $(a + u(a), b - u(b))$ and $(a - u(a), b + u(b))$, where $u(x)$ denote the uncertainties of x with $k = 1$. The uncertainties of the critical point are then given as the doubled ($k = 2$) standard deviation of the mean value calculated from the three evaluations. Note that this reported uncertainty thus only represents the uncertainty range that originates from the uncertainty of the density regression coefficients.

5 Conclusion

The density of tantalum was re-measured as a function of temperature over the liquid phase and into the super-heated region. The change in normal spectral emissivity over the measuring range was taken into account in order to minimize the uncertainty due to temperature measurement. The experimental data agree very well with previously published results and exhibit uncertainties of less than 2.3 %.

From the liquid-phase density behavior, the critical temperature and critical density were estimated and compared with theoretical results reported in the literature. The concordance is remarkably good.

Acknowledgements Open access funding provided by Graz University of Technology.

References

1. W. Schröer, G. Pottlacher, High Temp. High Press. **43**, 201 (2014)
2. M. Leitner, T. Leitner, A. Schmon, K. Aziz, G. Pottlacher, Metall. Mater. Trans. A **48**, 3036 (2017)
3. A. Schmon, K. Aziz, M. Luckabauer, G. Pottlacher, Int. J. Thermophys. **36**, 1618 (2015)
4. A. Schmon, K. Aziz, G. Pottlacher, Metall. Mater. Trans. A **46**, 2674 (2015)
5. K. Boboridis, G. Pottlacher, H. Jäger, Int. J. Thermophys. **20**, 1289 (1999)
6. E. Kaschnitz, G. Pottlacher, High pressure-high temperaturethermophysical measurements on liquid metals (Teubner, 1992). Teubner-Texte zur Physik **26**, 139–144 (1992)
7. C. Cagran, T. Hüpf, B. Wilthan, G. Pottlacher, High Temp. High Press. **37**, 205 (2008)
8. E. Kaschnitz, G. Pottlacher, H. Jäger, Int. J. Thermophys. **13**, 699 (1992)
9. T. Hüpf, *Density Determination of Liquid Metals*. Ph.D. thesis, Graz, University of Technology (2010)
10. A. Schmon, *Density Determination of Liquid Metals by Means of Containerless Techniques*. Ph.D. thesis, Graz University of Technology (2016)
11. R. Bedford, G. Bonnier, H. Maas, F. Pavese, Metrologia **33**, 133 (1996)
12. C. Cagran, C. Brunner, A. Seifter, G. Pottlacher, High Temp. High Press. **34**, 669 (2002)
13. G. Pottlacher, A. Seifter, Int. J. Thermophys. **23**, 1267 (2002)
14. G. Pottlacher, T. Hüpf, *Thermal Conductivity 30/Thermal Expansion 18* (DEStech Publications, Inc., Lancaster, 2010), pp. 192–206
15. Y. Marcus, J. Chem. Thermodyn. **109**, 11 (2016)
16. G.R. Gathers, Int. J. Thermophys. **4**, 149 (1983)
17. A. Berthault, L. Arles, J. Matricon, Int. J. Thermophys. **7**, 167 (1986)
18. H. Jäger, W. Neff, G. Pottlacher, Int. J. Thermophys. **13**, 83 (1992)
19. P.F. Paradis, T. Ishikawa, S. Yoda, Appl. Phys. Lett. **83**, 4047 (2003)
20. D.R. Lide (ed.), *CRC Handbook of Chemistry and Physics*, vol. 85 (CRC Press, Boca Raton, 2004)
21. J.W. Shaner, G.R. Gathers, C. Minichino, High Temp. High Press. **9**, 331 (1977)
22. A. Likalter, Phys. A **311**, 137 (2002)
23. A. Grosse, J. Inorg. Nucl. Chem. **22**, 23 (1961)
24. S. Blairs, M.H. Abbasi, Acta Acust. Acust. **79**, 64 (1993)
25. S. Blairs, M.H. Abbasi, J. Colloid Interface Sci. **304**, 549 (2006)
26. V. Fortov, K. Khishchenko, P. Levashov, I. Lomonosov, Nucl. Instrum. Methods Phys. Res. Sect. A **415**, 604 (1998)
27. H. Hess, H. Schneidenbach, Z. Metallkd. **87**, 979 (1996)

28. W.G. of the Joint Committee for Guides in Metrology (JCGM/WG 1). Evaluation of measurement data-guide to the expression of uncertainty in measurement (JCGM-Joint Committee for Guides in Metrology) (2008)
29. B. Wilthan, Verhalten des Emissionsgrades und thermophysikalische Daten von Legierungen bis in die flüssige Phase mit einer Unsicherheitsanalyse aller Messgrößen. Ph.D. thesis, Graz, University of Technology (2005)
30. M. Matus, Tech. Mess. **72**, 584 (2005)
31. L.C. Ming, M.H. Manghnani, J. Appl. Phys. **49**, 208 (1978)

8.3. Density of Liquid Niobium and Tungsten and the Estimation of Critical Point Data

M. Leitner and G. Pottlacher. "Density of Liquid Niobium and Tungsten and the Estimation of Critical Point Data." In: *Metall. Mater Trans. A* 50.8 (2019), pp. 3646-3653. DOI: https://doi.org/10.1007/s11661-019-05262-5.

SHORT SUMMARY

Density as a function of temperature was measured for niobium and tungsten by means of low-pressure ohmic pulse-heating. The critical point was estimated from the obtained liquid-phase density data. All data are extensively compared to those reported in the literature.

REMARKS ON AUTHORSHIP

M. Leitner performed the measurements and wrote the publication.
G. Pottlacher supervised the measurement and publication process and was involved in text revisions.

Density of Liquid Niobium and Tungsten and the Estimation of Critical Point Data

M. LEITNER and G. POTTLACHER

Density as a function of temperature was measured for the liquid transition metals niobium and tungsten by means of ohmic pulse-heating. The generated data are extensively compared to the existing literature data, and the uncertainty is critically assessed according to the *guide to the expression of uncertainty in measurement* (GUM). Starting from the obtained liquid-phase density regression, the phase diagram, and the critical point, *i.e.*, critical temperature T_c and critical density ρ_c of niobium and tungsten are estimated. The so-obtained critical point for these two high-melting metals is compared to the data available in the existing literature.

https://doi.org/10.1007/s11661-019-05262-5

I. INTRODUCTION

THE knowledge of a metal's density as a function of temperature is frequently crucial for many scientific considerations and technological applications. It is used as an input parameter in simulations that model thermal natural convection phenomena in furnaces and ladles, to calculate mass balance in refining operations or understand and model solidification processes, to name a few.[1,2] Density as a function of temperature is also needed for the calculation of thermal conductivity from thermal diffusivity and vice versa, or in the measurement of surface tension and viscosity. In fact, various models show a relatively strong sensitivity on input density data compared to other input-properties.[3] Density data of liquid transition metals, however, are often either scarcely available or are very inconsistent with each other. This is also a consequence of the high temperatures that are involved when dealing with liquid metals. These temperatures are typically above several thousand K for transition metals, which leads to a number of technical challenges. It is for this reason that a complementary revisit on liquid density data appears to be appropriate for several transition metals, such as niobium and tungsten.

The density of liquid metals is not only of direct technology-related interest, but also of fundamental scientific interest. Measuring a material's density as a function of temperature means that a part of this material's phase diagram is mapped in the temperature–density projection. Extending the measured density to higher temperatures leads the way to the material's critical point. For high melting metals, this unique point can be at extremely high temperatures well above 10,000 K and at extreme pressures of several hundred MPa. For this reason, the critical point of these metals can be reached experimentally only with great effort, if at all. However, measuring the liquid density at lower temperatures, *e.g.*, *via* ohmic pulse-heating, still allows extrapolating of the measured data points according to simplified theoretical models.[4] By this means one can give an estimation of the critical density, critical temperature and the material's phase diagram in the temperature–density projection. Critical point data of high-melting metals might even be useful one day in future ultra-high temperature technologies, such as for aerospace and energy applications.

This paper is organized as follows: Section II provides details on the experimental procedure and the ohmic pulse-heating setup is briefly explained. Section III presents and discusses the obtained temperature–resolved density data and gives the estimated phase diagrams of niobium and tungsten together with their critical point. In Section IV, uncertainties of the presented data are assessed.

II. EXPERIMENTAL PROCEDURE AND DATA EVALUATION

Wire-shaped W and Nb specimens with a diameter of 0.5 mm and a length of 40 mm were investigated using an ohmic pulse-heating apparatus (OPA) as described in Reference 5. Before the experiments, the specimens (niobium: Co. Advent, purity: 99.9 wt pct, catalog no.: NB537115, Gi1592, condition: temper annealed.

M. LEITNER and G. POTTLACHER are with the Institute of Experimental Physics, Graz University of Technology, NAWI Graz, Petersgasse 16, 8010 Graz, Austria. Contact e-mail: matthias.leitner@tugraz.at

Manuscript submitted November 30, 2018.
Article published online May 20, 2019

Tungsten: Co. Goodfellow, purity: 99.95 wt pct, catalog no.: W 005160/18, LS73129 J F, condition: clean) were treated with abrasive paper (grade 1200) and cleaned with acetone. Subsequently, the wire-samples were subjected to a strong current pulse. Within 45 μs (Nb) and 53 μs (W), the wires are thus heated from room temperature into the liquid phase until boiling sets in and the wire explodes.

During the experiment, the temperature and thermal expansion are recorded, as described in the following sections. The sample (surface) radiance is monitored by means of pyrometry to account for the short timescales. Simultaneously, a fast CCD-camera acquires images of the expanding wire at specific instants in time that can subsequently be related to a corresponding temperature. The experiments were conducted under an inert N_2 atmosphere with a slight static overpressure of about 1.5 bar.

A. *Temperature*

The surface radiance of the sample is monitored throughout the experiment by using a pyrometer with a central wavelength of $\lambda = 650\,\text{nm}$ and a full-width-at-half-maximum of 27 nm. Data points are collected every 100 ns. Neutral density filters were employed to break down the pyrometer signal by a constant fraction and thus enlarge the measurable temperature region. After concluding the experiment, the known radiance temperature at melting is assigned to the visible inflection in the thermogram, *i.e.*, the melting plateau, to derive a radiance temperature $T_r(t)$ as a function of time t. The radiance temperature at melting is for this purpose calculated using the literature value for the true melting temperature T_m and the normal spectral emissivity at melting ε_m. Together with the temperature-dependent normal spectral emissivity $\varepsilon(\lambda, T_r)$ of the metal, the pyrometer signal is then converted into a true temperature $T(t)$ following Eq. [1]:

$$T(t) = \frac{c_2}{\lambda \cdot \ln\left\{\varepsilon(\lambda, T_r) \cdot \left[\exp\left(\frac{c_2}{\lambda \cdot T_r(t)}\right) - 1\right] + 1\right\}}, \qquad [1]$$

where c_2 is the second radiation constant. Table I sums up the utilized values and parameters to derive the true temperature $T(t)$ for tungsten and niobium. For a more detailed description of the temperature deduction as well as an exemplary thermogram, please refer to a previous publication.[6]

B. *Thermal Radial Expansion and Density*

Thermal radial expansion is investigated by means of fast shadow-imaging. During the experiment, a high-power photoflash (*Multiblitz* X10, 1000 Ws) provides intense background illumination to produce shadow images of the expanding wire at specific instants in time. These instants are time-synchronized with the pulse-heating experiment. By this means, a temperature can be assigned to each shadow image taken. The CCD-camera system (Co. PCO imaging with controller unit by Co. Theta System and Graz Univ. of Technol.) is capable of acquiring one image every 2.5 μs, compare *e.g.*, References 6 and 7. After the experiment, summing over the pixel lines of each image gives a cup-shaped intensity profile. The full-width-at-half-maximum of these intensity profiles obtained by this means corresponds to the diameter d of the wire at a specific time and thus temperature T. In relating this temperature-dependent diameter $d(T)$ to the diameter at room temperature d_0, density can be derived by using the literature value for the room-temperature density ρ_0. Note that longitudinal expansion of the wire is inhibited thanks to the short timescales of the experiment. Thus, the measured relative radial expansion squared $(d(T)/d_0)^2$ equals the relative volume expansion $V(T)/V_0$ of the sample. The density as a function of temperature $\rho(T)$ can thus be calculated *via*

$$\rho(T) = \rho_0 \cdot \left(\frac{d_0}{d(T)}\right)^2. \qquad [2]$$

For niobium, we used a room-temperature density of $8.57 \times 10^3\,\text{kg m}^{-3}$ as given in the *CRC Handbook of Chemistry and Physics*.[8] For tungsten, a room-temperature density ρ_0 of $19256\,\text{kg m}^{-3}$ was adopted from Ming and Manghnani,[9] found in the *NIST Alloy data web application*.[10] Note that this density value is only 0.2 pct lower than that given in the *CRC Handbook of Chemistry and Physics*.[8]

C. *Critical Point Data*

The measured liquid-phase density as a function of temperature was taken to estimate the critical temperature T_c, critical density ρ_c , as well as the phase diagram in the (ρ,T)-plane. The estimation is done by an extrapolation algorithm following the method in the publication of Schröer and Pottlacher.[4] In this approach, the measured liquid-phase density is extrapolated according to simplified Ising- and mean-field behavior to estimate critical temperature and critical density.

Table I. Utilized Data for Temperature Deduction of the Metals Niobium and Tungsten

Metal	$\varepsilon(684.5\,\text{nm}, T_r)/1$	Validity Range	Melting Temperature T_m
Niobium	0.345	$2422 < T_r/\text{K} < 3700$	2745 K (2472 °C)
Tungsten	$0.4407 - 1.3916 \times 10^{-5}\,T_r$	$3207 < T_r/\text{K} < 4400$	3687 K (3414 °C)

Normal spectral emissivity ε at a wavelength of 684.5 nm as a function of radiance temperature T_r in K taken from Cagran *et al.*[33] Melting temperature T_m adopted from Bedford *et al.*[34]

A simplified phase diagram, given by the Eqs. [3] and [4], is then also constructed from the measured liquid-phase density $\rho_{+,\mathrm{meas}}(T)$ by extrapolating up to the critical temperature according to Eq. [3],

$$\rho_{\pm}(T) = \rho_{\mathrm{diam}} \pm b \cdot (T_c - T)^{1/3}\left(1 + b_2 \cdot (T_c - T)^{2/3}\right) . \quad [3]$$

In this equation, the subscript '+' indicates the saturated liquid line and '−' indicates the saturated vapor line of the phase diagram—the equation describes how the density changes as a function of temperature up to the critical point. ρ_{diam} is the so-called phase-diagram diameter, *i.e.*, the mean value between the saturated liquid density and the saturated vapor density at a given isotherm, $(\rho_+ + \rho_-)/2$. It is extrapolated up to the critical temperature T_c according to Eq. [4], where ρ_{diam} itself can be calculated from the measured liquid-phase density $\rho_{+,\mathrm{meas}}(T)$ that is located in the low-temperature branch of the binodal, *i.e.*, $\rho_{\mathrm{diam}} \approx \rho_{+,\mathrm{meas}}/2$,

$$\rho_{\mathrm{diam}}(T) = \rho_c\left(1 + a \cdot (T_c - T) + c \cdot (T_c - T)^{2/3}\right) . \quad [4]$$

The extrapolations described above yield the fitting coefficients b, b_2, a and c. For a more detailed description of the formalism, please refer to the original publication[4] or to a previous publication.[6]

Note, that this algorithm delivered remarkably good results when compared to experimentally obtained critical point data of the alkalis.[4] In addition, this approach was tested on the transition metal tantalum, which also delivered good concordance compared to the literature, see Reference 6.

III. RESULTS AND DISCUSSION

In this section, density as a function of temperature for the two metals niobium and tungsten is reported and discussed. From these data, the critical point as well as the phase diagram of the two metals are estimated.

A. *Density*

The measured liquid density of niobium and tungsten are plotted and compared to experimental data given in the literature. The liquid-phase density regressions are tabulated in Table II. The experimentally obtained data points are listed in Tables III (niobium) and IV (tungsten).

1. *Niobium*

Nine independent experiments were performed with niobium. The derived density is shown in Figure 1 together with literature values. At the beginning of the liquid phase, we obtain a density value of $\rho(T_{\mathrm{m,l}}) = (7.69 \pm 0.09) \times 10^3\,\mathrm{kg\,m^{-3}}$, where the subscript 'l' indicates the liquid phase. This is in excellent agreement with the literature, but at a slightly lower value. Ishikawa *et al.*[11] report a value that is 0.5 pct higher, Gallob *et al.*[12] are higher by 0.7 pct, Hixson and Winkler by 0.4 pct,[13] Shaner *et al.* by approximately 1 pct.[14] Interestingly, the change of density with temperature shows significant inconsistency within the literature. While Paradis *et al.* are closest with an about 28 pct stronger density gradient, the deviation of the slope reported earlier by our group[12] is about 189 pct. However, the technique used then was a very simplistic shadowgraph method[7] which also delivered a seemingly higher thermal expansion with other metals.[15]

2. *Tungsten*

Figure 2 shows the density of tungsten as a function of temperature, derived from eight independent pulse-heating experiments. At melting, the density drops by approximately 5 pct to a value of $\rho(T_{\mathrm{m,l}}) = (17.2 \pm 0.5) \times 10^3\,\mathrm{kg\,m^{-3}}$.

The data given in the literature appear to cluster into lower and higher density data. Allen[16] and Calverley[17] report a density at the beginning of melting, $\rho_{\mathrm{m,l}}$, that is 1.9 and 2.4 pct higher than our value. The value given in the *CRC Handbook of Chemistry and Physics*[8] is also 2.4 pct higher than our value. Datapoints reported by Koval *et al.*[18] as well as Hess *et al.*[19] show very good agreement, both at the end of the solid phase and during the liquid phase. In particular, the data given by Koval *et al.* are in extraordinary agreement, while the data points given by Hess *et al.* start to deviate from our data at higher temperatures in the liquid phase. Data given by Paradis *et al.*[2] also agree reasonably well with our data. At the melting point, they deviate by 2.8 pct. For the sake of comparison, the density measured by Paradis *et al.* of an undercooled liquid W-droplet was extrapolated into the liquid phase.

The second set of data found in the literature (Seydel and Kitzel,[20] Berthault *et al.*,[21] Hixson and Winkler[22] as well as Hüpf *et al.*[23]) is significantly lower. At the beginning of the liquid phase, those authors report values that are between 4 pct (Hixson and Winkler) and 5.7 pct (Berthault *et al.*) lower than our value for $\rho(T_{\mathrm{m,l}})$. Interestingly, the density data in the solid phase also show a somewhat unusual broad variation.

Table II. Fit-Coefficients for the Liquid-Phase Density of Niobium and Tungsten in the Form $\rho(T) = a - b \cdot T$. Uncertainty reported with a level of confidence 0.95 ($k = 2$)

Metal	$a/\mathrm{kg\,m^{-3}}$	$b/\mathrm{kg\,m^{-3}\,K^{-1}}$	Temperature Range	$U(\rho)/\rho$
Niobium	$(8.52 \pm 0.09) \times 10^3$	(0.304 ± 0.019)	$2745 \le T/\mathrm{K} \le 5847$	0.013 to 0.022
Tungsten	$(19.8 \pm 0.4) \times 10^3$	(0.71 ± 0.08)	$3687 \le T/\mathrm{K} \le 5631$	0.028 to 0.038

The relative density-uncertainty $U(\rho)/\rho$ at a fixed temperature T is given from the beginning of the liquid phase up to the highest temperature measured.

Table III. Niobium: Experimental Values of Density as a Function of Temperature $\rho(T)$ Derived from Thermal Expansion Measurements

T/K	T/°C	$\rho(T)$/kg m^{-3}	T/K	T/°C	$\rho(T)$/kg m^{-3}	T/K	T/°C	$\rho(T)$/kg m^{-3}
1983	1710	8307	2747	2474	7766	3589	3316	7465
2006	1733	8159	2750	2477	7788	3620	3347	7374
2057	1784	8252	2751	2478	7884	3670	3397	7363
2151	1878	8103	2764	2491	7635	3702	3429	7331
2175	1902	8202	2771	2498	7704	3931	3658	7428
2232	1959	8199	2774	2501	7677	3948	3675	7355
2300	2027	8175	2792	2519	7747	3957	3684	7358
2368	2095	8052	2870	2597	7766	4027	3754	7406
2417	2144	8154	2871	2598	7625	4068	3795	7301
2460	2187	7897	2911	2638	7609	4086	3813	7257
2475	2202	7995	3015	2742	7482	4120	3847	7248
2607	2334	8011	3024	2751	7649	4132	3859	7270
2618	2345	7965	3107	2834	7590	4199	3926	7342
2639	2366	7905	3135	2862	7471	4447	4174	7288
2705	2432	8048	3156	2883	7586	4453	4180	7180
2719	2446	7769	3160	2887	7439	4462	4189	7210
2726	2453	7858	3279	3006	7412	4687	4414	6993
2732	2459	7867	3400	3127	7530	4742	4469	7186
2736	2463	7809	3435	3162	7422	4997	4724	6937
2740	2467	7925	3462	3189	7530	5005	4732	7096
2741	2468	7873	3582	3309	7367	5797	5524	6664
2747	2474	7889	3584	3311	7560	5848	5575	6672

The density values were obtained with a room-temperature density of $\rho_0 = 8570\,\mathrm{kg\,m^{-3}}$.[8]

Combined expanded temperature uncertainty for the liquid phase [$T > 2745$ K (2472 °C)]: $U_c(T)/T = 0.015$ at the beginning of the liquid phase up to $U_c(T)/T = 0.026$ at the highest temperature measured. Combined expanded density–uncertainty $U_c(\rho)/\rho = 0.013$. Uncertainties reported with a level of confidence 0.95 ($k = 2$).

Table IV. Tungsten: Experimental Values of Density as a Function of Temperature $\rho(T)$ Derived from Thermal Expansion Measurements

T/K	T/°C	$\rho(T)$/kg m^{-3}	T/K	T/°C	$\rho(T)$/kg m^{-3}	T/K	T/°C	$\rho(T)$/kg m^{-3}
2296	2023	18,697	3680	3407	17,867	3981	3708	17,105
2334	2061	18,734	3680	3407	17,619	4105	3832	16,863
2401	2128	18,939	3681	3408	17,658	4149	3876	17,171
2414	2141	18,708	3681	3408	18,207	4191	3918	17,026
2564	2291	18,755	3684	3411	17,974	4275	4002	16,561
2605	2332	18,765	3684	3411	17,738	4352	4079	16,870
2749	2476	18,670	3685	3412	18,072	4364	4091	16,734
2772	2499	18,555	3687	3414	17,524	4420	4147	16,418
2774	2501	18,498	3687	3414	18,076	4546	4273	16,774
2918	2645	18,640	3689	3416	17,571	4642	4369	16,223
3001	2728	18,697	3690	3417	17,579	4766	4493	16,442
3121	2848	18,581	3691	3418	17,301	4862	4589	16,100
3192	2919	18,509	3693	3420	17,779	4892	4619	16,477
3302	3029	18,491	3698	3425	17,165	4926	4653	16,178
3336	3063	18,164	3701	3428	17,287	4981	4708	15,873
3351	3078	18,343	3767	3494	17,052	5192	4919	16,358
3458	3185	18,267	3828	3555	17,205	5438	5165	15,959
3556	3283	18,261	3847	3574	16,989	5631	5358	16,080
3663	3390	18,008	3904	3631	16,849			

The density values were obtained with a room-temperature density of $\rho_0 = 19256\,\mathrm{kg\,m^{-3}}$.[9]

Combined expanded temperature uncertainty for the liquid phase [$T > 3687$ K (3414 °C)]: $U_c(T)/T = 0.018$ at the beginning of the liquid phase up to $U_c(T)/T = 0.025$ at the highest temperature measured. Combined expanded density-uncertainty $U_c(\rho)/\rho = 0.013$. Uncertainties reported with a level of confidence 0.95 ($k = 2$).

B. *Critical Point Data*

The critical point of niobium and tungsten was estimated according to the publication of Schröer and Pottlacher.[4] Starting from the critical temperature T_c and critical density ρ_c, the phase diagram was estimated as described in Section II–C. Table V gives the parameters needed to plot these phase diagrams in the (ρ, T)-plane. On the way to estimate the phase diagram, a simplified Ising

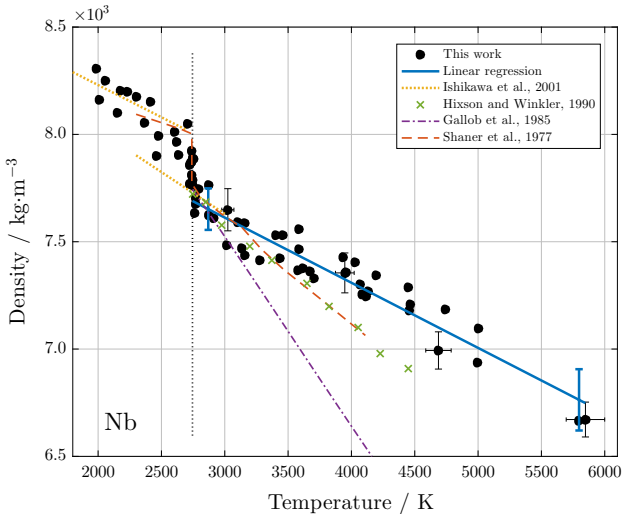

Fig. 1—Density of niobium as a function of temperature. The vertical dashed line marks the melting point. Full circles and solid line: Experimental data obtained during this work and corresponding liquid-phase linear regression. Uncertainties given at a 95 pct confidence level ($k = 2$).

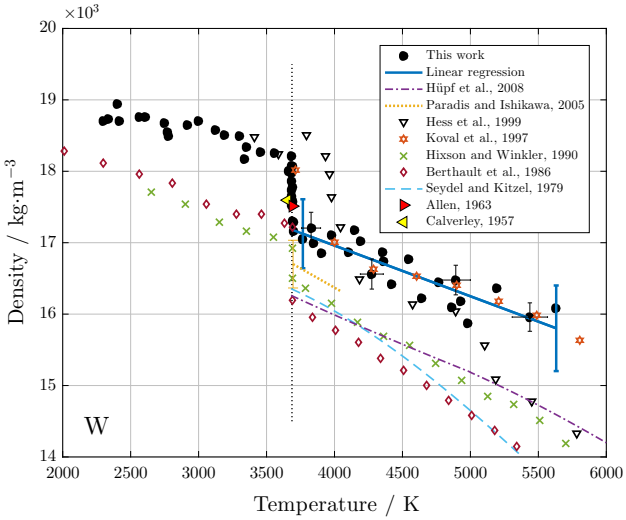

Fig. 2—Density of tungsten as a function of temperature. The vertical dotted line indicates the melting point. Full circles and solid line: This work's experimental data and corresponding liquid-phase linear regression. Uncertainties given at a 95 pct confidence level ($k = 2$). In this plot, data of Paradis *et al.*[2] were extrapolated into the liquid phase.

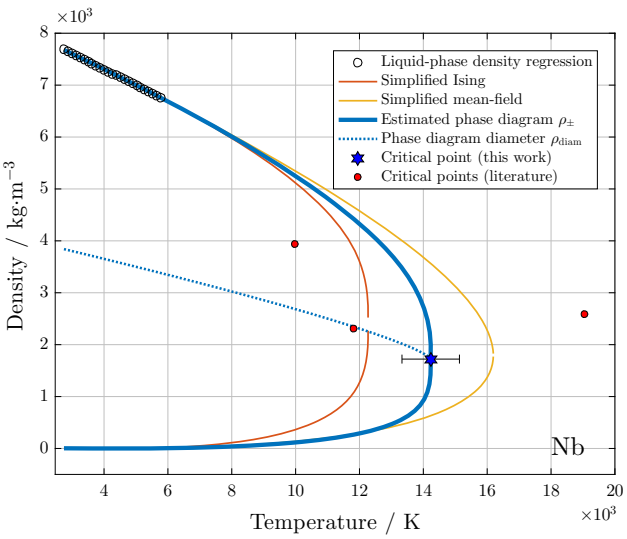

Fig. 3—Niobium: Estimated phase diagram (thick solid line) with nonlinear diameter (dotted line) and critical point (star). Open circles: Data generated by the linear regression of this work's experimental density data. Thin solid lines: Phase diagrams according to a simplified mean-field and Ising behavior. Literature values for the critical point are given (red circles) (Color figure online).

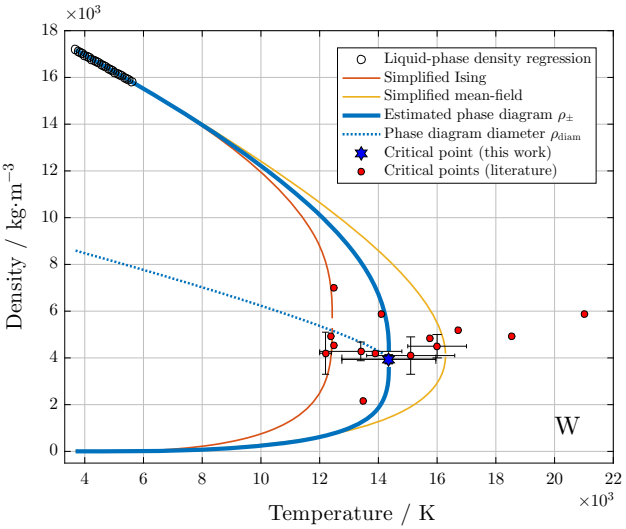

Fig. 4—Tungsten: Estimated phase diagram (thick solid line) with nonlinear diameter (dotted line) and critical point (star). Open circles: Data generated by the linear regression of this work's experimental density data. Thin solid lines: Phase diagrams according to a simplified mean-field and Ising behavior. Literature values for the critical point are given (red circles) (Color figure online).

Table V. Parameters of the Estimated Phase Diagram of Niobium and Tungsten According to Eqs. [3] and [4]

Metal	ρ_c/kg m^{-3}	T_c/K	$a/10^{-5}$K^{-1}	$c/10^{-3}$ K$^{-2/3}$	$b/10^{-1}$ K$^{-1/3}$	$b_2/10^{-4}$ K$^{-2/3}$
Niobium	1722	14,231	4.42	1.42	1.47	3.13
Tungsten	3945	14,357	4.50	1.43	3.38	3.16

Temperature range of validity from melting temperature T_m up to the critical temperature T_c of the respective metal. a, c, b and b_2 are the obtained fitting coefficients, ρ_c is the critical density.

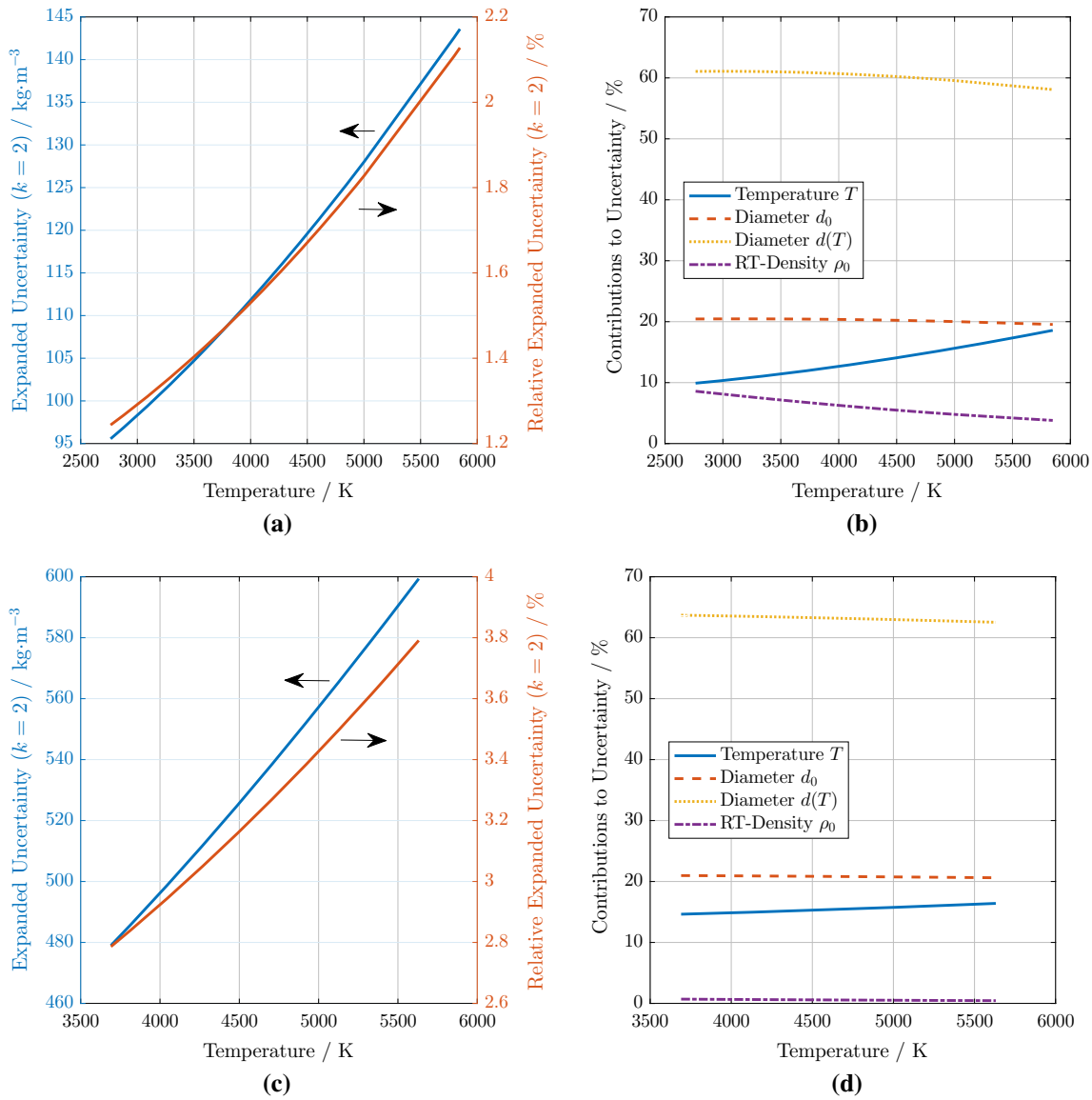

Fig. 5—Uncertainty of the liquid-phase density-regression estimated according to the GUM. Expanded uncertainty and relative expanded uncertainty ($k = 2$) as a function of temperature for niobium (*a*) and tungsten (*c*). Uncertainty budget as a function of temperature for niobium (*b*) and tungsten (*d*).

and mean-field approach is used, compare Reference 4. The resulting phase diagrams are also plotted in Figures 3 and 4. In addition, (T_c, ρ_c)-pairs were plotted when found in the literature, see Minakov *et al.*[24] as well as Hess and Schneidenbach.[25]

1. *Niobium*

For niobium, the extrapolation yields a critical point of

$$T_{c,Nb} = (14.2 \pm 0.9) \times 10^3 \text{ K}$$
$$\rho_{c,Nb} = (1.72 \pm 0.05) \times 10^3 \text{ kg m}^{-3}.$$

The estimated phase diagram is depicted in Figure 3 together with data reported in the literature. Data in the literature show a wide range from $T_c = 9989$ K reported by Young[26] to values as high as $T_c = 19{,}580$ K, published by Lang.[27] Compared to these literature values, and to the summarized values found in the comprehensive summaries on critical point data given by Blairs and Abbasi[28] and Hess and Schneidenbach,[25] our value for the critical temperature is located in the middle range.

Data for the critical density range from 2.32×10^3 kg m^{-3} as reported by Hess and Schneidenbach[25] to 3.94×10^3 kg m^{-3}, published by Young.[26] The critical density reported by us is the lowest value among those found in the literature.

2. *Tungsten*

Figure 4 shows the estimated phase diagram and critical point of tungsten. The evaluation yields a critical point of

$$T_{c,W} = (14.4 \pm 1.6) \times 10^3 \text{ K}$$
$$\rho_{c,W} = (3.95 \pm 0.19) \times 10^3 \text{ kg m}^{-3}.$$

Plenty of previous considerations on the critical point can be found in the literature. The reported values range from $T_c = 7650\,K$, published by Blairs and Abbasi[29] to values as high as $T_c = 23{,}000\,K$, reported by Grosse.[30] Comparing our value to the multitude of predictions listed by Minakov *et al.*[24] and Blairs and Abbasi[28,29] shows that our critical temperature is in the lower middle range of reported literature values. The same is true for our critical density prediction; it is also in the lower middle range compared to the literature.

IV. UNCERTAINTIES

Uncertainties for the experimental density values were calculated according to the *guide to the expression of uncertainty in measurement*, shortly referred to as GUM.[31] The uncertainty of the regression coefficients are also calculated according to GUM, by including the individual datapoint uncertainties in x- and y- directions.[32] As a result, Figures 5(a) and (c) show the expanded density uncertainty at a 95 pct confidence level at a given temperature T, *i.e.*, the temperature uncertainty is converted into a density uncertainty *via* the slope of the density regression. We discussed the approach in more detail in our previous publication on tantalum.[6] For the room-temperature density uncertainty, we adopted $u(\rho_{0,Nb}) = 14\,kg\,m^{-3}$ and $u(\rho_{0,W}) = 20\,kg\,m^{-3}$ from Reference 9. Figures 5(b) and (d) show the temperature-resolved uncertainty budget for the two investigated metals.

An uncertainty for the critical point was estimated by using the uncertainties of the density fit-coefficients listed in Table II. The extrapolation procedure was not only conducted for $\rho = a + b \cdot T$, but also for $\rho = (a + |u(a)|) + (b + |u(b)|) \cdot T$ and $\rho = (a - |u(a)|) + (b - |u(b)|) \cdot T$, where $b < 0$ and $u(x)$ denotes the standard uncertainty of x ($k = 1$). The doubled standard deviation of the mean value of these three critical point results is reported as uncertainty. Note that this uncertainty therefore only gives a rough idea of how much the critical point can vary due to the uncertainty of the density fit.

V. CONCLUSION

The temperature-dependent density of liquid niobium and liquid tungsten were determined using the ohmic pulse-heating technique. In our experiments, the obtained density gradient of liquid niobium turned out to be lower than the various different values reported in the literature, while the density at the beginning of the liquid phase is in very good agreement with the data from the literature comparison. For tungsten, the situation is different. Here, the density gradient fits in well with reported literature values, but there is a shift to lower density values of up to 5.7 pct at the beginning of the liquid phase for some authors. Others report values at melting that are up to 2.4 pct higher.

The obtained density–temperature relationship was used to estimate a phase diagram and the critical temperature in addition to the critical density of niobium and tungsten. Comparing the obtained values to the literature shows that our values for the critical temperatures of niobium and tungsten are in the (lower) middle range of the reported values. Our estimate for the critical density turned out to be at the lower end of those found in the literature.

ACKNOWLEDGMENTS

Open access funding provided by Graz University of Technology. We would like to thank Dan Alexandru Opris for the laboratory assistance during the tungsten measurements.

REFERENCES

1. T. Iida and R. Guthrie: *The Physical Properties of Liquid Metals*, Clarendon Press, Oxford, 1988, p. 47.
2. P.-F. Paradis, T. Ishikawa, R. Fujii, and S. Yoda: *Appl. Phys. Lett.*, 2005, vol. 86 (4), p. 041901.
3. P. Quested, R. Morrell, A. Dinsdale, and L. Chapman : *High Temp. - High Press.*, 2018, vol. 47, pp. 365–77.
4. W. Schröer and G. Pottlacher: *High Temp. - High Press.*, 2014, vol. 43, pp. 201–15.
5. E. Kaschnitz, G. Pottlacher, and H. Jäger: *Int. J. Thermophys.*, 1992, vol. 13 (4), pp. 699–710.
6. M. Leitner, W. Schröer, and G. Pottlacher: *Int. J. Thermophys.*, 2018, vol. 39 (11), p. 124.
7. G. Pottlacher and T. Hüpf: *Thermal Conductivity 30/Thermal Expansion 18*, DEStech Publications, Inc., 2010, pp. 192–206.
8. W.M. Haynes, ed.: *CRC Handbook of Chemistry and Physics*, 96th ed., CRC Press, 2015–2016.
9. L.C. Ming and M.H. Manghnani: *J. Appl. Phys.*, 1978, vol. 49 (1), pp. 208–12.
10. O. Database: NIST Alloy Data web application: 2018, https://trc.nist.gov/metals_data/. Accessed Oct 2018.
11. T. Ishikawa, P.-F. Paradis, and T. Itami: *Meas. Sci. Technol.*, 2005, vol. 16, pp. 443–51.
12. R. Gallob, H. Jäger, and G. Pottlacher: *High Temp. - High Press.*, 1985, vol. 17, pp. 207–13.
13. R. Hixson and M. Winkler: *High Press. Res.*, 1990, vol. 4, pp. 555–57.
14. J.W. Shaner, G.R. Gathers, and W.M. Hodgson: *Proceedings of the Seventh Symposium on Thermophysical Properties*, A. Cezailiyan, ed., American Society of Mechanical Engineers, Gaithersburg, Maryland, May 10–12, 1977, pp. 896–903.
15. G. Pottlacher, T. Neger, and H. Jäger: *Int. J. Thermophys.*, 1986, vol. 7 (1), pp. 149–59.

16. B. Allen: *Trans. AIME*, 1963, vol. 227 (239), p. 47.
17. A. Calverley: *Proc. Phys. Soc., Sect. B*, 1957, vol. 70 (11), p. 1040.
18. S.V. Koval, N.I. Kuskova, and S.I. Tkachenko: *High Temp*., 1997, vol. 35 (6), pp. 863–66.
19. H. Hess, A. Kloss, A. Rakhel, and H. Schneidenbach: *Int. J. Thermophys*., 1999, vol. 20 (4), pp. 1279–88.
20. U. Seydel and W. Kitzel: *J. Phys. F: Metal Phys*., 1979, vol. 9 (9), pp. L153–L160.
21. A. Berthault, L. Arles, and J. Matricon: *Int. J. Thermophys*., 1986, vol. 7 (1), pp. 167–79.
22. R. Hixson and M. Winkler: *Int. J. Thermophys*., 1990, vol. 11 (4), pp. 709–18.
23. T. Hüpf, C. Cagran, G. Lohöfer, and G. Pottlacher: *J. Phys.: Conf. Ser*., 2008, vol. 98 (6), p. 062002.
24. D.V. Minakov, M.A. Paramonov, and P.R. Levashov: *Phys. Rev. B*, 2018, vol. 97, p. 024205.
25. H. Hess and H. Schneidenbach: *Z. Metallkd*., 1996, vol. 87, pp. 979–84.
26. D.A. Young: *A Soft-Sphere Model For Liquid Metals*, Tech. rep., Lawrence Livermore Laboratory, Livermore, 1977.
27. G. Lang: *Z. Metallkd*., 1977, vol. 68 (3), pp. 213–18.
28. S. Blairs and M.H. Abbasi: *J. Colloid Interface Sci*., 2006, vol. 304 (2), pp. 549–53.
29. S. Blairs and M.H. Abbasi: *Acustica*, 1993, vol. 79, pp. 64–72.
30. A. Grosse: *J. Inorg. Nucl. Chem*., 1961, vol. 22 (1–2), pp. 23–31.
31. W.G. of the Joint Committee for Guides in Metrology (JCGM/WG 1): *Evaluation of measurement data—Guide to the expression of uncertainty in measurement*, JCGM—Joint Committee for Guides in Metrology, 2008.
32. M. Matus: *Tech. Mess*., 2005, vol. 72, pp. 584–91.
33. C. Cagran, C. Brunner, A. Seifter, and G. Pottlacher: *High Temp. - High Press*., 2002, vol. 34 (6), pp. 669–79.
34. R. Bedford, G. Bonnier, H. Maas, and F. Pavese: *Metrologia*, 1996, vol. 33, pp. 133–54.

Appendix

Appendix A.

Circuit diagram

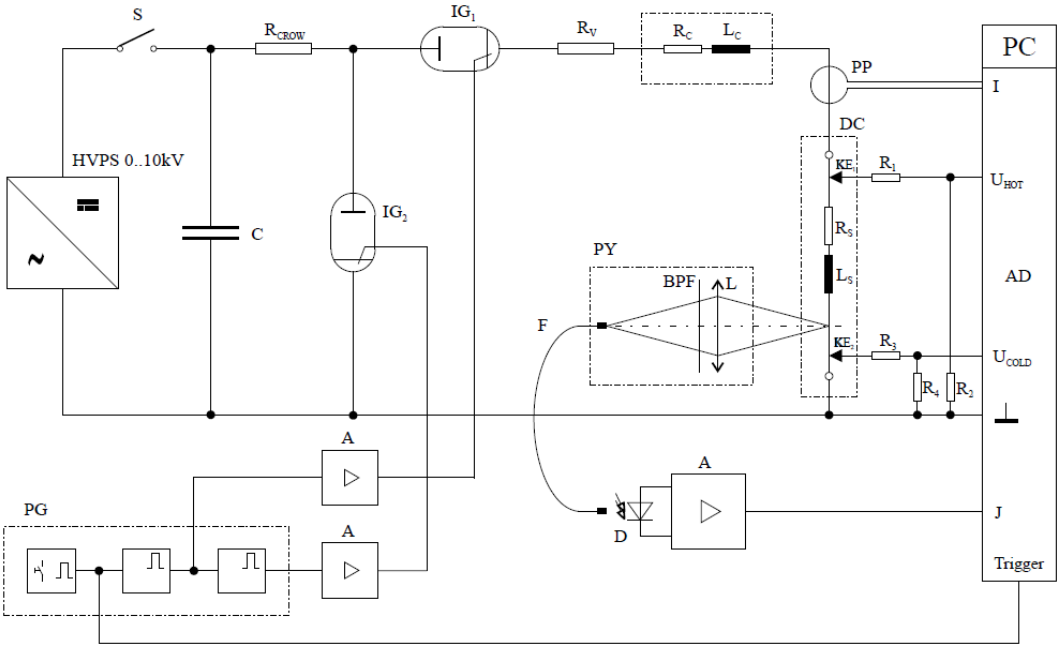

Figure A.1.: Circuit diagram of the ohmic pulse-heating setup at Graz University of Technology. Image taken from [57].
HVPS ... high voltage power supply, S ... switch, C ... capacitor bank, R_{CROW} ... crowbar resistor, IG_1 ... start Ignitron, IG_2 ... stop Ignitron, R_V ... series resistor, R_C and L_S ... resistance and inductance of the circuit, R_S and L_S ... resistance and inductance of the sample, KE_1 and KE_2 ... knife edges for voltage measurement, R_1 to R_4 ... voltage dividers, PG ... TTL pulse generator, A ... amplifier, PY ... pyrometer, BPF ... interference filter, L ... lens, F ... fiber, D ... photo diode, PP ... Pearson probe for current measurement, DC ... discharge chamber, PC ... personal computer, I ... current signal, U_{HOT} and U_{COLD} ... voltage signals, J ... pyrometer signal, AD ... transient recorder card.

Appendix B.

Experimental data

Table B.1.: **Iridium:** Experimental values of density ρ as a function of temperature T obtained in low-pressure pulse-heating experiments (atm.: N_2 at 2.3 bar). Density values were derived applying a room-temperature density of $\rho_0 = 22\,562\,\mathrm{kg \cdot m^{-3}}$. Combined expanded uncertainty between the beginning of the liquid phase ($T_\mathrm{m} = 2719\,\mathrm{K}$) up to the highest temperatures measured: $U_\mathrm{c}(T)/T = 0.016$ to 0.022, $U_\mathrm{c}(\rho)/\rho = 0.013$. Uncertainties stated at a 95 % confidence level ($k = 2$).

T / K	ρ / kg · m^{-3}	T / K	ρ / kg · m^{-3}
2173	21600	3009	19321
2237	21383	3084	19256
2412	21247	3164	19030
2462	21367	3276	19021
2514	21109	3331	19331
2534	21336	3383	18586
2613	21290	3511	19021
2708	21092	3633	18987
2715	19965	3701	18294
2716	20595	3810	18700
2718	20793	3820	18582
2718	20951	3889	18122
2720	19844	4003	18667
2723	19946	4178	18487
2724	20642	4230	17930
2726	21340	4285	18333
2729	19664	4350	18070
2731	20412	4388	17716
2735	20586	4756	17470
2768	19354	4843	17942
2844	19791	4882	17663
2884	19400		

Table B.2.: **Iridium:** Experimental values of density ρ as a function of temperature T obtained in high-pressure pulse-heating experiments (atm.: H_2O at 2 kbar to 3 kbar). Density values were derived applying a room-temperature density of $\rho_0 = 22\,562\,\mathrm{kg \cdot m^{-3}}$. Combined expanded uncertainty between the beginning of the liquid phase ($T_\mathrm{m} = 2719\,\mathrm{K}$) up to the highest temperatures measured: $U_\mathrm{c}(T)/T = 0.018$ to 0.037, $U_\mathrm{c}(\rho)/\rho =$ 0.038 to 0.034. Uncertainties stated at a 95 % confidence level ($k = 2$).

T / K	ρ / $\mathrm{kg \cdot m^{-3}}$
2695	20632
2714	20229
2836	19809
3080	19280
3409	19167
3828	18391
3993	18221
4378	17745
4775	17204
4965	16823
5355	16710
5755	15985
5972	15567
6386	15303
6756	15134
7051	14393
7521	14137
7829	13830
7997	13502
8482	13003
9163	12717

Table B.3.: **Rhenium:** Experimental values of density ρ as a function of temperature T obtained in low-pressure pulse-heating experiments (atm.: N_2 at 2.3 bar). Density values were derived applying a room-temperature density of $\rho_0 = 21\,020\,\mathrm{kg \cdot m^{-3}}$. Combined expanded uncertainty between the beginning of the liquid phase ($T_\mathrm{m} = 3458\,\mathrm{K}$) up to the highest temperatures measured: $U_\mathrm{c}(T)/T = 0.018$ to 0.021, $U_\mathrm{c}(\rho)/\rho = 0.013$. Uncertainties stated at a 95 % confidence level ($k = 2$).

T / K	ρ / $\mathrm{kg \cdot m^{-3}}$
2284	19985
2478	20176
2698	19744
3065	19432
3117	19879
3164	19274
3401	19080
3449	18916
3468	19026
3473	18748
3477	19558
3728	17931
3773	18471
4460	17748

Table B.4.: **Rhenium:** Experimental values of density ρ as a function of temperature T obtained in high-pressure pulse-heating experiments (atm.: H_2O at 1.8 kbar to 3 kbar). Density values were derived applying a room-temperature density of $\rho_0 = 21\,020\,\mathrm{kg \cdot m^{-3}}$. Combined expanded uncertainty between the beginning of the liquid phase ($T_\mathrm{m} = 3458\,\mathrm{K}$) up to the highest temperatures measured: $U_\mathrm{c}(T)/T = 0.020$ to 0.043, $U_\mathrm{c}(\rho)/\rho =$ 0.039 to 0.036. Uncertainties stated at a 95 % confidence level ($k = 2$).

T / K	ρ / $\mathrm{kg \cdot m^{-3}}$
3444	18727
3595	18354
3630	18256
3899	18104
4299	17690
4552	17379
4935	17097
4947	16803
5584	16413
5656	16710
6128	16333
6234	15957
6828	15361
6915	15251
7308	15186
7616	14822
8079	14212
8382	14252
8580	14443
9173	14031
9409	13695
9887	13405
10738	13004
11801	12265

Bibliography

[1] T. Iida and R. I. Guthrie. *The Physical Properties of Liquid Metals*. Clarendon Press Oxford, 1988. ISBN: 0-19-856331-0.

[2] P.-F. Paradis, T. Ishikawa, R. Fujii, and S. Yoda. "Physical properties of liquid and undercooled tungsten by levitation techniques." In: *Appl. Phys. Lett.* 86.4 (2005), pp. 041901–041901. DOI: 10.1063/1.1853513.

[3] D. M. Matson, X. Xiao, J. E. Rodriguez, J. Lee, R. W. Hyers, O. Shuleshova, I. Kaban, S. Schneider, C. Karrasch, S. Burggraff, R. Wunderlich, and H.-J. Fecht. "Use of Thermophysical Properties to Select and Control Convection During Rapid Solidification of Steel Alloys Using Electromagnetic Levitation on the Space Station." In: *JOM* 69.8 (2017), pp. 1311–1318. DOI: 10.1007/s11837-017-2396-5.

[4] P. Quested, R. Morrell, A. Dinsdale, and L. Chapman. "The measurement and estimation of density for selected liquid alloys." In: *High Temp. - High Pressures* 47.4 (2018), pp. 365–377. URL: https://www.oldcitypublishing.com/journals/hthp-home/hthp-issue-contents/hthp-volume-47-number-4-2018/.

[5] G. Pottlacher. *High Temperature Thermophysical Properties of 22 Pure Metals*. edition kneiper, 2010. ISBN: 978-3-9502761-6-9.

[6] P.-F. Paradis, T. Ishikawa, and S. Yoda. "Noncontact density measurements of tantalum and rhenium in the liquid and undercooled states." In: *Appl. Phys. Lett.* 83.19 (2003), pp. 4047–4049. DOI: 10.1063/1.1624475.

[7] T. Ishikawa, P.-F. Paradis, and T. Itami. "Non-contact thermophysical property measurements of refractory metals using an electrostatic levitator." In: *Meas. Sci. Technol.* 16.2 (2005), pp. 443–451. DOI: 10.1088/0957-0233/16/2/016.

[8] T. Ishikawa, P.-F. Paradis, R. Fujii, Y. Saita, and S. Yoda. "Thermophysical property measurements of liquid and supercooled iridium by containerless methods." In: *Int. J. Thermophys.* 26.3 (2005), pp. 893–904. DOI: 10.1007/s10765-005-5585-3.

[9] P.-F. Paradis, T. Ishikawa, and S. Yoda. "Non-contact measurements of thermophysical properties of niobium at high temperature." In: *J. Mater. Sci.* 36.21 (2001), pp. 5125–5130. DOI: 10.1023/A:1012477308332.

[10] P.-F. Paradis, T. Ishikawa, and S. Yoda. "Non-contact Measurements of the Thermophysical Properties of Hafnium-3 mass % Zirconium at High Temperature." In: *Int. J. Thermophys.* 24.1 (2003), pp. 239–258. DOI: 10.1023/A:1022326618592.

[11] P.-F. Paradis, T. Ishikawa, and S. Yoda. "Thermodynamic Properties Measurement of Supercooled and Liquid Rhodium." In: *Int. J. Thermophys.* 24.4 (2003), pp. 1121–1136. DOI: 10.1023/A:1025065304198.

[12] P.-F. Paradis, T. Ishikawa, and S. Yoda. "Noncontact Measurements of Thermophysical Properties of Molybdenum at High Temperatures." In: *Int. J. Thermophys.* 23.2 (2002), pp. 555–569. DOI: 10.1023/A:1015169721771.

[13] J. W. Shaner, G. R. Gathers, and W. M. Hopson. "Thermophysical Measurements on Liquid Metals above 4000 K." In: *Am. Soc. Mech. Eng.* (1977), pp. 896–903. URL: https://inis.iaea.org/search/search.aspx?orig_q=reportnumber:%22UCRL--78782%22.

[14] J. W. Shaner, G. R. Gathers, and C. Minichino. "Thermophysical properties of liquid tantalum and molybdenum." In: *High Temp. - High Pressures* 9.3 (1977), pp. 331–343. URL: https://www.oldcitypublishing.com/journals/hthp-electronic-archive-home/hthp-electronic-archive-issue-contents/hthp-volume-9-number-3-1977/.

[15] G. R. Gathers, J. W. Shaner, R. S. Hixson, and D. A. Young. "Very high temperature thermophysical properties of solid and liquid vanadium and iridium." In: *High Temp. - High Pressures* 11.6 (1979), pp. 653–668. URL: https://www.oldcitypublishing.com/journals/hthp-electronic-archive-home/hthp-electronic-archive-issue-contents/hthp-volume-11-number-6-1979/.

[16] G. R. Gathers. "Correction of Specific Heat in Isobaric Expansion Data." In: *Int. J. Thermophys.* 4.2 (1983), pp. 149–157. DOI: 10.1007/bf00500138.

[17] R. Hixson and M. Winkler. "Thermophysical Properties of Solid and Liquid Tungsten." In: *Int. J. Thermophys.* 11.4 (1990), pp. 709–718. DOI: 10.1007/bf01184339.

[18] R. Hixson and M. Winkler. "Thermophysical Properties of Liquid Niobium." In: *High Pressure Res.* 4.1-6 (1990), pp. 555–557. DOI: 10.1080/08957959008246186.

[19] R. Hixson and M. Winkler. "Thermophysical Properties of Molybdenum and Rhenium." In: *Int. J. Thermophys.* 13.3 (1992), pp. 477–487. DOI: 10.1007/bf00503884.

[20] T. Thévenin, L. Arlès, M. Boivineau, and J. Vermeulen. "Thermophysical properties of Rhenium." In: *Int. J. Thermophys.* 14.3 (1993), pp. 441–448. DOI: 10.1007/BF00566043.

[21] A. Schmon. "Density Determination of Liquid Metals by Means of Containerless Techniques." Doctoral thesis. Graz University of Technology, Institute of Experimental Physics, 2016. URL: https://diglib.tugraz.at/density-determination-of-liquid-metals-by-means-of-containerless-techniques-2016.

[22] G. Pottlacher, K. Boboridis, C. Cagran, T. Hüpf, A. Seifter, and B. Wilthan. "Normal spectral emissivity near 680 nm at melting and in the liquid phase for 18 metallic elements." In: *AIP Conference Proceedings* 1552.1 (2013), pp. 704–709. DOI: 10.1063/1.4819628.

[23] G. Pottlacher and A. Seifter. "Microsecond Laser Polarimetry for Emissivity Measurements on Liquid Metals at High Temperatures - Application to Tantalum." In: *Int. J. Thermophys.* 23.5 (2002), pp. 1267–1280. DOI: 10.1023/A:1019804623248.

[24] W. Schröer and G. Pottlacher. "Estimation of critical data and phase diagrams of pure molten metals." In: *High Temp. - High Pressures* 43.2-3 (2014), pp. 201–215. URL: https://www.oldcitypublishing.com/journals/hthp-home/hthp-issue-contents/hthp-volume-43-number-2-3-2014/.

[25] G. R. Gathers, J. W. Shaner, and W. M. Hodgson. "Thermodynamic characterization of liquid metals at high temperature by isobaric expansion measurements." In: *High Temp. - High Pressures* 11.5 (1979), pp. 529–538. URL: https://www.oldcitypublishing.com/journals/hthp-electronic-archive-home/hthp-electronic-archive-issue-contents/hthp-volume-11-number-5-1979/.

[26] S. Taioli, C. Cazorla, M. J. Gillan, and D. Alfè. "Melting curve of tantalum from first principles." In: *Phys. Rev. B* 75.21 (2007), p. 214103. DOI: 10.1103/PhysRevB.75.214103.

[27] G. Pottlacher. "Bestimmung thermophysikalische Daten von Metallen bis in den Überhitzungsbereich der flüssigen Phase." Doctoral thesis. Graz University of Technology, Institute of Experimental Physics, 1987.

[28] G. Pottlacher and H. Jäger. "A review of determinations of critical point data of metals using subsecond pulse heating techniques." In: *J. Non-Cryst. Solids* 205–207 (1996), pp. 265–269. DOI: 10.1016/S0022-3093(96)00234-7.

[29] V. E. Fortov and I. V. Lomonosov. "Shock waves and equations of state of matter." In: *Shock Waves* 20.1 (2010), pp. 53–71. DOI: 10.1007/s00193-009-0224-8.

[30] R. W. Ohse and H. von Tippelskirch. "The critical constants of the elements and of some refractory materials with high critical temperatures (a review)." In: *High Temp. - High Pressures* 9.4 (1977), pp. 367–385. URL: https://www.oldcitypublishing.com/journals/hthp-electronic-archive-home/hthp-electronic-archive-issue-contents/hthp-volume-9-number-4-1977/.

[31] G. Lang. "Kritische Temperaturen und Temperaturkoeffizienten der Oberflächenspannung flüssiger Metalle." In: *Z. Metallkde.* 68.3 (1977), pp. 213–218.

[32] H. Hess. "Critical Data of Metals-Estimations for Tungsten." In: *Phys. Chem. Liq.* 30.4 (1995), pp. 251–256. DOI: 10.1080/00319109508030672.

[33] D. Gates and G. Thodos. "The Critical Constants of the Elements." In: *A.I.Ch.E Journal* 6.1 (1960), pp. 50–54. DOI: 10.1002/aic.690060110.

[34] S. Blairs and M. H. Abbasi. "Correlation between surface tension and critical temperatures of liquid metals." In: *J. Colloid Interface Sci.* 304.2 (2006), pp. 549–553. DOI: 10.1016/j.jcis.2006.07.072.

[35] A. Grosse. "The Temperature Range of Liquid Metals and an Estimate of their Critical Constants." In: *J. Inorg. Nucl. Chem.* 22.1-2 (1961), pp. 23–31. DOI: 10.1016/0022-1902(61)80225-x.

[36] A. Grosse. "The Realtionship between the Surface Tensions and Energies of Liquid Metals and Their Critical Temperatures." In: *J. Inorg. Nucl. Chem.* 24.2 (1962), pp. 147–156. DOI: 10.1016/s0022-1902(62)90147-1.

[37] J. Bohdansky. "Temperature Dependence of Surface Tension for Liquid Metals." In: *J. Chem. Phys.* 49.7 (1968), pp. 2982–2986. DOI: 10.1063/1.1670540.

[38] R. E. Goldstein, A. Parola, and A. P. Smith. "Fluctuating pseudoatoms in metallic fluids." In: *J. Chem. Phys.* 91.3 (1989), pp. 1843–1854. DOI: 10.1063/1.457089.

[39] H. Hess and H. Schneidenbach. "On the Estimation of Critical Point Data of Transition Metals." In: *Z. Metallkde.* 87.12 (1996), pp. 979–984.

[40] S. Blairs and M. H. Abbasi. "Internal Pressure Approach for the Estimation of Critical Temperatures of Liquid Metals." In: *Acustica* 79.1 (1993), pp. 64–72. URL: https://www.ingentaconnect.com/content/dav/aaua/1993/00000079/00000001/art00010.

[41] L. Cailletet and E. Mathias. In: *Compt. Rend.* 104 (1887), pp. 1563–1571.

[42] H. Hess, E. Kaschnitz, and G. Pottlacher. "Thermophysical Properties of Liquid Cobalt." In: *High Pressure Res.* 12.1 (1994), pp. 29–42. DOI: 10.1080/08957959408201653.

[43] A. Likalter. "On Critical Parameters of Metals." In: *Teplofiz. Vys. Temp.* 23.3 (1985), pp. 465–472.

[44] D. A. Young and B. J. Alder. "Critical Point of Metals from the van der Waals Model." In: *Phys. Rev. A* 3.1 (1971), pp. 364–371. DOI: 10.1103/physreva.3.364.

[45] D. A. Young. *A Soft-Sphere Model For Liquid Metals*. Tech. rep. UCRL-52352. Lawrence Livermore Laboratory, 1977. DOI: 10.2172/5154392.

[46] G. R. Gathers. "Dynamic Methods for Investigating thermophysical Properties of Matter at very high Temperatures and Pressures." In: *Rep. Prog. Phys.* 49.4 (1986), pp. 341–396. DOI: 10.1088/0034-4885/49/4/001.

[47] V. E. Fortov, K. V. Khishchenko, P. R. Levashov, and I. V. Lomonosov. "Wide-range multi-phase equations of state for metals." In: *Nucl. Instrum. Methods Phys. Res., Sect. A* 415.3 (1998), pp. 604–608. DOI: 10.1016/s0168-9002(98)00405-7.

[48] L. Miljacic, S. Demers, Q.-J. Hong, and A. van de Walle. "Equation of state of solid, liquid and gaseous tantalum from first principles." In: *Calphad* 51 (2015), pp. 133–143. DOI: 10.1016/j.calphad.2015.08.005.

[49] D. V. Minakov, M. A. Paramonov, and P. R. Levashov. "Consistent interpretation of experimental data for expanded liquid tungsten near the liquid-gas coexistence curve." In: *Phys. Rev. B* 97.2 (2018), p. 024205. DOI: 10.1103/PhysRevB.97.024205.

[50] A. L. Khomkin and A. S. Shumikhin. "Critical points of metal vapors." In: *J. Exp. Theor. Phys.* 121.3 (2015), pp. 521–528. DOI: 10.1134/S1063776115090162.

[51] G. Pottlacher and T. Hüpf. "A Review of Expansion Measurements for Subsecond Ohmic Pulse-Heating Experiments." In: *Thermal Conductivity 30: Thermal Expansion 18: Joint Conferences: August 29-September 2, 2009, Pittsburgh, Pennsylvania, USA*. Vol. 30. DEStech Publications, Inc. 2010, p. 192. ISBN: 978-1-60595-015-0.

[52] T. Hüpf. "Density Determination of Liquid Metals." Doctoral thesis. Graz University of Technology, Institute of Experimental Physics, 2010. URL: https://diglib.tugraz.at/density-determination-of-liquid-metals-2010.

[53] B. Wilthan, W. Schützenhöfer, and G. Pottlacher. "Thermophysical Properties of Five Industrial Steels in the Solid and Liquid Phase." In: *Int. J. Thermophys.* 38.6 (2017), p. 83. DOI: 10.1007/s10765-017-2220-z.

[54] T. Macher. "Modernisierung einer ohmschen Pulsheizapparatur zur Bestimmung thermophysikalischer Daten von Metallen in der flüssigen Phase - Datenerfassung, Datenauswertung und Unsicherheitsanalyse." Diploma thesis. Graz University of Technology, Institute of Experimental Physics, 2014. URL: https://diglib.tugraz.at/modernisierung-einer-ohmschen-pulsheizapparatur-zur-bestimmung-thermophysikalischer-daten-von-metallen-in-der-fluessigen-phase-2014.

[55] A. Seifter. "Bestimmung des normalen spektralen Emissionskoeffizienten von flüssigen pulsgeheizten Metallen mittels eines schnellen Photopolarimeters." Doctoral thesis. Graz University of Technology, Institute of Experimental Physics, 2001. URL: https://www.tugraz.at/fileadmin/user_upload/Institute/IEP/Thermophysics_Group/Files/Diss-SeifterAchim.pdf.

[56] J. Kestin, J. V. Sengers, B. Kamgar-Parsi, and J. M. H. L. Sengers. "Thermophysical Properties of Fluid H2O." In: *J. Phys. Chem. Ref. Data* 13.1 (1984), pp. 175–183. DOI: 10.1063/1.555707.

[57] F. Sachsenhofer. "Data evaluation for pulse heating experiments combined with emissivity measurements using a division-of-amplitude photopolarimeter." MA thesis. Graz University of Technology, Institute of Experimental Physics, 2000. URL: https://www.tugraz.at/fileadmin/user_upload/Institute/IEP/Thermophysics_Group/Files/DA-SachsenhoferFranz.pdf.

[58] A. Seifter. "Bestimmung thermophysikalischer Daten von Eisen - Nickel - Legierungen im flüssigen Zustand mittels ohmscher Pulsaufheizung." MA thesis. Graz University of Technology, Institute of Experimental Physics, 1996. URL: https://www.tugraz.at/fileadmin/user_upload/Institute/IEP/Thermophysics_Group/Files/DA-SeifterAchim.pdf.

[59] M. Leitner, W. Schröer, and G. Pottlacher. "Density of Liquid Tantalum and Estimation of Critical Point Data." In: *Int. J. Thermophys.* 39.11 (2018), p. 124. DOI: 10.1007/s10765-018-2439-3.

[60] T. Ishikawa, J. T. Okada, Y. Watanabe, et al. "Thermophysical Property Measurements of High Temperature Melts Using an Electrostatic

Levitation Method." In: *Jpn. J. Appl. Phys.* 50.11S (2011), 11RD03. DOI: 10.7567/jjap.50.11rd03.

[61] P. Klemens. "Theory of thermal conductivity of solids at high temperatures." In: *High Temp. - High Pressures* 15.3 (1983), pp. 249–254. URL: https://www.oldcitypublishing.com/journals/hthp-electronic-archive-home/hthp-electronic-archive-issue-contents/hthp-volume-15-number-3-1983/.

[62] P. Pichler and G. Pottlacher. "Thermal Conductivity of Liquid Metals." In: *Impact of Thermal Conductivity on Energy Technologies*. 2018. DOI: 10.5772/intechopen.75431.

[63] *The new International System of Units (SI)*. PTB. 11/2017. URL: https://www.ptb.de/cms/fileadmin/internet/presse_aktuelles/broschueren/intern_einheitensystem/Info_Sheet_The_New_SI_V2.pdf.

[64] D. Errandonea, M. Somayazulu, D. Häusermann, and H. K. Mao. "Melting of tantalum at high pressure determined by angle dispersive x-ray diffraction in a double-sided laser-heated diamond-anvil cell." In: *J. Phys.: Condens. Matter* 15.45 (2003), pp. 7635–7649. DOI: 10.1088/0953-8984/15/45/003.

[65] J. W. Shaner, G. R. Gathers, and C. Minichino. "A New Apparatus for Thermophysical Measurements Above 2500 K." In: *High Temp. - High Pressures* 8.4 (1976), pp. 425–429. URL: https://www.oldcitypublishing.com/journals/hthp-electronic-archive-home/hthp-electronic-archive-issue-contents/hthp-volume-8-number-4-1976/.

[66] Y. Marcus. "On the compressibility of liquid metals." In: *J. Chem. Thermodyn.* 109 (2017). Special Issue on Volume Properties, pp. 11–15. DOI: 10.1016/j.jct.2016.07.027.

[67] R. M. Pope and E. S. Fry. "Absorption spectrum (380–700 nm) of pure water. II. Integrating cavity measurements." In: *Appl. Opt.* 36.33 (1997), pp. 8710–8723. DOI: 10.1364/AO.36.008710.

[68] V. S. Langford, A. J. McKinley, and T. I. Quickenden. "Temperature Dependence of the Visible-Near-Infrared Absorption Spectrum of Liquid Water." In: *J. Phys. Chem. A* 105.39 (2001), pp. 8916–8921. DOI: 10.1021/jp010093m.

[69] B. Wilthan, C. Cagran, and G. Pottlacher. "Combined DSC and Pulse-Heating Measurements of Electrical Resistivity and Enthalpy of Tungsten, Niobium, and Titanium." In: *Int. J. Thermophys.* 26.4 (2005), pp. 1017–1029. DOI: 10.1007/s10765-005-6682-z.

[70] R. Gallob, H. Jäger, and G. Pottlacher. "Recent results on thermophysical data of liquid niobium and tantalum." In: *High Temp. - High Pressures* 17.2 (1985), pp. 207–213. URL: https://www.oldcitypublishing.com/journals/hthp-electronic-archive-home/hthp-electronic-archive-issue-contents/hthp-volume-17-number-2-1985/.

[71] C. Cagran and G. Pottlacher. "Thermophysical Properties and Normal Spectral Emittance of Iridium up to 3500 K." In: *Int. J. Thermophys.* 28.7 (2007), pp. 697–710. DOI: 10.1007/s10765-007-0188-9.

[72] T. Hüpf, C. Cagran, G. Lohöfer, and G. Pottlacher. "Electrical resistivity of high temperature metallic melts–Hf-3% Zr, Re, Fe, Co, and Ni." In: *High Temp. - High Pressures* 37.3 (2008), pp. 239–246. URL: https://www.oldcitypublishing.com/journals/hthp-home/hthp-issue-contents/hthp-volume-37-number-3-2008/.

[73] H. Jäger, W. Neff, and G. Pottlacher. "Improved Thermophysical Measurements on Solid and Liquid Tantalum." In: *Int. J. Thermophys.* 13.1 (1992), pp. 83–93. DOI: 10.1007/BF00503358.

[74] K. Mills, B. Monaghan, and B. Keene. "Thermal conductivities of molten metals: Part 1 Pure Metals." In: *Int. Mater. Rev.* 41.6 (1996), pp. 209–242. DOI: 10.1179/imr.1996.41.6.209.

[75] W. M. Haynes, ed. *CRC Handbook of Chemistry and Physics*. 96th ed. CRC Press, 2015 - 2016. ISBN: 978-1-4822-6096-0.

[76] D. R. Lide, ed. *CRC Handbook of Chemistry and Physics*. 85th ed. CRC Press, 2004. ISBN: 0-8493-0485-7.

[77] J. W. Arblaster. "Densities of Osmium and Iridium." In: *Platinum Met. Rev.* 33.1 (1989), pp. 14–16. URL: https://www.technology.matthey.com/article/33/1/14-16/.

[78] A. H. Harvey, J. S. Gallagher, and J. M. H. L. Sengers. "Revised Formulation for the Refractive Index of Water and Steam as a Function of Wavelength, Temperature and Density." In: *J. Phys. Chem. Ref. Data* 27.4 (1998), pp. 761–774. DOI: 10.1063/1.556029.

[79] G. S. K. Wong and S.-m. Zhu. "Speed of sound in seawater as a function of salinity, temperature, and pressure." In: *J. Acoust. Soc. Am.* 97.3 (1995), pp. 1732–1736. DOI: 10.1121/1.413048.

[80] M. Leitner and G. Pottlacher. "Density of Liquid Niobium and Tungsten and the Estimation of Critical Point Data." In: *Metall. Mater. Trans. A* 50.8 (2019), pp. 3646–3653. DOI: 10.1007/s11661-019-05262-5.

[81] R. Bedford, G. Bonnier, H. Maas, and F. Pavese. "Recommended values of temperature on the International Temperature Scale of 1990 for a selected set of secondary reference points." In: *Metrologia* 33.2 (1996), pp. 133–154. DOI: 10.1088/0026-1394/33/2/3.

[82] T. Hüpf and G. Pottlacher. "Thermal expansion of Ir, Pd, Pt, and V obtained in fast pulse-heating experiments." In: *High Temp. - High Pressures* 40.3-4 (2011), pp. 271–279. URL: https://www.oldcitypublishing.com/journals/hthp-home/hthp-issue-contents/hthp-volume-40-number-3-4-2011/.

[83] C. Cagran, B. Wilthan, and G. Pottlacher. "Normal Spectral Emissivities (at 684.5 nm) of Liquid Gold, Rhenium, Titanium and Vanadium." In: *Conference Proceedings Tempmeko* (2004), pp. 1313–1318.

[84] V. E. Fortov, A. N. Dremin, and A. A. Leont'ev. "Evaluation of the Parameters of the Critical Point." In: *Teplofiz. Vys. Temp.* 13.5 (1974), pp. 1072–1080.

[85] B. Wilthan. "Verhalten des Emissionsgrades und thermophysikalische Daten von Legierungen bis in die flüssige Phase mit einer Unsicherheitsanalyse aller Messgrößen." Doctoral Thesis. Graz University of Technology, Institute of Experimental Physics, 2005. URL: https://www.tugraz.at/fileadmin/user_upload/Institute/IEP/Thermophysics_Group/Files/Diss-WilthanBoris.pdf.

[86] W. G. 1. of the Joint Committee for Guides in Metrology (JCGM/WG 1). *Evaluation of measurement data - Guide to the expression of uncertainty in measurement*. JCGM, 2008. URL: https://www.bipm.org/en/publications/guides/gum.html.

[87] M. Matus. "Koeffizienten und Ausgleichsrechnung: Die Messunsicherheit nach GUM, Teil 1: Ausgleichsgeraden." In: *Tech. Mess.* 72.10 (2005), pp. 584–591. DOI: 10.1524/teme.2005.72.10_2005.584.